CHARACTERIZATION & ANALYSIS ON ELECTROLYTIC DECOMPOSITION OF HYDROXYLAMMONIUM NITRATE (HAN) TERNARY MIXTURES IN MICROREACTORS

CHAI WAI SIONG, BEng.

Thesis submitted to the University of Nottingham

For the degree of Doctor of Philosophy

2017

Abstract

Rapid development of micropropulsion systems arose from growing interest on micro- and nanosatellites. Utilization of liquid energetic materials such as hydrazine and hydrogen peroxide as propellant in propulsion yielded promising results. However, safety issue remains a great concern as hydrazine is highly toxic. This drives the development of propellants towards lower toxicity and more environmental friendly, namely green propellants.

Hydroxylammonium nitrate (HAN) was selected among three green propellants due to its high energy density in addition to ease in storage and handling properties. In order to understand the effect of addition of fuel into HAN binary solution, electrolytic decomposition of zero oxygen balance HAN ternary mixture in thermal isolated beaker was performed at macroscale. Addition of a fuel to binary HAN solution generally has more stages of decomposition, as opposed to single stage in binary HAN solution. Rate of temperature increase in the first stage of decomposition ($\dot{T}_1$) was found to be directly proportional to electrical resistivity of the HAN ternary mixture, while maximum electrolytic decomposition temperature (T_{max}) of HAN ternary mixture obtained was dependent on fuel added.

Visualization of HAN decomposition was demonstrated using transparent PDMS microreactors. A novel DPST integration in triggering the power supply and high speed camera was proposed. Such

integration greatly reduced the cost of using a DAQ system, and was shown to capture the decomposition successfully at 5000 *fps*.

Parametric optimization was also carried out in PDMS microreactors. Usage of 3 pairs of electrodes has increased overall reaction rate as high as 225 %, as compared to 1 pair counterpart. The overall reaction rate is proportional to flowrate and applied voltage. 3 pairs of electrodes can initiate decomposition in low voltage region. Applied voltage is the most significant parameter affecting the overall reaction rate. HAN-dextrose has lower decomposition performance compared to binary HAN solution in PDMS microreactor, using the optimized parameters carried out on binary HAN solution.

This work has demonstrated both effect of fuel addition in binary HAN solution and parametric optimization in binary HAN solution towards their decomposition phenomena at macroscale and microscale, respectively. Several recommendations were made in future work section, including using screen-printing technology on the microreactor and adding a catalytic reactor after HAN was electrolyzed, to further improve decomposition efficiency.

Publication – Conference

1. **Wai Siong Chai**, JitKai Chin, Tengku Farah Wahida, '*Parameters Affecting Electrolytic Decomposition Perofrmance of Concentrated Hydroxylammonium Nitrate (HAN) Ternary Mixtures*', SmallSAT Colloquium 2013, Kuala Lumpur, September 2013.
2. **Wai Siong Chai**, K. S. Koh, Kean How Cheah, Jit-Kai Chin, Tengku Farah Wahida, '*Performance Comparison between Single and Multi-electrode System for Electrolytic Decomposition of HAN*', International Symposium on Space Technology and Science 2015, Kobe, Japan, July 2015.

Publication – Journal

1. **Wai Siong Chai**, Kean How Cheah, K. S. Koh, Jitkai Chin, T. F. W. K. Chik, '*Parametric Studies of Electrolytic Decomposition of Hydroxylammonium Nitrate (HAN) Energetic Ionic Liquid in Microreactor using Image Processing Technique*', Chemical Engineering Journal, Vol. 296, pg. 19 – 27, 2016
2. **Wai Siong Chai**, Kean How Cheah, K. S. Koh, Jitkai Chin, T. F. W. K. Chik, '*Calorimetric Study on Electrolytic Decomposition of Hydroxylammonium Nitrate (HAN) Ternary Mixtures*' (Submitted to Propellants, Explosives, Pyrotechnics)

Acknowledgements

It has been almost four years since I started this work.

I would like to express my gratitude towards many individuals. Without their help, advice and support, this thesis would not be completed successfully.

Firstly, I would like to thank my supervisor, Dr. Chin Jit Kai, for his full support throughout these years. The freedom given to explore beyond our initial goals is much appreciated. I am very thankful for his willingness to share his knowledge and other information with me.

Secondly, I would like to thank my girlfriend, Sze Shin, and also my family, for their continuous support and patience during my postgraduate education. Thanks to my brother who took good care of my parents, which allows me to concentrate better in my studies. It means a lot to me for them to be able to understand my situation.

Special thanks to technical staffs, Andrew, Faizal, Filzah, Kumar, in helping to setting up or assisting various laboratory works. It has been a pleasure to work with my seniors, as well as my collaborators, Kean How and Kai Seng. How can I miss out my fellow office mates – Adam, Milor, Yoong Kit and Soon Yee. Our badminton game has certainly cheered up our research life even more. It has also been a pleasure to work with my fellow group members - Asad, Kalai, Chang Nong, Keat Liong, June, Nabeel and Voon Loong. Our summer intern, Hui Mien, whom I had been glad to work with, assisted in our work a lot too.

I would like to express my gratitude to the International Symposium on Space Technology and Science 2015 (ISTS 2015) committee for awarding me the scholarship. With the sponsorship, I had the opportunity to participate in ISTS 2015 conference in Japan. It was a great experience to be able to gather with people from niche field like mine. And I even had the opportunity to talk to people from European Space Agency (ESA).

To all the other individuals whom I forgot to mention, thanks a lot.

List of Figures

List of Tables

Nomenclature

Acronyms

ADN	Ammonium dinitramide
AN	Ammonium nitrate
ANOVA	Analysis of variance
AP	Ammonium perchlorate
BNC	Bayonet Neill-Concelman
CAD	Computer-aided design
CINE	Vision Research Phantom CINE vamera video file
DAQ	Digital acquisition
DC	Direct current
DPST	Double pole single throw
DRIE	Deep reactive ion-etching
DSC	Differential scanning calorimetry
DTA	Differential thermal analysis
EDX	Energy-dispersive X-ray spectroscopy
EIL	Energetic ionic liquid
f-value	Factor value
fps	Frames per second
FTIR	Fourier transform infrared spectroscopy
HAN	Hydroxylammonium nitrate
HNF	Hydrazinium nitroformate
HTCC	High-temperature co-fired ceramic
IBAT	Image-based auto trigger

LGP	Liquid gun propellant
LTCC	Low-temperature co-fired ceramic
LED	Light-emitting diode
MEMS	Microelectromechanical systems
NOx	Nitrogen oxides
OB	Oxygen balance
p-value	Probability value
PDMS	Polydimethylsiloxane
R^2	Coefficient of determination
ROI	Region of interest
SEM	Scanning electron microscope
TEAN	Triethylammonium nitrate
TGA	Thermogravimetric analysis
TIFF	Tagged Image File Format
TMD	Transmembrane domain
TQ-MS	Triple quadrupole mass spectrometer
TTL	Transistor-transistor logic

Symbols

A	Number of electrode pairs	
B	HAN flowrate	µl/min
C	Applied voltage	V
ΔH	Total heat	kJ
ΔH_{rxn}	Heat of reaction	kJ/mol
ΔP	Pressure increment	mbar/s

Δt_n	Time required for the electrolytic decomposition to complete n^{th} stage	s
Δt_2	duration of second stage	s
ΔT_3	Temperature difference between T_2 and T_{max} in 3^{rd} stage	°C
E_a	Activation energy	kJ/mol
h	Height	µm
H	Joule heat	J
H/t	Joule heating rate	W
I	Current	A
l	Length	µm
L1	First half of microreactor length	
L2	Second half of microreactor length	
LD_{50}	Lethal dose	mg/kg
m	Mass	kg
M	Molarity	M
MW	Molecular weight of compound	g/mol
OB%	Oxygen balance	%
ρ	Density	g/cm^3
ρ_M	Mixture resistivity	µΩ.m
$\dot{Q}$	Flowrate	µl/min
$\dot{Q}_{gen}$	Rate of heat generation	W
$\dot{Q}_{loss}$	Rate of heat loss	W
r	Radius	µm
R	Resistance	Ω
S.A.	Surface area	m^2/g
SD	Standard deviation	

t	Time	s
t_1	Time taken for decomposition to reach 100 °C	s
t_f	Time taken for decomposition to reach T_{max}	s
t_i	Initial time of decomposition	s
t_{total}	Time taken for the electrolytic decomposition to complete	s
T	Temperature	°C
T_0	Mixture initial temperature before the decomposition began	°C
T_2	Temperature before the mixture has a second rise in temperature	°C
$T_{aveHANfuel}$	Average temperature of interaction between HAN and fuel	°C
T_{max}	Maximum attainable temperature for the electrolytic decomposition of HAN ternary mixture	°C
$\dot{T}$	Rate of temperature elevation	°C/s
$\dot{T}_1$	Rate of temperature elevation during first stage of electrolytic decomposition	°C/s
$\dot{T}_2$	Rate of temperature elevation during second stage of electrolytic decomposition	°C/s
V	Applied voltage	V
w(HAN)	Weight percentage of HAN	wt%
X	Number of atoms of carbon	
Y	Number of atoms of hydrogen	
Z	Number of atoms of oxygen	

Chapter 1 Introduction

1.1 The emerging of nanosatellites

Micro (10 – 100 *kg*) and nanosatellite (1 - 10 *kg*) were classified according to the masses, respectively. As forecast by *Depasquale* and *Bradford*, more than 100 nano/microsatellites will be launched annually by 2020 and beyond [1]. It was reported that 158 nanosatellites and microsatellites were launched in 2014 in the latest report from SpaceWorks, showing an increase of 72 % compared to 2013 [2]. A continuous incline trend in the launch of nano/microsatellite grown by 8.6% per annum since 2000 and is expected to grow at 23.8 % per year over next 6 years (2014-2020) [1, 2].

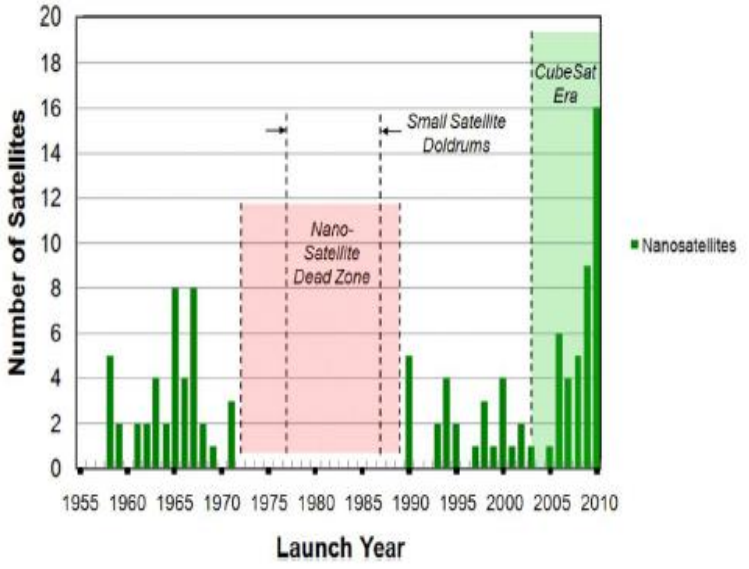

Figure 1.1 Successful global nanosatellite (1 – 10 *kg*) launch history [3].

As shown in Figure 1.1, the first nanosatellite, Explorer 1 (14 *kg*), was launched by the United States (US) in the late 1950s [4, 5].

Launching of nanosatellites was active for more than a decade but later fell into dead zone till the 1990s. During this period, larger, heavier and more complex satellites were being focused extensively, culminating in the decrease in flight opportunities and increase in cost per mission. For such missions, research and development on large satellite could take more than 10 years before it is ready for launching. Integration of various functions into large satellites compromised launch opportunity or launch window. As a result of poor and inefficient design, system failure could easily lead to failure of the whole mission. Realizing the severity of the problem, attention on micro- and nanosatellites was regained from the space community as their functions were simplified. The latest development and operation concept of functions in large satellite are distributed to several smaller satellites, which are simpler and more cost-effective to develop.

The philosophy of micro- and nanosatellites is especially useful for developing countries, as the approach is more cost effective. As the mission complexity and cost were reduced, space program can be developed independently without relying on developed countries. Direct control and access to their satellites are the advantages, without relying on major satellite service providers. These satellites are also attractive to established space agencies with more mission opportunities granted, they could be used as a platform to verify novel technological ideas. Cost-effectiveness of such philosophy granted all parties opportunities to initiate more research to space.

1.2 Green chemical propellants

Power needed for satellites operation generally can be split into two parts, i.e. electronics usage and thrust. Power requirement for electronics usage in satellites is normally supplied by solar panels onboard. An independent thruster is needed for attitude control and orbital station-keeping. Generally, solid, liquid or ion thrusters were used in large satellites or rocket. Meanwhile, for micro- or nanosatellites, liquid chemicals thrusters are preferred than ion thruster as they require lesser electrical energy. Limited supply of electrical energy also inhibits the usage of ion thruster. Hydrazine is commonly used in the liquid chemical thrusters [6]. With storage being an issue, a denser liquid chemical thrusters is preferred, as higher density impulse can be achieved.

In order to provide attitude control systems in these micro- or nanosatellites, there is a growing interest in microcombustion-based devices, as combustion is the core process of micropropulsion system. Microcombustion connecting to a nozzle provides thrust which will benefit the propulsion purpose. Developments in such microcombustion devices could be integrated in microthrusters and further developed into an efficient micropropulsion system. Advancement in microelectromechanical system (MEMS) field enables fast-growing microsatellites technology to be constantly improved, thus reducing the cost [7]. For example, higher image quality on camera is achieved although cheaper material is used. As a result of “crossover” between MEMS technology and high temperature materials, microscale

combustion was attempted using conventional hydrocarbon fuel in diverse applications including microreactor, microheater and micropropulsion [8-10]. Microcombustor was proven to reduce the inlet temperature by 370 °*C*, as compared to 600 °*C* in conventional combustor, thus reducing the power consumption for total system, yet achieving efficiency of higher than 90 % and delivering higher power density [8].

Lately, attention from the microscale aerospace scientific communities was focused on energetic materials including hydroxylammonium nitrate (HAN), ammonium dinitramide (ADN), hydrogen peroxide (H_2O_2) and hydrazinium nitroformate (HNF) due to their lower toxicity level, as compared to hydrazine [11]. HAN-based propellants receive most attention among these energetic material candidates, because of its easy-handling properties and high energy density [12]. The safety of HAN-based AF-M315E has recently been verified and considered as a potential candidate to be used in microthrusters and micro-spacecrafts for orbital station-keeping [13]. However, much lacking in technicality such as insufficient understanding of combustion chemistry during combustion of HAN-based propellant is the main factor hindering microcombustor development. The other significant challenges including:

1. Highly reliable combustion technique
2. Combustion stability
3. Heat flow management

4. Microscale fabrication technique and material

Inspired by this, an attempt of HAN-based mixtures, were investigated at both macro- and microscale, respectively. Electrolytic decomposition was adapted as the primary decomposition method due to ionic properties of HAN solution. Theoretically, electrical energy could be deposited directly into HAN solution and the combustion found to be more efficient as it was targeted to specific species in the system. The project will first attempt of a macroscale decomposition of HAN ternary mixtures, serving as an initial screening of potential fuel candidate of the mixtures.

Through macroscale decomposition, the overall decomposition phenomenon can be clearly observed aiming to provide a description of the process, which was not being extensively studied so far. Next, microscale decomposition of HAN binary solution was carried out to verify the determining factor affecting the overall reaction rate. Lastly, optimization of parametric study was also performed, aiming to provide best setup for the optimized decomposition process.

On the other hand, decomposition of HAN binary system has been previously attempted [14]. Current work uses that as a benchmark, aiming to further extend the study in depth, by comparing the decomposition performance of ternary system in current work and binary system in previous work.

1.3 Motivations

Owing to the project scope, much limitations were identified and presented in Chapter 2. The limitations are the motivation of current study and detail as below. A number of research objectives are then outlined in the next sub-chapter.

1.3.1 Low efficiency of conventional HAN decomposition techniques

Combustion of HAN solution is commonly carried out through thermal heating or catalytic decomposition. However, requirement of pre-heating in both techniques limit their applications in microthruster due to low energy supply available in microsatellites. The rate of heat generation and heat loss are expressed as $\dot{Q}_{gen} \propto l^3$ and $\dot{Q}_{loss} \propto l^2$, respectively, where l represents characteristic length [15]. This yields a ratio of $\dot{Q}_{loss}/\dot{Q}_{gen} \propto 1/l$, suggesting that the heat loss is enhanced as the system is downsized. Significant heat loss and limited heat supply are the technical difficulties in microscale operation, leading to low combustion efficiency and insufficient heat for propellant heating.

In conventional thermal heating, HAN is heated by a heating element to reach its ignition temperature. Wastage of heat energy usually occurs at microscale as heat transfer to the surrounding is enhanced due to higher surface area to volume ratio compared to macroscale, leading to an inefficient overall decomposition system. In catalytic decomposition, energy is either provided to pre-heat the propellant before it reaches the

catalyst to achieve higher conversion rate or to pre-heat the catalyst to attain reaction temperature for higher yield. Apart from the conventional decomposition techniques aforementioned, electrolytic decomposition refers to deposit of electrical energy directly to the propellant to decompose it.

These combustion techniques adapted from hydrazine studies were employed in HAN applications. Both conventional decomposition methods still face great challenges as complete decomposition is yet to be achieved. Being an ionic liquid, HAN had that advantage over hydrazine, enables it to be electrolyzed. Electrolytic decomposition technique was chosen as energy deposition to HAN solution is more direct as compared to aforementioned decomposition techniques, thus increase the overall decomposition. Furthermore, decomposition mechanisms involved were studied, aiming to understand in-depth on the overall decomposition process.

1.3.2 Potentiality of HAN ternary propellants

Combustion study on HAN was commonly conducted in ternary form, which consists of HAN, water and fuel. Common HAN ternary propellants are LP 1846 (60.8 % HAN, 19.2 % triethyammonium nitrate (TEAN), 20 % water (H_2O)) and SHP 163 (74 % HAN, 4 % ammonium nitrate (AN), 6 % H_2O, 16 % methanol (CH_3OH)), which are being used in United States and Japan, respectively.

Although many studies were carried out on HAN binary and ternary mixtures, most of the studies were only limited to binary HAN and common HAN ternary propellants. By studying more fuel options, it could provide more insightful information into the mixture feasibility for targeted application. It was also shown that certain HAN formulations work with specific catalyst [16]. Lower number of carbon atoms was preferred for fuel option to prevent formation of carbonaceous residue, which will increase difficulty in obtaining a reproducible result [17]. Moreover, HAN-methanol samples had lower decomposition rates than 13 *M* HAN [16].

Methanol has the lowest number of carbon atoms in alcohol family, thus it was used in formulation of SHP 163. The difference in propellant composition was demonstrated in a SHP 163 case study, with respect to the amount of methanol present. Methanol was found to suppress high linear burning rate of HAN binary solution and instability of hydrodynamic instability during decomposition [18]. Addition of hydrazine nitrate (HN) to HAN-based propellant inhibited HAN self-sustaining combustion but also stabilized the sudden temperature increment during HAN decomposition [19]. Continuous effort is required to seek the most suitable blend to give the best performance.

1.3.3 Ceramic microthruster cracking issue

As combustion of propellant releases large amount of heat energy, advanced ceramic material has been used as structural material in micropropulsion system to overcome the high reaction temperature of

chemical propellants [20]. Ceramics is a class of refractory material offering high strength and stiffness, with good chemical inertness and unique mechanical properties at elevated temperature. Ceramics, with low thermal conductivity (2 *W/m.K*), makes it an ideal material for development of efficient micropropulsion system [21].

Low-temperature co-fired ceramic (LTCC) thruster with silver electrode was first employed to study electrolytic decomposition of HAN-based monopropellant at microscale. However, ceramic microthruster cracked after the testing due to high thermal stress, suggesting the importance of controlling the reaction rate to avoid the associated pressure build up from exceeding the limit of material properties of ceramic [22].

Much in-depth knowledge of micro-scale electrolytic decomposition, in particular the reaction rate, of HAN solution in both binary and ternary mixture paves a solid foundation towards the development of an efficient microscale reactor for various energetic applications, for example propulsion, gas generator, combustor, power generation *et cetera* in the future.

Meanwhile, a commonly used polymer, polymethyl-disiloxane (PDMS), on the other hand, is a polymer featuring low strength and stiffness but high chemical resistance. Thermal conductivity of PDMS (0.15 *W/m.K*) is comparable to that of ceramics [23]. Unique optical transparency of PDMS makes it a potential candidate to be studied using

visualization technique. Its high viscoelasticity enables it to be molded easily as well.

1.4 Research scope and novelty

Driven by aforementioned issues, the primary research objective of this project is to study the decomposition phenomena in an efficient microreactor system with HAN-based propellant and improve in current design. Current work is divided into two major stages, i.e. testing of HAN ternary mixtures and improvement of current microreactor design.

The novelties of this project are summarized as follow:

1. Study the effect of fuel addition and effect of electrochemical parameter of HAN ternary mixture towards electrolytic decomposition performance of HAN mixture at macroscale (Chapter 3). The fuel studied are methanol, ethanol, propanol, dextrose, sucrose, urea and ammonia.

2. Development of a cost-effective approach to reduce pre-ignition delay to visualize electrolytic decomposition of HAN binary solution in PDMS microreactor and study the decomposition phenomena (Chapter 4). HAN decomposition could also be studied more in-depth using visualization technique.

3. Study the effect of parameters affecting electrolytic decomposition performance of HAN ternary mixture at microscale and determine the most contributing parameter (Chapter 5). The parameters

studied include number of electrodes pair, HAN flowrate and applied voltage.

In Chapter 2, a comprehensive literature review was carried out. Different ionic liquids and decomposition techniques were discussed. The review provided a clear guide in concluding the ionic liquid and decomposition technique that were employed in this study.

In response to low efficiency of HAN decomposition, Chapter 3 discussed the relationship between electrochemical parameter and HAN decomposition performance. Electrolytic decomposition of HAN ternary mixture performed in a thermally insulated beaker is proposed to address the macroscale study of HAN ternary mixture by studying the parameter which could contribute to the improvement. Seven HAN ternary mixtures were studied, including HAN-methanol, ethanol, propanol, dextrose, sucrose, urea and ammonia. Upon performing the macroscale decomposition experiment, performance of the HAN decomposition was analyzed and compared among the fuels tested.

Due to the nature of electrolytic decomposition, the effect of electrochemical parameter, i.e. conductivity of mixture, towards HAN decomposition performance was studied. The outcome of the study bridged the knowledge on effects of electrical conductivity towards electrolytic decomposition of HAN ternary mixture. The work also served as a screening of suitable fuel components in HAN ternary mixture for future studies in microreactor device.

Being the most important phase, majority of this research effort was devoted to improve the current microreactor system, which was described in Chapter 4. With the advancement in microfabrication technique, cutting plotter was utilized to create a master mold for the microreactor design. As such, microreactor could be fabricated using a more cost-effective approach, due to lower start-up cost and shorter fabrication time required. Double pole single throw (DPST) switch integration into the visualization system also greatly reduce the total cost of the experimental setup.

In Chapter 5, the cracking issue in ceramic microthrusters that was mentioned was tackled by studying overall reaction rate of HAN solution decomposition. The rate of change of bubble area to the maximum point in fabricated PDMS microreactor was used, as both PDMS and ceramic have similar heat conductivity. Parametrical studies was carried out to study the factors affecting the overall reaction rate. The parameters were then optimized to achieve the highest overall reaction rate in the microreactor system. Visualization of the HAN decomposition phenomena extends the knowledge of HAN decomposition.

Chapter 6 summarizes all the activity described in this work. Several recommendations are made in the section of future work.

Chapter 2 Literature Review

2.1 Ionic liquid propellants

Discovery of energetic ionic liquids (EILs) was made in the late 1970s as liquid gun propellant (LGP) [24-26] and arise of development problems cause them to be discarded for this particular application [11, 27]. The research was abandoned until recently, replacement of conventional rocket fuels such as hydrazine (N_2H_4) and hydrogen peroxide (H_2O_2) were proposed. However, high toxicity and associated handling costs of hydrazine and instability of H_2O_2 during storage prohibited them to be used in rapid research works [11, 28].

Promising high energy output upon combustion was shown by first family of EILs, namely ammonium dinitramide (ADN), hydrazinium nitroformate (HNF), and hydroxylammonium nitrate (HAN). They are green propellant as they have lower toxicity and more environmental friendly, as compared to conventional propellant. They exhibit excellent oxygen balance ranging from 20 % (HNF) to 33 % (HAN) and low melting point, as low as 48 °*C* (HAN), which are critical for combustion as less energy input is preferred [29, 30]. The oral median lethal dose of each propellant was benchmarked against hydrazine, as shown in Figure 2.1 [31, 32]. All green propellants have much lower toxicity as compared to hydrazine, which made green propellants more desirable than hydrazine.

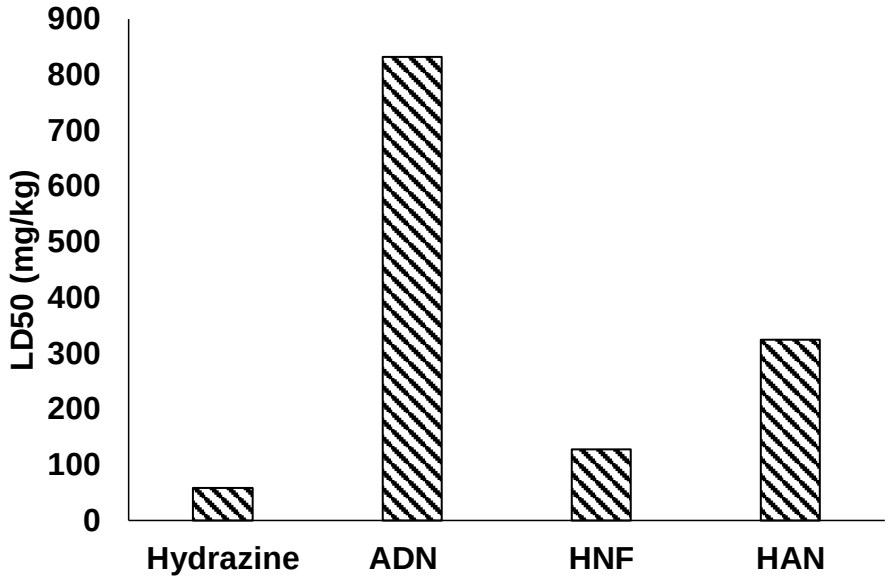

Figure 2.1 Lethal dose of each green propellant, as compared to hydrazine, shown as LD_{50} level [31, 32].

Therefore, the next subsection consists of advantages and disadvantages of these EILs (ADN, HNF and HAN), starting with introduction of ADN, followed by highlight on its production and combustion mechanism. Other EILs family, such as HNF and HAN, will be introduced in the later section. In addition, future prospects of these EILs will be taken into consideration before conclusions are drawn.

2.1.1 Ammonium Dinitramide (ADN)

ADN is a white solid salt, having an oxygen balance of 25.79 % [33], mainly served as an oxidizer for solid rocket fuel [29]. Though it was first synthesized in 1971 in Moscow, USSR [34], it was not until 1988 that the rest of the world knew about it when it was “re-invented” in USA [35].

Research work was started in early 1990s by Swedish Defence Research Agency to develop ADN as a high performance solid propellant in different formulations [36, 37]. Thermal decomposition or catalytic ignition was demonstrated to decompose ADN-based energetic material effectively [38, 39]. ADN solubility in water is 78.1 *wt%* at 20 °*C* and its critical relative humidity is 55.2 % at 25 °*C* , increased its difficulty of storage in humid environment [40].

A few main methods of synthesizing ADN were stated below [41]:

1. Formation of alkyl dinitramide $RN(NO_2)_2$ and subsequent cleavage of R-N bond, leading to dinitramide anion, then ADN reaction

$$R - N(NO_2)_2 \rightarrow -N(NO_2)_2^- + R^+$$

2. Direct nitration of NH_3 or NH_2NO_2 using either NO_2BF_4 or N_2O_5, followed by reaction with a base, can lead to production of ADN

$$NH_3 \rightarrow NH_2NO_2 \rightarrow HN(NO_2)_2 \xrightarrow{NH_3} NH_4N(NO_2)_2$$

3. Nitration of deactivated amines such as NH_2CONH_2 or NH_2COOCH_3 using strong nitrating agents such as NO_2BF_4 or N_2O_5, to form dinitramidic acid, then ADN reaction

$$H_2N - X \xrightarrow{NO_2BF_4 \text{ or } N_2O_5} HN(NO_2)_2$$

X: $-CONH_2$, -COOR

4. Double decomposition reaction of the already synthesized dinitramide salts with respective metal salts, to make organic dinitramide, then purify and ADN reaction

$$MN(NO_2)_2 \xrightarrow{M'X} M'N(NO_2)_2$$

X: -OH, -Cl, -SO_4

However, most of the products here are highly unstable, thus have to be dealt with high precautions. Net equation of thermal decomposition is shown below [42]:

$$NH_4N(NO_2)_2 \rightarrow {NH_4}^+ + {NO_2}^- + 2NO \qquad E_a = 175\ kJ/mol$$

Several issues ADN experienced are humidity, difficulty in production and extremely complex combustion. Its hygroscopic nature required storage in environment with very low humidity, in order to preserve its solid form, which is not readily in space environment. Requirement of low temperature bath or specific chemicals increase the production cost. The complexity of its combustion mechanism hindered further research.

Despite significant results achieved by ADN-based formulations to date, some issues remained unresolved. Specifically, high combustion temperature (1880 °*C*) through catalytic decomposition which surpassed working temperature of catalyst currently available (Shell 405) [43, 44]. New development in ignition method or catalyst, or both is required as

hydrazine share the same distinctive physical and chemical properties as ADN.

In addition, laboratory-scale production of ADN involved pure nitric acid and sulfuric acid, where strict precautions need to be focused on [45]. Furthermore, theory on irregular ADN burning at high pressure needs to be well-grounded, reaction mechanism thermodynamics and transport over high pressure and preconditioned temperature should be investigated thoroughly.

2.1.2 Hydrazinium Nitroformate (HNF)

HNF is a yellow crystal, which is thermally stable below 70 °*C*. Decomposition can start as low as 110 °*C* and violent ignition begin after that [46]. HNF was once a test subject in a large research project as new high-performance propellant in United States during the 60s and 70s.In order to increase the combustion performance as compared to ammonium perchlorate (AP) in composite propellant, it was targeted to replace the conventional powerful oxidizer due to its unique properties of high flame temperature and low molecular weight. Many studies were conducted on various issues of HNF such as safety aspect, computability, toxicity, morphology, and propellant development. Promising experimental results in the initial stage caused the lab scale synthesis of HNF to be scaled up to a yearly production of 300 *kg* [47]. In general, production of HNF is by precipitation reaction between hydrazine (N_2H_4) and nitroform ($HC(NO_2)_3$), as shown in the following reaction [48]:

$$N_2H_4\ (l) + HC(NO_2)_3\ (l)\ \rightarrow\ {N_2H_5}^+.C{(NO_2)_3}^-(s)\ \ \Delta H_{rxn} = -84\ kJ/mol$$

The exothermic reaction takes place in a large temperature-controlled stirring reactor. Initial formation of raw HNF particles is as needle-shaped, orange-yellow crystals. Such formation is undesirable as the rheology of these crystals prevents high loading casting. Re-crystallization of these raw HNF crystals utilized different process, such as evaporation, solvent/non-solvent and cooling crystallization. The overall decomposition reaction of HNF is shown below:

$$HNF\ (l) \rightarrow HC(NO_2)_3\ (g) + N_2H_4\ (g) \qquad E_a\ =\ 171.5\ kJ/mol$$

Fundamental combustion studies of HNF was carried out to study the combustion of loosely packed HNF with a transmembrane domain (TMD) of 75 % in different tube size. Particle size of HNF larger than 100 *μm* in the composite propellant was found to deflagrate independent of the embedding matrix at 6.8 MPa [49]. By decreasing particle size from 280 *μm* to 5 – 10 *μm*, it is less susceptible towards impact and friction [50]. One of the major decomposition products of HNF is NO_2 and continuous reaction leads to higher amount of NO_2. Three distinct zones were found in condensed phase combustion wave, firstly led by inert heating up to 120 °*C*, followed by formation of gas bubbles between 120 °*C* and 260 °*C*, and lastly gasification above 260 °*C* [51]. In addition, model utilizing high and low activation energy (E_a) in condensed phase and gas phase, respectively, agreed well with experimental data on regression rate and temperature sensitivity under laser-assisted

combustion [52]. Addition of vanadium (V) oxide was found to regress 11 times than pure HNF at 0.1 *MPa* [53].

Although much exploration works on HNF usage were attempted, several works remained untouched. For example, HNF solubility in water remained scarce. Water, being a common liquid carrier, served as a stabilizing medium in energetic materials by reducing combustion temperature. Thermal instability in combustion is caused by low water solubility of HNF in water (≈50 *wt%* at 20 °*C*), leading to its potential limit of applications of HNF in other fields, such as chemical micropropulsion. Lastly, three distinctive combustion zones, i.e. primary reaction zone, non-luminous zone and luminous zone, were reported [31] but the mechanisms of chemical reaction remained unestablished. Therefore, analysis of all potential chemical reaction routes was required as further investigation.

2.1.3 Hydroxylammonium Nitrate (HAN)

Hydroxylammonium nitrate (HAN) with chemical formula $[NH_3OH^+][NO_3^-]$ appeared as a new green energetic oxygen-rich ionic liquid recently. Development of HAN solution was initiated as liquid gun propellant in 1976 [26]. Its hygroscopic properties make it hard to be stored in a solid form and always appear in aqueous solution form; however, it has also enhanced the decomposition of HAN by reducing the induction time, as solid HAN has stronger ionic interaction [54, 55]. Its solubility in water is as high as 95 % in weight ratio, present in ionic

form with cation NH_3OH^+ and anion NO_3^-. HAN has other special properties such as high density, low viscosity, low freezing point, easier handling and transport properties [56]. Not only HAN is unique in its physical properties, it is also a chemical that can be synthesized via different approaches as below:

1. Titration of nitric acid and hydroxylamine solution could yield HAN at low temperature bath [57].

2. Double displacement reaction involving conversion of hydroxylammonium sulfate to end product through electrodialysis or cation-exchange process [58]. This method is a complicated batch process and possesses explosion risk during reaction between ion exchange resin and nitric acid.

3. Nitrogen monoxide could be reduced catalytically with hydrogen in a dilute aqueous solution of mineral acid at elevated temperature. By adding sulfur-poisoned platinum catalyst throughout the process, selectivity of HAN could be increased from 60 – 65 % to 86.5 % with high content of nitrous oxide being released in this method [59]. Periodical replacement or regeneration of special catalyst for the process increased the cost and complication of the process [60].

4. Saturated barium nitrate solution could be reacted stoichiometrically with hydroxylammonium sulfate to yield a dilute solution of hydroxylammonium nitrate. Handling and disposal of by-product barium sulfate can be complicated and troublesome. In addition, spontaneous self-decomposition of HAN upon addition of concentrated acid could not be prevented [61].

As general practice, synthesis of HAN normally requires addition of catalyst such as platinum during titration. However, this might also be a handicap of the titration as incomplete removal of the catalyst from the product at end-point could lead to cost-ineffectiveness in long run and could jeopardize its utility. Various HAN concentrations were also produced using electrolysis could be further purified to produce higher HAN concentration, i.e. 83.2 *wt%* [62]. Besides, harmful greenhouse gases such as nitrogen oxides (NO_x) released as by-products possess hazard to human and environment. Pristine HAN solution of different concentrations could either be obtained commercially (24 or 80 *wt%*) or could be affected by concentration of starting materials (hydroxylamine and nitric acid). Purification of HAN such as distillation or evaporation are simple but not desired as the heat involved might result in decomposition of HAN [63].

Much works have been carried out to study on combustion of HAN. As one of the main component in HAN solution, presence of water in the system acts as system stabilizer by reducing combustion temperature [30] and affect the oxidation state of active metal in catalytic decomposition [64]. Both modelling and experimental data came into good agreement that deflagration of HAN solutions was limited by rate of proton transfer from hydroxylammonium cation to nitrate anion [65]. Autocatalytic reaction, which also means self-decomposition, occurs at sufficiently high nitric acid concentration, are also affected by temperature of the solution [66]. The presence of iron ion exhibited catalytic effect on HAN autocatalytic reaction [67].

In addition, simulations and experimental works were carried out on the chemical kinetics and mechanisms involved in thermal decomposition, with conclusion that the rate of determining step proposed was in line with previous postulation, which is the proton transfer reaction [68]. Study on combustion behavior of different HAN concentrations concluded linear proportional relationship between the performance of HAN solution to chamber pressure [69]. In general, thermal decomposition of HAN is limited by proton transfer reaction, incorporating water effect [54, 65, 68, 70-73], as shown below:

$$HAN + H_2O \rightarrow NH_2OH + HNO_3 + H_2O \quad E_a = 63.178\ kJ/mol$$

In spite of the findings above, several important issues remained unresolved. For instance, simplification of proposed kinetic equations leading to incomplete understanding towards complete combustion mechanisms of HAN solution (9, 10.7 and 13 *M*) [70]. Besides, parameter that affects reaction time such as the residence time, which has potential to harvest extra energy, is not fully understood. Improvement is required to bridge the gaps of knowledge in this process. Physicochemical properties of three ionic liquid propellants were summarized in Table 2.1.

Table 2.1 Comparison between three ionic liquids, in terms of physical and chemical properties.

Properties	**Ionic liquid**		
	ADN	**HNF**	**HAN**
Common form	Solid	Solid	Aqueous solution
Oxygen balance (OB%) [29]	26	13	33
Density in solid state (*g/cm³*) [74]	1.81	1.91	1.84
Melting temperature (°*C*) [30]	91	124	48
Solubility in water at room temperature (*wt%*) [56]	80	50	95
Critical relative humidity (%)	55.2 [40]	-	-
Activation energy (solid) (*kJ/mol*)	155 [75]	150 [76]	66 [68]
Ease of synthesis	Hardest	Easiest	Medium
Volumetric thrust	Medium	Lowest	Highest
LD_{50} oral (*mg/kg*) [77, 78]	832	128	325

Onset temperature is the temperature at which the propellant started to decompose. Onset temperature is proportional to heat energy required for the decomposition to occur.

Table 2.2 Onset temperature of each propellant with respective concentration [30, 64].

Concentration of propellant (*wt%*)	**HNF**	**ADN**	**HAN**
	Onset temperature (*°C*)		
40	130	-	180
50	-	152	-
60	-	128	175
75	-	116	-
95	-	-	155

According to Table 2.2, both onset temperature of HNF (130 vs 180 °*C* at 40 *wt%*) and ADN (128 vs. 175 °*C* at 60 *wt%*) are lower than that of HAN . A full comparison was not able to be quantified as HAN used in these two studies gave different results, due to different concentration used in the studies [30, 64]. However, HNF has a lower onset temperature (130 °C at 40 *wt%*) than ADN (152 °C at 50 *wt%*). Onset temperature is lowered with increased concentration, as shown in both HAN and ADN case, due to lower stabilizing effect of water, as a result of lower water content. The onset temperature of HAN and ADN is decreased from 175 °*C* (60 *wt%*) to 155 °*C* (95 *wt%*) and 152 °C (50 *wt%*) to 116 °C (75 *wt%*), respectively.

From the findings above, HAN has highest onset temperature among these three candidates (HNF, ADN, HAN), indicating HAN has the highest starting energy among these three energetic materials. This also shows that HAN is safest, in comparison. Thus, other decomposition method such as catalytic decomposition or electrolytic decomposition methods are required for more efficient HAN decomposition.

A study conducted on thermal analysis of similar concentration of HAN and ADN (60 *wt%*) [64] shows that HAN gave higher pressure rise and evolved gas temperature (166 *mbar* and 178 °*C*) than ADN (135 *mbar* and 105 °*C*). Another thermal analysis study of similar concentration of HAN and HNF (40 *wt%*) showed HAN had higher pressure rise (50 *mbar*) than HNF (40 *mbar*) [30]. Although onset temperature of HAN is higher than that of ADN and HNF, the temperature of gas evolution and pressure rise is also higher than that of ADN and HNF [79]. Higher pressure rise and evolved gas temperature showed that larger thrust and higher decomposition completion were obtained, respectively.

Higher HAN concentration (95 *wt%*) could be obtained than HNF (50 *wt%*) in aqueous solution form. Higher HAN concentration could lead to larger energy release, which might lead to larger damage to the structural properties of the reactor due to higher temperature. Catalytic decomposition of HAN can be initiated even without complete removal of water, as compared to ADN [29], leading to a more efficient decomposition of HAN.

This section concludes advantages and disadvantages of ADN, HNF and HAN. Having considered the feasibility of synthesis in laboratory scale, ease in storage and handling properties and also safety properties, HAN was chosen as a subject of study in this project. Different decomposition methods and mechanisms involved will be further reviewed and discussed in the next section.

2.2 Decomposition techniques and reaction mechanisms of HAN-based propellants

2.2.1 Thermal decomposition

Thermal decomposition is the most basic and commonly used decomposition technique for HAN solution, either in analysis or in propulsion. Thermogravimetric analysis (TGA), differential thermal analysis (DTA), strand burner and batch reactor are common thermal analysis tools utilized to examine decomposition characteristics of HAN solutions at various concentrations. They can also be used to compare performance with addition of different fuel components [80, 81]. They also often served as a benchmark prior to catalytic decomposition [30, 57, 82].

Meanwhile, important benchmark such as burning rate, onset temperature, temperature change and pressure rise are the performance indications of the propellants. Results show that endothermic evaporation of water took place before occurrence of exothermic reaction

of HAN. HAN concentration is directly proportional and inversely proportional to temperature change of exothermic decomposition and onset temperature, respectively [57, 64].

Comparison between burning rate of two HAN-methanol formulations (HAN269MEO15: 69.7% HAN, 0.6% Ammonium Nitrate, 14.79% Methanol, 14.91% H_2O and HAN284MEO17: 77.25% HAN, 0.67% Ammonium Nitrate, 17.19% Methanol, 4.89% H_2O) found that burning rate curves at low pressures are nearly parallel, suggesting high similarity between the burning rate controlling mechanisms of these two formulations. Two and five distinct regimes were identified in burning of HAN284MEO17 and HAN269MEO15, respectively, in which burning rate of HAN269MEO15 was found to be correlated with pressure exponent [83]. Furthermore, methanol was found to be effective in suppressing burning rate [84, 85]. A slight adjustment in the original HAN formulation was found to affect onset temperature. In addition, addition of HNO_3 and NH_2OH was found to increase and decrease the onset temperature, respectively [85].

Addition of fuel to HAN is of interest mainly due to the higher energy density which can be harvested, as compared to binary HAN solution [16]. The other advantage of adding fuel into this system is the ability to reduce and control the burning rate of HAN mixture, thereby reducing the damage to reactor. Advantages and disadvantages of adding fuel into binary system were tabulated in .

Table 2.3.

Table 2.3 Advantages and disadvantages of using binary and ternary HAN mixture.

	Advantages	**Disadvantages**
Binary HAN solution (HAN + H_2O)	• Less complicated decomposition mechanism	• Low energy density • High burning rate
Ternary HAN mixture (HAN + H_2O + Fuel)	• High energy density • Possibility to alter burning rate	• More complex decomposition mechanism

To further study the overall decomposition process, detection and analysis of species evolution throughout thermal decomposition of HAN-based propellant helps achieve better understanding in the chemical kinetics and reaction mechanisms. Thermolysis and laser assisted combustion coupled with analytical tools such as FTIR and TQ-MS were used to study decomposition products of HAN-based ternary mixture, such as XM 46 / LP 1846 (60.8% HAN, 19.2% TEAN, 20% H_2O) and LP 1845 (63.2% HAN, 20% TEAN, 16.8% H_2O) [54, 71, 86]. Decomposition sequence for binary HAN solution (HAN and water), solid triethyammonium nitrate (TEAN) and LP 1846 are displayed in Table 2.4.

Table 2.4 Comparison of decomposition sequence of HAN, TEAN, LP 1845 and 1846 in different literatures.

Method / Component	Decomposition sequence	
	[54]	[86]
	Confined rapid thermolysis (Up to 1500 *K/s*)	High power CO_2 laser (up to 10000 *K/s* and heat flux 400 W/cm^2)
HAN	1. Induction period 2. Water evaporation 3. Formation of HNO_3 4. Formation of NO_2 (brown gas)	1. Delay where water boil away 2. Emission of brown gas 3. Ignition of sample 4. Burn with white flame
TEAN	1. Decompose near 260 °*C*, higher than its melting point of 81 °*C*	1. Melting 2. Exhibition of two sequential flames: an initial blue flame, followed by bright yellow flame
XM46 (LP 1846)	1. Evaporation of water 2. HAN decomposition 3. TEAN decomposition	1. Initial gas evolution during ignition delay 2. HAN+TEAN reaction dominated by HAN (White flame) 3. HAN+TEAN reaction dominated by TEAN (Blue and yellow TEAN flames)

Results of these experiments show a general sequence of release of gas species, starting with water evaporation, followed by HAN-dominated reaction for HAN binary system or triethylammonium nitrate (TEAN)-dominated reaction for HAN ternary system but the product gas species released might differ in each study due to variation in test conditions [54, 71]. They show a good agreement in the phenomena of decomposition sequence. Formation of flame requires high heat flux (400 W/cm^2) and no flame is observed under hear flux of 100 W/cm^2. Mutual interaction of HAN and TEAN in XM46 (LP 1846) was suggested as a result of the increased reaction rate, compared to corresponding independent materials [86]. Decomposition on HAN-methanol ternary system began with water and methanol evaporation, followed by HAN decomposition [81]. These studies show that the initiation of HAN-based mixtures began with more volatile components.

A chemical kinetic study of HAN solution decomposition was proposed to further improve the understanding on mechanisms of thermal decomposition of HAN solution. The study took into consideration of complex reactions and validated with experimental data, giving a simplified global reaction model for HAN decomposition. Mechanisms involved in thermal decomposition of HAN solution are listed below in Table 2.5 [70]:

Table 2.5 Kinetic equations and their respective activation energy.

Kinetic equations	Activation energy (*kcal/mol*)
1. $HAN + H_2O \rightarrow NH_2OH + HNO_3 + H_2O$	15.1
2. $NH_2OH + HNO_3 \rightarrow HONO + HNO + H_2O$	6.6
3. $NH_2OH + HONO \rightarrow N_2O + 2\ H_2O$	3.3
4. $NH_2OH + HNO \rightarrow N_2 + 2\ H_2O$	2.7
5. $3\ HONO \rightarrow 2\ NO + HNO_3 + H_2O$	9.1
6. $2\ HNO \rightarrow N_2O + H_2O$	17.1
7. $HNO + HNO_3 \rightarrow 2\ HONO$	16.6
8. $HONO + HNO_3 \rightarrow 2\ NO_2 + H_2O$	0.7

As observed in Table 2.5, nitrogen dioxide (NO_2) and water vapor (H_2O) are expected to dominate among the decomposition products (Equation 8) due to the lowest energy barrier according to the thermal decomposition kinetic equations listed in *Lee*'s work [54] and Equation 6 is expected to be least favorable due to its highest activation energy. However, simultaneous consumption of nitrous acid (HONO) and production of nitric acid (HNO_3) in Equation 5 led to formation of the initial reactants in Equation 2 and Equation 3. Thus, Equation 5 is expected to occur more frequently than Equation 8. Involvement in breaking a triple bond requires much higher energy to overcome the energy barrier, as shown in Equation 6. Equation 4, having the second least activation

energy, will be the leading reaction, leading to main product of thermal decomposition of HAN to be nitrogen gas and water.

Thermal decomposition of binary HAN is first led by water evaporation, because water has a lower boiling point, followed by the chemical rate determining step, which is proton transfer from NH_3OH^+ to NO_3^-, giving out NH_2OH and HNO_3 (Equation 1) [55, 65, 68, 71-73, 87]. Ignition step, reaction between hydroxylamine and nitric acid (Equation 2), took place after. Next, six simplified model of kinetic equations occur simultaneously and release various gas species (Equation 3-8). Rate determining step during the induction period is significantly influenced by water content in HAN solution, according to findings listed [54, 86, 87].

Meanwhile, modelling works were also carried out on HAN-based propellant in addition to the experimental works, with the aim to understand the reaction mechanisms, studying the autocatalytic behavior and its utility in rifle [67, 88-90]. Combustion of a ternary system, HAN-water-TEAN solution, could be broken down into three stage reactions, namely initiation step, ignition and combustion. First, production of heat and gases occurred during initiation step [91], followed by release of heat as reaction became self-sustained, and lastly most of the energy stored in the solution released during combustion step. These findings are supported by a proposal of similar trends of reaction kinetics in all three stages of combustion [55]. As other gas species such as HONO and N_2 were favored, formation of NO_x resulted from thermal decomposition of HAN-based propellant remained to be studied.

Summary of reaction mechanisms of gas-phase reaction of HAN was done and shown in Table 2.5.

Extension work based on Table 2.6 was then developed in which a theoretical reduced reaction model was constructed to deduce Arrhenius-type reaction rates for decomposition of HAN binary system [70]. The addition of those intermediate species had increased the model accuracy, such as the formations of HNO_2 and NOx. Besides, dimerization of HNO was also proposed as a possible pathway of N_2O formation: $2HNO \rightarrow N_2O + H_2O$ (E_a 17.1 *kcal/mol*) [73, 92, 93] but this reaction was of minor importance compared to reaction between NH_2OH and HONO to form N_2O due to lower concentration of HNO compared to HONO in the condensed phase in thermal decomposition [70]. Another possible chemical reaction, which is of lower activation energy, 9.1 *kcal/mol*, was added into the reduced modelling reaction mechanism: $3HONO \rightarrow 2NO + HNO_3 + H_2O$, in order to account for higher NO concentration compared to NO_2 [70]. It is concluded that the proposed simplified kinetic equations for thermal decomposition of aqueous HAN solutions were sufficient for basic understanding. However, the study could be further extended so that thermal decomposition behavior of HAN solution could be further understood.

Table 2.6 Comparison of thermal decomposition reaction mechanisms of HAN as proposed by different research groups.

	Klein [91]	**Oxley & Brower [55]**
Initiation	$HAN \leftrightarrow NH_2OH + HNO_3$ $NH_2OH + HNO_3 \rightarrow HONO + HNO + H_2O$	$HAN \leftrightarrow NH_2OH + HNO_3$ $NH_2OH + HNO_3 \rightarrow HONO + HNO + H_2O$
N_2O formation	$NH_3OH^+ + HONO \rightarrow H_3O^+ + O{=}N{-}NH{-}OH$ $\leftrightarrow OH{-}N{=}N{-}OH \rightarrow N_2O + H_2O$	$NH_2OH + HONO \leftrightarrow N_2O + 2H_2O$
N_2 formation	$NH_3OH^+ + HNO \rightarrow N_2 + H_2O + H_3O^+$	$NH_2OH + HNO \rightarrow N_2 + 2H_2O$
NO_2 formation	$HONO + HNO3 \rightarrow 2NO_2 + H_2O$ $2HONO \rightarrow NO + NO_2 + H_2O$	None
Other reaction	$HNO + NO_3^- \rightarrow HONO + NO_2^-$	$HNO + HNO_3 \rightarrow 2HONO$

2.2.2 Catalytic decomposition

Catalytic decomposition of HAN-based liquid propellant (LP 1846) was first demonstrated with Shell 405 catalyst (30 % Ir/Al_2O_3), which was previously employed successfully in hydrazine decomposition [16]. However, higher theoretical combustion temperature of HAN (2093 °*C*) caused shorter catalyst life due to sintering of catalyst, compared to hydrazine, as it is commonly operated below 1100 °*C* [12, 16]. Moreover, reaction rate of HAN is lower than that of hydrazine due to inferiority to hydrazine in catalytic activity [94].

Conventionally, catalytic decomposition required catalyst to be preheated in order to have an effective decomposition. The presence of appropriate catalytic active phases leads to a drop in the onset temperature, revealing that decomposition can be triggered at lower temperature, even in the presence of water. The reaction rate is larger by comparison with thermal decomposition [64, 81]. Ignition delay, chamber pressure and catalyst bed temperature are useful indicators of catalyst efficiency [95]. Possible paths of reactions of HAN undergone when in contact with catalyst [64]:

$$NH_3OHNO_3\ (aq) \rightarrow 2H_2O\ (l) + N_2\ (g) + O_2\ (g) \qquad \text{R2-1}$$

$$NH_3OHNO_3\ (aq) \rightarrow 2H_2O\ (l) + \tfrac{1}{2}N_2\ (g) + NO_2\ (g\ or\ l) \qquad \text{R2-2}$$

$$NH_3OHNO_3\ (aq) \rightarrow 2H_2O\ (l) + 2NO\ (g) \qquad \text{R2-3}$$

$$NH_3OHNO_3\ (aq) \rightarrow 2H_2O\ (l) + N_2O\ (g) + \tfrac{1}{2}O_2\ (g) \qquad \text{R2-4}$$

Oxidation of catalyst during reaction, loss of catalyst surface area and active metal (sintering) caused by high temperatures were

considered as major indications for catalyst deactivation. The issue worsening in hot steam environment. Increased reaction time resulted in catalyst performance decay. Presence of steam in HAN/fuel combustion increases severity of operating environment, causing damage to the catalysts [12, 95, 96]. In addition, addition of TEAN into the fuel system leads to non-reproducible results due to formation of carbonaceous deposit on catalyst. [17].

Adherence of active metal in Shell 405 catalyst was observed for a 30,000 *seconds* testing in a test chamber, with a rapid decline of catalytic activity after 20,000 *seconds* [94]. High molecular weight of HAN/fuel combustion exhaust gases requires chamber temperature to be maintained at optimum level in order to keep specific impulse (I_{sp}) at acceptable levels, thus utilizing more energy [12]. Mechanical breaking has been observed due to strong exothermic decomposition of aqueous HAN and can be avoided by preheating at 100 °*C* [97]. Catalyst wear rate with respect to total flow rate for the propellant was 6 % for fine particles and 2 % for coarse particles. The catalyst experienced greater wear than the case with hydrazine [19].

Aqueous HAN solutions was decomposed catalytically at temperature as low as 40 °*C* in 2004, with an ignition delay less than 1 *s* [98]. In a recent study, HAN solution could be ignited lower than room temperature (20.7 °*C*) in the presence of Ir/SiO_2 in a thermogravimetric study [99]. Over 8000 s of cumulative operation have been demonstrated

on single laboratory thruster and catalyst bed, showing high restartability of HAN with catalyst [12].

Catalyst material is the main component for catalytic decomposition studies. The lowest ignition/onset temperature is the crucial performance indication in catalytic decomposition studies. In order to obtain the most suitable material for catalytic decomposition purpose, effect of different catalyst metal, support and fuel were studied. Catalytic combustion was favored at microscale due to high area to volume ratio and small length scales. It is slower than gas-phase combustion and energy is deposited directly into thruster body [100].

Onset temperature was found to be lowest employing catalyst with both support and active phase (75 °*C*), as compared to the case of catalyst with only support (105 °*C*) and without catalyst (128 °*C*) [17]. Unsupported platinum group metals was proven to be best metal catalyst among the injection testing of HAN solution in earlier years [94]. Onset decomposition temperature for platinum on alumina support was higher than 40 °*C* [96, 98].

Screening of catalyst metal was done effectively by simulation using adsorption analysis on LP 1846. Iridium (Ir) was found to have the best adsorption among a group of metals such as Ru, Rh, Pd, Ir, Pt, showing it to be the best catalyst [94]. Later on, experimentation works carried out to verify such results on 80 *wt%* HAN solution. Ir supported on SiO_2 displayed the lowest ignition temperature (20.7 °*C*) for HAN [99].

In a latest study, Ir-based catalyst was found to be effective in reducing onset temperature of HAN decomposition. The difference in product gas species between thermal and catalytic decomposition was not obvious, showing possibility on similar kinetics. The presence of HNO_3 in the product gas of catalytic decomposition, showing it cannot be decomposed in both cases, and that catalyst does not change product species but only reducing onset temperature [101].

Impregnated catalysts display higher activity, owing to smaller crystallite size of supported metallic particles [98]. However, another study shows that higher dispersion and smaller particle size were not favorable for obtaining high activity, indicating that the effect of particle size towards activity is not indefinite [99]. Both powdered and shaped platinum supported on doped alumina catalysts remain active after 23 injections at 45 °*C* displaying non-inhibiting effect of shaping [97].

In an isothermal tests at 50 °*C*, powder catalyst (50 *μm*) displayed best activity with a complete decomposition of HAN solution, by having good contact with monopropellant, as compared to sphere catalyst (1.5 *mm*). Presence of preferential paths on the catalyst bed, causes the propellant to have less contact with catalyst, indicating that sphere-shaped catalyst is not suitable as catalyst bed [102].

Xerogel and aerogel are two different treatment for same alumina support in the study. Although aerogel support has higher specific surface area, better thermal stability at high temperature (1200 °*C*) and are more homogeneously dispersed than xerogel support, lower catalytic

activity at low temperature and higher onset temperature were obtained in comparison with xerogel support [98]. This shows that different treatment for the same metal catalyst and support show different results, such as higher reaction rate or reduced decomposition temperature [103].

Two similar studies on catalytic decomposition of HAN solution were compared with the results in Table 2.7. Alumina (Al_2O_3) doped by lanthanum oxide (La_2O_3) with 10 % iridium content was used [64] while alumina doped by silicon with 10 % platinum content was used in another study [103]. It is noteworthy to mention that surface area of Ir/Al_2O_3-La_2O_3 (230 m^2/g) is higher than that of Pt/Al_2O_3Si (44 m^2/g). The usage of 80 *wt%* HAN solution also contributed to better decomposition performance, highlighting the importance of concentration in the decomposition. Comparison between monolith and grain catalyst shows that high reactivity could be achieved using good contact between solid and liquid phases and enhanced heat and mass transfer [104].

Table 2.7 Comparison on catalytic decomposition of HAN solution.

	[64] Amrousse *et. al.*	[103] Amariei *et. al.*
HAN concentration (*wt%*)	80	79
Catalyst used	Ir/Al_2O_3-La_2O_3	Pt/Al_2O_3Si
Mass of catalyst used (*mg*)	8	16
Catalyst surface area (m^2/g)	230	44
Volume of HAN solution (*µl*)	5	10
Pressure increment (*mbar/s*)	260	169
Onset temperature (°*C*)	42	90

Possible pathways leading to drop in decomposition performance was illustrated in Figure 2.2 [96]. Theta alumina structure remained unchanged after the catalytic reaction. Owing to heterogeneous distribution of silica and platinum particles, formation of nanosized platinum agglomerates was responsible for efficient decomposition of HAN. Low metal-silica interactions lead to migration of metallic particles, which are responsible for sintering of smallest crystallites and dislocation of aggregates.

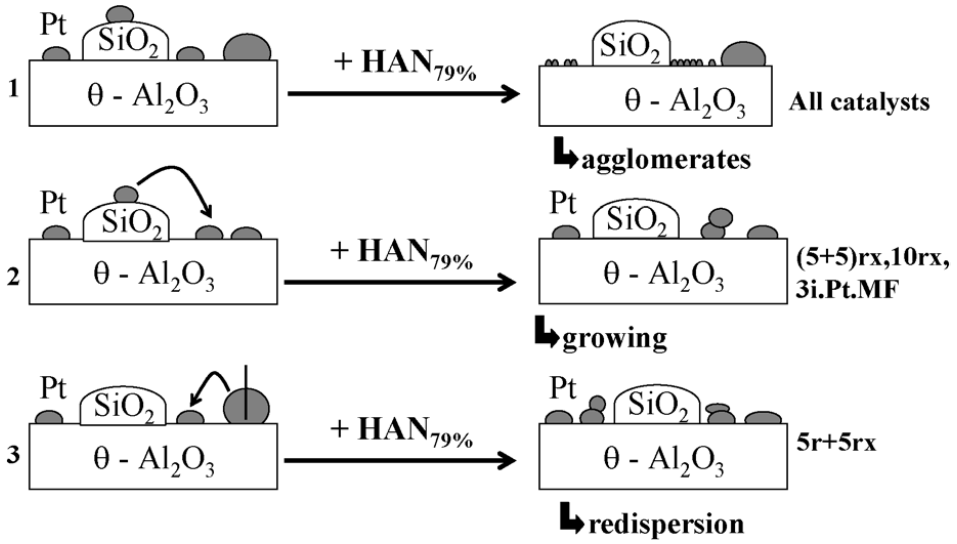

Figure 2.2 Scheme displaying the transformation of platinum particles during the reaction of HAN 79 % decomposition on catalysts [96].

Fuel was found to affect catalyst performance by interacting with catalyst when present. Presence of water and methanol was found to disturb the interaction between HAN molecules and catalysts [81]. HN addition realized a reliable catalytic ignition and combustion characteristics with 1 – 20 *N* class thrusters by inhibiting self-sustaining

combustion. CO_2 was detected and gradual decrease in N_2O amount throughout combustion of HAN/HN blend, indicating that HN accelerates the decomposition process of HAN-based monopropellants [19].

The chosen molecular fuels were found to have strong inhibiting effect on the catalytic decomposition at low temperatures [11]. In a comparison study, for stoichiometric mixtures, HAN was able to oxidize glycerol more completely than HNF and ADN. Moreover, the highest catalytic effect was displayed in HAN-based solutions with a drop in ignition temperature of approximately 100 °*C* [39].

Good candidate of fuel must contain limited number of carbon atoms to avoid formation of carbonaceous residue during cold start as it has a catalytic effect towards HAN decomposition, increasing difficulty in obtaining a reproducible results. By reducing percentage of carbon dioxide in gas exhaust composition, it can lead to a decrease of specific impulse for a determined maximum final temperature [17].

Platinum is the most active phase to break the HAN-H_2O_2-H_2O mixture. The catalyst MnO_x-Pt was the best to decompose such mixture. The MnO_x catalyst base remains the most effective for decomposition of HAN-H_2O_2-H_2O at room temperature. This shows the influence of fuel towards decomposition performance [74].

Although catalytic decomposition of HAN could be started at room temperature with the use of iridium metal, the decomposition did not complete in single step, with the remaining HAN solution to be completely decomposed at approximately 80 °*C* [99]. Thus, other key factors that

influenced catalytic activity of iridium need to be studied. Complete decomposition of HNO_3 is required to achieve best performance of HAN-based monopropellant [101]. Further work in reducing load on catalyst and improving catalyst charge method are required to reduce wear on catalyst [19]. Suitable catalyst for HAN decomposition which can sustain its high combustion temperature and stable for operation in a microsatellite (1 - 2 years) has yet to be found. Long term stability of catalyst is also an issue.

2.2.3 Electrolytic decomposition

In the past decade, alternative methods to initiate decomposition of HAN solution was proposed and tested in US Ballistic Research Laboratory (BRL), such as electrical ignition method [105, 106]. It was proposed that any reaction mechanism competing with proton transfer, which initiates exothermic reaction in HAN thermal decomposition, should lead to decrease in reaction temperature and increase in reaction rate [107]. Additional formation of hydrogen and oxygen from electrolysis of water also could enhance the following ignition and combustion [108]. Besides, electrolytic decomposition has the advantages listed below [109]:

1. Efficient thermal management
2. Ignition at room temperature
3. Reduced power requirement
4. Enhanced system durability and reliability

5. Reduced cost

In recent years, the feasibility of electrolytic ignition concept was first tested with a microfin electrodes, which was used to study electrolytic characteristics of LP 1846 at room conditions [109]. It was then incorporated into ceramic microthruster to show the applicability of achieving ignition in microthruster [22]. Simulation and parametrical studies on HAN binary solution was then carried out, showing that thermal and electrolytic decomposition occurred simultaneously [110, 111].

On the other hand, study on electrification of LP 1846 droplets was carried out in order to provide a reference to the electrical ignition systems of HAN design [112]. A simplified engineering model for ignition delay of LP 1846 droplet was proposed [113], in which the experimental results were further verified by simulation work, which came to a good agreement, with a maximum error of 2.9 % [114].

Electrodes was found to affect electrolytic decomposition performance and sacrificial electrode performs better than inert electrode, in giving higher rate of temperature rise. [115, 116]. Since both copper and aluminum undergo similar electron transfer mechanism, their rate of temperature rise is similar. However, aluminum, which gives out one more electron, the highest temperature achieved is higher than that of copper, showing better decomposition achieved [115]. Applied current and concentration of HAN solution were found to be proportional to the rate of temperature rise [115] and inversely proportional to ignition delay

[110]. Smaller volume shortened the ignition delay, indicating the suitability of applying electrolytic decomposition technique in micropropulsion area [110].

Applied voltage is inversely proportional to ignition delay of LP 1846 [109, 112]. Total energy is inversely proportional with voltage, showing that higher decomposition efficiency is promoted by higher voltage. Higher surface area promoted ease of ions flow though the liquid, reducing the resistance between electrodes plates, therefore increasing the current flow. Despite the change in applied voltage, the final steady-state temperature peaked at 115 °*C*, showing that the maximum liquid temperature was not affected by the initial energy input [109]. Phenomenal changes in LP 1846 droplets upon electrical ignition [112]:

1. Evaporization
2. Periodical expansion and contraction
3. Stronger thermal decomposition
4. Ignition and combustion

Micro-explosion mechanism is formed mainly due to overheated water component and mild liquid phase reaction of HAN is an inducing factor. Ignition delay of LP 1846 droplet is shortened when voltage is increased. Resistance of LP 1846 droplet decreased gradually during electrification of droplet [112]. Proposed reactions mechanisms of electrolytic decomposition of HAN based on electrolysis of water are shown in Table 2.8 [107, 108]. Numerical studies conducted on electrolytic decomposition mechanism, incorporating the existing

reaction mechanisms of thermal decomposition of HAN solution was reported [70].

Table 2.8 Proposed reaction mechanisms of electrolytic decomposition of HAN at both anode and cathode [107, 108].

At anode:	At cathode:
$2H_2O \longrightarrow O_2 + 4H^+ + 4e^-$	$2NH_2OH^+ + 2e^- \longrightarrow 2NH_2OH + H_2$
$H^+ + NH_3OH^+NO_3^- \longrightarrow NH_3OH^+ + HNO_3$	$2H_2O + 2e^- \longrightarrow H_2 + 2OH^-$
$H^+ + NO_3^- \longrightarrow HNO_3$	$OH^- + NH_3OH^+NO_3^- \longrightarrow NH_2OH + H_2O + NO_3^-$
	$OH^- + NH_3OH^+ \longrightarrow NH_2OH + H_2O$
	$NO_3^- + 4H^+ + 3e^- \longrightarrow NO + 2\,H_2O$
	$2H_2O + O_2 + 4e^- \longrightarrow 4OH^-$

Overall equation on both sides of anode and cathode are shown below:

At anode:

$$2NH_3OH^+NO_3^- + H_2O \longrightarrow 0.5O_2 + 2NH_3OH^+ + 2HNO_3 + 2e^-$$

At cathode:

$$2NH_3OH^+ + 2e^- \longrightarrow 2NH_2OH + H_2$$

And the global reaction of electrolytic decomposition is:

$$2NH_3OH^+NO_3^- + H_2O \longrightarrow 0.5O_2 + 2HNO_3 + 2NH_2OH + H_2$$

Till now, only several studies dealt with electrolytic decomposition of HAN. Main work on electrolytic decomposition has been limited to HAN binary solution [110, 115] and LP 1846 only [22, 109, 112, 113, 117]. As from previous understanding, an addition of fuel component can further improve decomposition performance and this area of study has very limited output so far. Effect of adding tertiary fuel component into binary HAN solution nor the chemical decomposition model of HAN tertiary systems are not fully understood, despite electrolytic decomposition can be relatively easy executed. Physical and chemical properties of such mixtures need to be investigated in-depth in order to understand the decomposition mechanisms and obtain an appropriate tertiary fuel component for HAN solution.

2.3 HAN-based micropropulsion systems

In order for each space mission to be executed successfully, specific requirements on the propulsions system is stringent. Various micropropulsion concept is available and the domains of applications was suggested by London. Suitable concept is strongly dependent on mission ΔV (change in velocity) requirement [118].

The domain was reproduced by Bayt [119] and illustrated in Figure 2.3. Obviously, application of micropropulsion system in a mission could not be fulfilled by single micropropulsion system. Introduction of different micropropulsion concepts over the past decades were aimed to meet the requirements. A complete review on state-of-the-art micropropulsion technology was done by London [118] and Mueller [120] in 1997.

As mentioned previously, attitude control and orbital station-keeping was of interest. Liquid chemical thrusters are preferred, as compared to ion thruster, due to the lower electrical energy requirement of such micropropulsion concept [6]. The total required ΔV of such missions are approximately 200 *m/s*, with a minimum thrust requirement of 15 *mN* [118]. Thus, liquid chemical thruster will be considered.

HAN-based propellants belong to the chemical category, as shown in Figure 2.3. With higher performance and lower toxicity than hydrazine, HAN-based propellants are being selected. Governing equations for conventional macroscale combustors no longer applicable to microcombustors. Reactions occurred in the liquid propellant involved

both liquid and gas phase and converted the liquid into gas. This resulted in a flow of both liquid and gas phase, namely two-phase flow, which plays a vital role, if liquid propellant was used. The presence of two-phase flow complicates the conventional fluid mechanics and present more problems than pure liquid or gas flow.

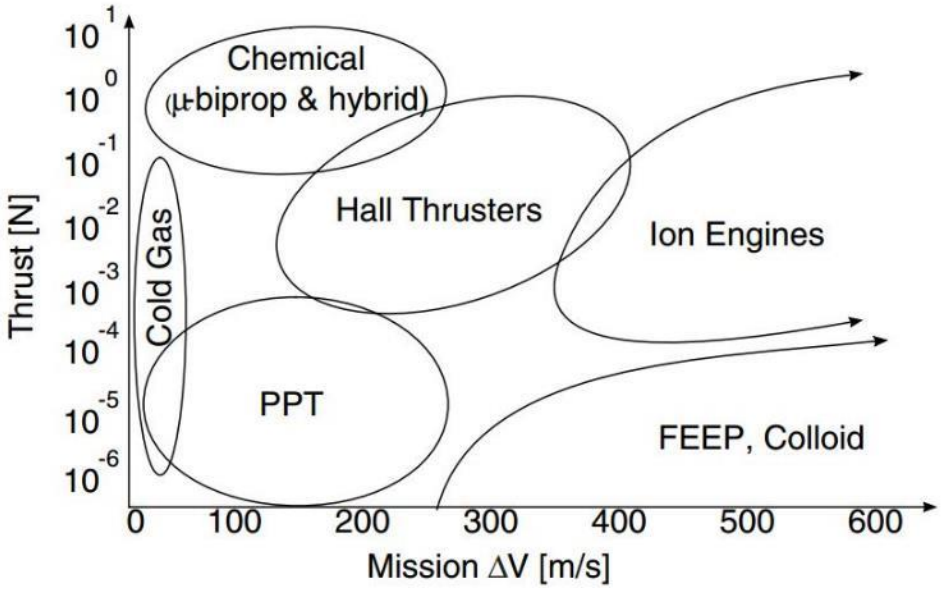

Figure 2.3 Domains of applicability of various micropropulsion concepts, reproduced by Bayt [119] from London [118].

2.3.1 Microreactor fabrication

The microcombustion device proposed in this project is considered an extension of application from microfluidic technology due to the requirement of precision on combustion system design and fabrication. As the dimension is narrowed down to microscale, it could be

easily achieved using suitable microfabrication techniques that are used in conventional microfluidic fabrication technology.

Due to advancements in MEMS technology, many microfabrication techniques are available. Few major factors that need to be considered before a fabrication method was chosen, i.e. precision, type of material used and production cost. Among the available microfabrication techniques, soft-lithography, photolithography and deep reactive ion-etching (DRIE) are some common methods for fabricating microfluidic devices and optimization on these techniques were reported [121-124]. Requirement of sophisticated instruments, clean room facilities and their high costs were the downsides [125].

As a result, a rapid yet low-cost prototyping technology such as xurography and screen printing were proposed to fabricate the microdevices [126, 127]. It is targeted to reduce cost and fabrication interval, as some conventional technique such as laser photoplotting would have a turnaround time of at least 1 day [128]. This technique is defined as quick (less than 2 hours) and high cost-effectiveness of realizing the design into a microfluidic prototype, with the aid of computer-aided design (CAD) drawing. Thus, it offered a great alternative for multiple microfluidic applications. Besides, independence on clean room facilities, low equipment cost, environmental-friendliness, short fabrication time and highly sophisticated steps make this technique to be attractive.

Xurography is one of the common rapid prototyping technique, which uses a cutting plotter to cut various designs on different adhesive vinyl film. It was first proposed in 2005 as an alternative fabrication route for rapid prototyping of microfluidic devices [126]. Moreover, this fabrication technique is compatible with polymeric-based material and metal-based material, such as PDMS and gold respectively [125, 126]. Application of xurography technique was found in various microfluidic studies such as droplet formation study [129], biosensor [130], blood typing [131], hybrid tooling [132] and DNA/RNA extraction [133], demonstrating strong feasibility of this technique, where high reliability and reproducibility could be achieved.

However, the limitation of this technique lies on the consistency of dimension of the microstructures, as most existing cutting plotters could not sustain the consistency and precision of cutting after long period of usage. In addition, vinyl film is incompatible with common laboratory solvents such as toluene and hexane caused disturbance in curing PDMS polymer, if those solvents were added prior curing to aid viscosity reduction [134, 135]. Furthermore, further expansion that utilized vinyl film used in xurography technique was incapable of producing multiple replica molding due to its fragility [136]. Therefore, xurography and epoxy mold technique [137] were combined and used to produce reliable microstructures. The microchannels could be molded using inexpensive epoxy mold. Epoxy molds were fabricated successfully and also can be used on production of multiple polymer-based replica.

Polymeric materials, such as PDMS, exhibit unique characteristics compared to other materials, such as glass and silicon, which are normally being used in microfluidic studies [123]. Ability of polymer to combine with various materials in fabricating microstructure allow it to be used in almost any applications. PDMS is a popular choice as structural materials among polymer-based microfluidic devices due to its unique properties such as optical transparency, low surface energy, higher thermal stability compared to glass, low thermal conductivity and chemical inertness [138].

Despite the advantages, PDMS cannot tolerate harsh operating environment such as extreme temperatures and pressures. In addition, PDMS is incompatible to most organic solvents, especially hexane and toluene, causing it to swell when in contact. The phenomenon may cause material failure after long term usage as the change in shape is irreversible [139]. As a result of the microchannel deformation, it could also lead to inaccuracies in experimental results [140].

2.3.2 Positive and negative molding techniques

There are two molding techniques in xurography method, namely positive and negative molding techniques. Positive molding is the conventional technique used in xurography method, which was first proposed in 2005 [126], while negative molding is a novel technique proposed in 2009 [137] and a similar low cost method was also described [141]. Both positive and negative molding techniques differ in the way the

vinyl film is being weeded, where the outer portion and inner portion are removed, respectively. Both positive and negative molding techniques were illustrated in Figure 2.4.

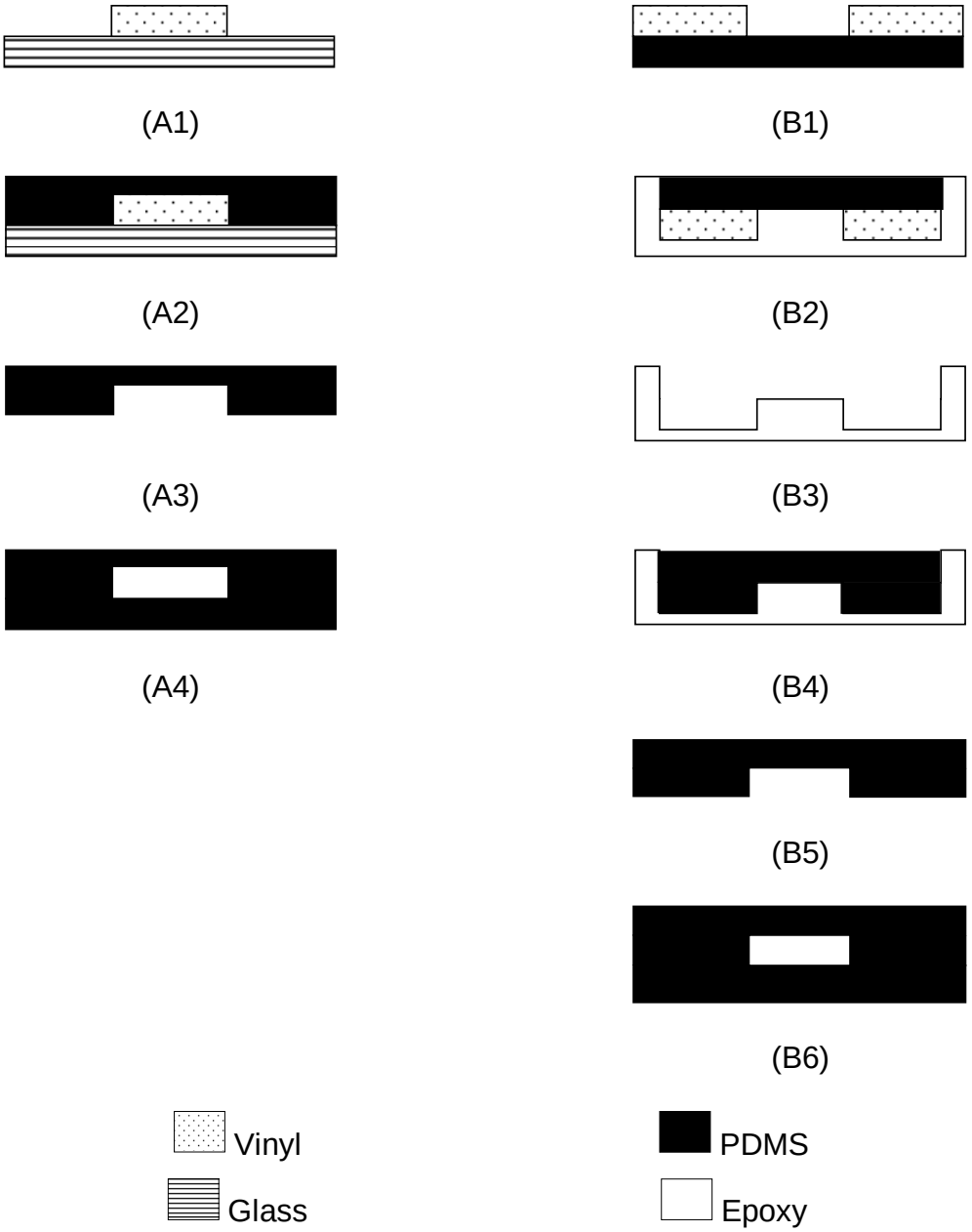

Figure 2.4 Schematic diagram of (A) Positive molding technique and (B) Negative molding technique.

Positive molding technique yields PDMS structures which started with a positive vinyl adhered to a substrate, such as glass, as a master

mold. In positive molding technique, unwanted portion was weeded out, leaving the required microchannel structure behind. Although positive molding technique requires only few steps to complete, the mold might be less durable especially when glass is used as structural material [142].

On the other hand, elimination of utilization of chrome mask in negative molding reduces the cost and turnaround time to less than 2 hours [137]. Negative molding with epoxy resin was also described by Ahmad *et al.* [143]. An epoxy mold is an intermediate in negative molding technique. Although more steps are involved in this technique, the epoxy mold is durable as the design is imprinted onto the epoxy. Advantages and disadvantages of both molding techniques are summarized in Table 2.9.

Table 2.9 Summary of comparison between positive and negative molding techniques.

Molding techniques	Positive	Negative
Pros	• Less steps and time required compared to positive molding • Allow blocks inside microcombustion chamber top layer to be fabricated • Flatter PDMS was molded	• Durable epoxy mold • Consumes less PDMS • No falling off of design occur
Cons	• Less durable mold • Consumes more PDMS • Design might fall off due to less adhesive to surface	• More steps and time required • Formation of curved sides due to surface energy and adhesion to epoxy • Adhesion to surfaces introduced in fabrication steps might cause more problems

2.3.3 Bonding technique

There are several inexpensive methods to bond PDMS, such as partial curing, mechanical bonding and chemical bonding [144-148]. Good adherence between PDMS layers is important as to ensure the device could be formed properly. A comparison of several PDMS bonding methods was shown in Figure 2.5.

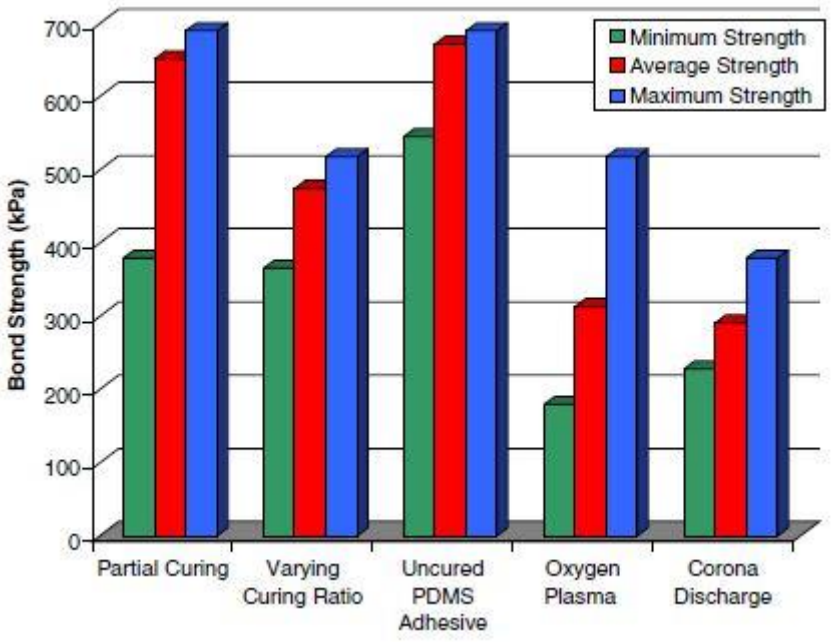

Figure 2.5 Comparison of bond strength of several PDMS bonding methods [145].

Partial curing uses interfacial energy between PDMS and substrate (glass, silicon or PDMS itself) to bond them together. It is the easiest method, which mainly involves thermal lamination of both PDMS layers and does not cause structural damage towards the design. Two PDMS layers are generally employed for this method, which consisted of one PDMS layer with design and one blank PDMS layer. As such, the

bonding method is straightforward and mainly only requiring fresh PDMS layer [144, 145].

Mechanical bonding described uses polymethyl methacrylate (PMMA) to hold PDMS layers together, forming a completed PDMS microfluidic device. The PMMA bonding technique holds the PDMS layers by applying pressure from top and bottom to ensure uniform pressure applied on PDMS layers. Disassembly and reassembly can be done in 10 – 15 minutes but will have limited options in insertions from the side [146, 147].

Apart from partial curing and mechanical bonding method, chemical bonding method can also be used to ensure stronger bonding between PDMS layers. Common chemical bonding method utilizes piranha solution. It is a mixture of strong acids, which is basically a strong and corrosive oxidizing agent to modify PDMS molecular structure so that the cured PDMS could be bonded. However, use of such solution could easily result in deformed channels[148].

Another chemical bonding is by using tetra-n-butylammonium fluoride (TBAF). It is a common solvent used to dissolve cured PDMS, used to bond PDMS layers for HAN microcombustor [14]. In this study, TBAF bonding was able to sustain higher flowrate (up to 20 ml/min) in 'flow-to-burst' test than piranha solution bonding (50 µl/min). However, deformation due to long drenching time (> 10 seconds) might lead to cracking, causing disturbance to fluid flow inside the microchannel.

2.3.4 HAN-based MEMS combustion and propulsion

Various initiatives have been undertaken by different groups of researchers towards the fields of micropropulsion and microcombustion. Each approach has its own unique benefits including utilizing various propulsion technology [149]. The concept of MEMS-based chemical monopropellant micropropulsion system was first proposed in 1997 [120]. Its advantages over conventional liquid bipropellants are greater total impulse, simpler fabrication and easier handling of propellant.

Efforts of several research groups in HAN-based MEMS were compiled in Table 2.10. Ignition and decomposition utilizing catalytic and electrical methods are commonly being used by researchers [12, 94, 112, 113, 117, 150].

In short, electrolytic and catalytic decomposition of HAN-based monopropellant were demonstrated successfully. However, high-temperature materials remain a great concern for catalytic decomposition as efficient decomposition require catalyst or combustor that are able to sustain temperatures higher than 2200 °*C* [16]. Low-temperature co-fired ceramic tape (LTCC), having a low thermal conductivity, is able to resolve the problem of high heat loss in microchannels. Ability of high-temperature co-fired ceramics (HTCC), such as zirconium dioxide (zirconia), are able to withstand extreme environments, resulting it to be proposed as structural material for microthrusters [151]. In addition, rapid electrolytic ignition of XM46 may leads chamber walls to be under

thermal stress and cause it to burst during combustion although 100 to 200 *mN* thrust could be obtained [152].

Table 2.10 Summary of comparison of HAN-based MEMS combustion and propulsion development.

	[152]	[112, 113]	[12, 16, 153, 154]
Ignition method	Electrolytic decomposition	Electrical ignition	Catalytic ignition
Focus	Integration of ignition and combustion system for liquid propellant micropropulsion	Study electrical ignition characteristics of HAN-based liquid propellant	Develop reactor for decomposition of HAN-based propellant
System	Low temperature co-fired ceramic tape	Teflon ignition table	Laboratory flow reactor and thruster
Fuel type	LP 1846	LP 1846	HAN-based monopropellant
Results summary	▪ 200 *mN* thrust ▪ 45 *V* input voltage ▪ 1.9 *J* energy input ▪ 224.5 *ms* ignition delay	▪ Periodic expansion and contraction process when LP1846 droplet is electrified ▪ Increase in peak load voltage, decrease ignition delay ▪ Simplified model of electrical ignition delay of LP1846 droplet established ▪ Ignited by 50 *W* AC ▪ Burning delay time 1 *ms*	▪ Ignition at lower temperature resulted in longer ignition delay ▪ Operable with pulse mode and able to be restarted ▪ HAN/glycine test firing is clean ▪ 8000 *s* operation demonstrated ▪ High temperature materials required for catalyst ▪ Stoichiometric and oxidizer-rich methanol blends give best results

2.4 Summary

In summary, a detailed study towards microreactor system is required as the outcome has huge potential applications in the field of aerospace. Coupled with microfluidic technology, the microreactor device was fabricated using low cost rapid prototyping microfabrication technique. In addition, this fabrication technique utilized polymeric material, i.e. poly (dimethyl) siloxane (PDMS), as structural material for microreactor device in the ease of observation of decomposition of HAN-based solution, due to transparency of the material.

Besides, hydroxylammonium nitrate (HAN) was selected in this project, after comparison with other available options from aspects such as, production technique, ease of production, production cost, handling and transport properties, safety issue and decomposition performance. Research on HAN-based microscale reaction was rather limited in spite of its potential applications in the energy field. Moreover, the microscale application is complicated as the combustion behavior of different HAN ternary system remained to be studied, without any further literature data, under such extreme small volume and reaction interval.

One of the main objectives in this work is to study the overall electrolytic decomposition of various HAN ternary mixtures, visualize the decomposition phenomena and determine parameters that are crucial in the process. Calorimetry study was performed on electrolytic decomposition of HAN to determine suitable fuel component to be added into binary HAN.

Xurography was chosen as ease in fabrication, low startup cost and short turnaround time. Chemical bonding using TBAF was employed in this study due to stronger bonding than normal piranha solution. This method reinforced chamber side bonding towards blank PDMS, ensuring stronger adherence of PDMS between electrodes, and to prevent inner leakage.

Using xurography technique and TBAF bonding method, visualization of HAN decomposition inside PDMS microreactor was carried out. The HAN reaction rate was determined by using the visualization technique.

Therefore, bridging the knowledge gap in this area is important for microreactor system in applications, especially in micro- and nanosatellite, where development in miniaturization will hold the key to future due to its simplistic design and operation and its mobility.

Chapter 3 Macroscale decomposition of HAN ternary mixture

3.1 Objectives

In this chapter, characteristics of HAN ternary mixtures were investigated, with aim to understand their energetic behavior via electrolytic decomposition.

Parameters important to electrolytic decomposition such as electrical conductance was found in existing literatures for binary HAN solution [155, 156], LP 1845 and LP 1846 [157] but not yet fully developed for other type of fuel components. Therefore, this chapter is important in providing a guide in selection of suitable fuel components for HAN ternary mixture for specific applications. Besides, it is also aimed at establishing the roles of electrical conductivity of HAN ternary mixture, which was not found in existing literatures.

This chapter is divided into two main parts, in which the first part is a brief description of synthesis of HAN solution, followed by macroscale electrolytic decomposition of HAN ternary mixture.

Section 3.2 elaborated on preparation of zero OB HAN-based ternary mixture. It started with synthesis of pristine HAN solution under temperature-controlled conditions, utilizing titration between hydroxylamine solution and diluted nitric acid solution (35 *wt%*). The

pristine solution obtained was concentrated in a rotary evaporator to achieve HAN solutions of final target concentration, i.e. 73 *wt%*.

It is followed by a macroscale electrolytic decomposition of HAN ternary mixture via direct current (DC) power. Based on literature review, most of the current HAN ternary mixtures consisted of either triethylammonium nitrate (TEAN) or alcohols, such as methanol and ethanol [16, 83, 113, 154, 158, 159]. However, other component, such as common saccharides, have not been considered as fuel for HAN ternary mixtures. They are commercially available and were also employed as fuel options for other propellant mixtures [160]. This current work could fill up such gap by subjecting HAN ternary mixtures under electrolytic decomposition to evaluate their performance.

Temperature profile of each mixture was evaluated and discussed, to show the influence of chemical interaction between HAN oxidizer and other fuel component towards maximum temperature reached (T_{max}). The effect of electrical resistivity towards the rate of temperature elevation ($\dot{T}$) during electrolytic decomposition was then presented. The former indicates the degree of completion of reaction and the latter indicates the rate of reaction during decomposition.

3.2 Experimental setup

3.2.1 Synthesis of aqueous HAN solution

The HAN solution was synthesized in house by titration of nitric acid (35 *wt%*) and hydroxylamine solution (50 *wt%*) (Fisher Scientific, Malaysia). Chemical reaction of the titration, as shown in Reaction 3-1 (R3-1), is an exothermic reaction. The synthesis setup was adapted from Courthéoux *et al.* [30]. R3-1 has to be performed under 4 °*C* in order to prevent self-decomposition of HAN solution, thus it was kept in an ice bath during titration process. Nitric acid is a strong acid while hydroxylamine is a weak base. To avoid self-decomposition of HAN solution at elevated temperature, the nitric acid was diluted to 35 % prior to titration.

Photograph and schematic diagram of the synthesis of aqueous HAN solution are shown in Figure 3.1. It was carried out under normal laboratory condition. Ice water bath was used to keep the temperature below 4 °*C*. The solution was stirred vigorously during the titration to achieve a homogeneous reaction. The titration product is a HAN solution of low concentration at approximately 20 *wt%*, obtained at equivalence point of pH 2.5. It was further concentrated to 73 *wt%* using vacuum evaporator (Heidolph Instruments, Laborota 4003, Germany). The concentration of aqueous HAN solution was measured using an improved density-driven correlation [14].

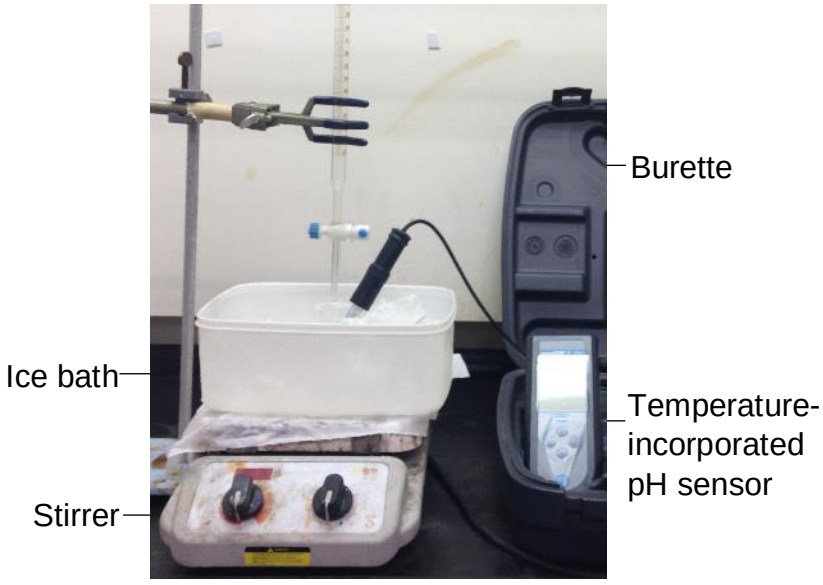

(A)

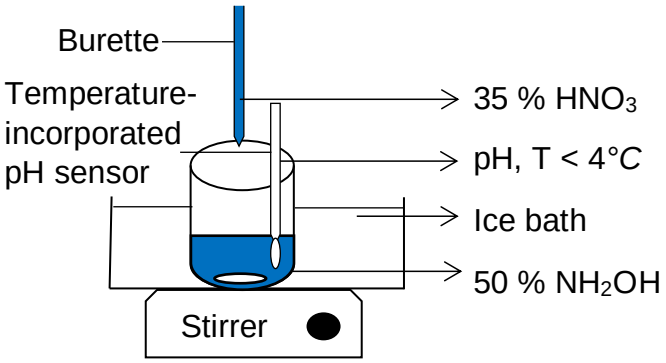

(A)

Figure 3.1 (A) Photograph and (B) schematic diagram of HAN production through titration.

However, if titration was to be performed above 4 °*C*, R3-2 to R3-4 will occur as hydroxylamine is decomposed to ammonia under standard room temperature and pressure. As a result, ammonium nitrate (NH_4NO_3) will be produced as a contaminant, inhibiting the production of HAN and lowering the yield. Thus, addition of acid should be slow, with rapid stirring and under low temperature.

T < 4 ℃	$NH_2OH + HNO_3 \rightarrow [NH_3OH]^+[NO_3]^-$	R3-1
	$NH_2OH \rightarrow NH_3$	R3-2
T > 4 ℃	$NH_3 + H_2O \rightarrow [NH_4]^+[OH]^-$	R3-3
	$[NH_4]^+[OH]^- + HNO_3 \rightarrow [NH_4]^+[NO_3]^- + H_2O$	R3-4

Subsequent purification was carried out in a rotary evaporator to achieve desired concentrations. Rotary evaporator settings are shown in R3-2 below.

Table 3.1 Rotary evaporator setting used in HAN solution purification process.

Water bath temperature (°*C*)	45
Vacuum pump pressure (*mbar*)	30
Rotation speed (*rpm*)	60

The parameters above were set such that the water bath does not exceed 45 °*C*, where the decomposition did not occur on HAN solution during purification and water could be removed more effectively under vacuum condition [161]. Concentration of HAN solution was measured using Equation 3-1 (E3-1), which was adapted from [14]. E3-1 was improved from a density-driven correlation from Courthéoux [30], , as shown in E3-2. 5 *ml* of HAN solution was pipetted (Thermofisher, Finnpipette F2, USA) and its weight was recorded (Mettler Toledo,

AB204-S, Switzerland). E3-1 was chosen instead of E3-2, due to the high similarity of working environment between *Koh's* [14] and current study.

$$\rho = \frac{103.9}{100.5 - w(HAN)x42.9} \quad \text{E3-1}$$

$$\rho = \frac{107.85}{96.045 - w(HAN)x30.99} \quad \text{E3-2}$$

ρ is density of HAN solution, while *w(HAN)* is the mass fraction of HAN. Mass percentage of HAN in water is determined from E3-1.

3.2.2 Characterization of HAN solution

As an established method which were performed by several researches to evaluate concentration of HAN solution [30, 64], thermoanalytical analysis was used to characterize the concentration of HAN solution used in this study. Thermoanalytical analysis was commonly used to study the energy change and mass loss of solid or liquid sample with respect to temperature under a rising temperature controlled environment.

DTA was used in *Amrousse* [64] and *Courthéoux* [30, 80] studies. In this project, weight percentage of HAN in the binary solution was determined by using TGA and DSC because DSC could reflect the energy changes in the HAN sample. When a sample was subjected to heating together with a reference under a controlled environment, the main difference between DSC and DTA is that DSC measures the difference in the amount of heat required to increase temperature of

sample and reference while DTA records the temperature difference between sample and reference upon heating.

73 *wt%* HAN solution was used in this study due to safety purpose [14]. It was pipetted into an aluminum crucible and covered with an aluminum lid, to prevent spillage of the HAN propellant [30, 101]. A hole was made on the lid with a sharp needle, so that the resulting gas can escape and reduce the pressure difference in the crucible. The mass and temperature variation were recorded against time, with a heating rate of 10 *°C* under constant nitrogen flow (50 *ml/min*). Experiment was repeated at least 3 times for repeatability purpose, with raw data tabulated in Appendix I.

In this study, the corresponding normalized weight with the intersection between the endothermic and exothermic peak obtained in the DSC curve is the HAN concentration [80]. An example of TGA and DSC results obtained were plotted in Figure 3.2, showing clearly how concentration of HAN solution could be obtained. The black solid curve corresponds to normalized weight while the blue dotted curve corresponds to heat flow curve. As indicated by the heat flow curve, a decreasing slope indicates that heat is absorbed by sample while an increasing slope shows that heat is released by sample. As the temperature was ramped up from room temperature, the normalized weight curve remained unchanged while the heat flow curve decreased steadily. It showed HAN solution was absorbing heat but did not boil as there is no obvious change in its mass. The less steep slope of heat flow

curve before boiling point of water can be interpreted as slow evaporation of water before temperature of the sample attained boiling point of water. Upon reaching boiling point of water, the heat flow curve decreased with a steeper slope.

The endothermic peak of 73 *wt%* HAN solution was found to be 158 *°C*, which is comparable to the results obtained by Amrousse *et al.* (167 *°C* for 80 % HAN solution) [64]. The decomposition temperature of 73 *wt%* HAN solution was found to be 181 *°C*, which is higher than the decomposition temperature of 160 and 173 *°C* for 60 and 79 *wt*% HAN solution obtained by *Courthéoux et al.*, respectively [30, 80]. The sample also produced two exothermic peaks (181 and 223 *°C*), showing that the thermal decomposition of HAN is two step, which is also suggested by thermal decomposition of a 95 *wt%* HAN solution [64]. After the exothermic peak, abrupt decrease of the HAN solution sample weight to zero, indicating the HAN sample was fully decomposed into gas species.

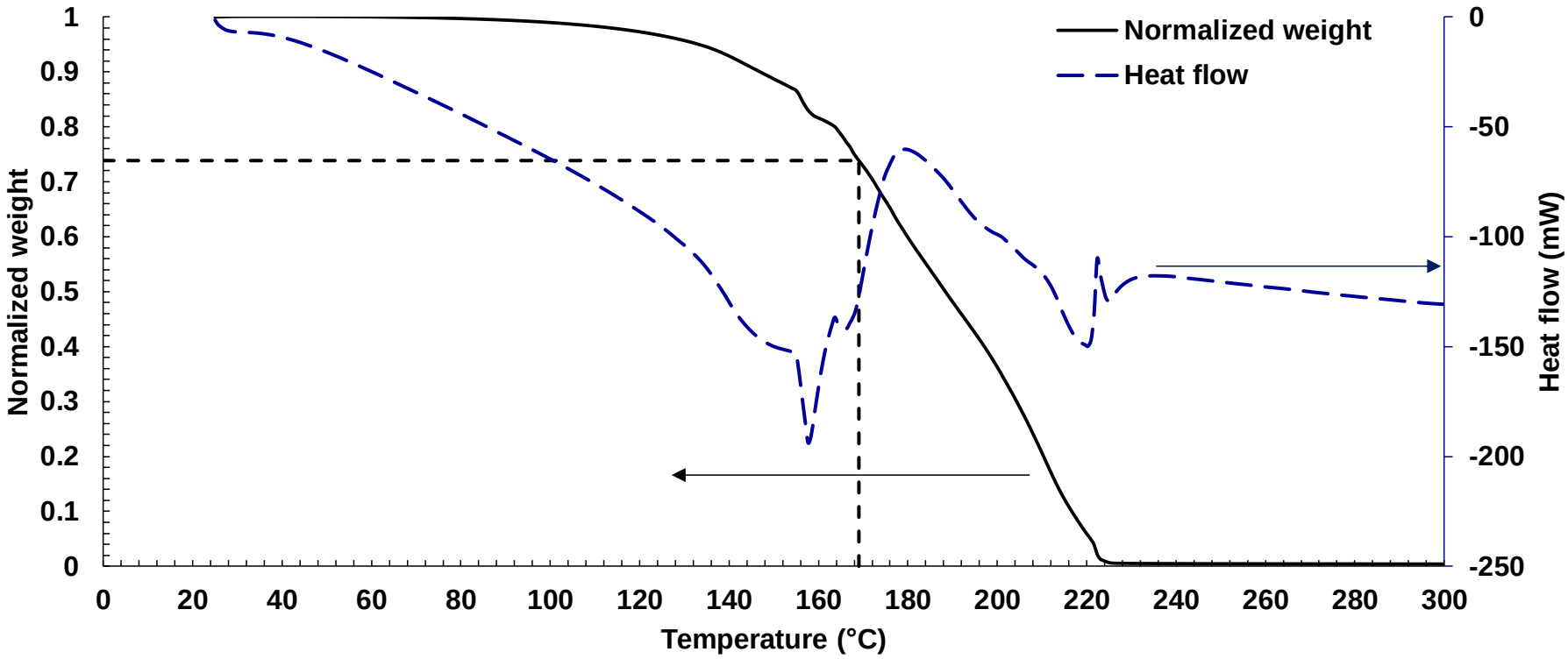

Figure 3.2 TGA and DSC results of thermal decomposition of 73 *wt%* HAN solution. The intersection between the endothermic and exothermic peak of DSC curve to normalized weight is 0.74, indicating the concentration of HAN solution is 74 *wt%*.

3.2.3 Preparation of zero OB HAN-based ternary mixtures

Oxygen balance (*OB%* represented by %), is defined as the amount of oxygen remained after oxidation of hydrogen, carbon and metals to produce H_2O, CO_2 etc. [162]. The *OB%* of a chemical component can be calculated using E3-3.

$$OB\% = \frac{-1600}{MW} x(2X + \left(\frac{Y}{2}\right) - Z) \qquad \text{E3-3}$$

where X, Y and Z represent the number of atoms for carbon, hydrogen and oxygen, respectively, *MW* is the molecular weight of component in *g/mol*.

A zero oxygen balance mixture is the ideal chemical propellant as it releases the maximum amount of thermal energy in combustion. In the HAN-based ternary mixtures, the HAN solution (a binary mixture) serves as an oxidizer while the chemical compound (third component) serves as a fuel. Water being employed as a solvent, has a stabilizing effect towards decomposition of HAN [64, 85]. In this study, chemical compounds which are soluble in water with high negative *OB%*, e.g. alcohols, saccharides, nitrogen-rich compounds, etc. were selected as fuel components. Generally, oxidizers have positive *OB%*. Based on E3-3, the amount of chemical compound required to achieve a zero OB ternary mixture was determined and summarized in Table 3.2. It was then added into the 5 *g* of HAN solution and mixed thoroughly by mechanical stirring.

Table 3.2 Selected chemical compounds and the amount required to achieve zero OB%.

Category of fuel	Component	Chemical formula	OB% (%)	Amount added (g)
	HAN[a]	NH_3OHNO_3	33.30	-
Alcohol	Methanol	CH_3OH	-149.83	0.81
	Ethanol	CH_3CH_2OH	-195.31	0.62
	Propanol	$(CH_3)_2CHOH$	-239.64	0.51
Saccharides	Sucrose	$C_{12}H_{22}O_{11}$	-112.20	1.08
	Dextrose	$C_6H_{12}O_6$	-96.90	1.26
Nitrogen-rich compounds	Urea	$CO(NH_2)_2$	-79.93	1.52
	Ammonia[b]	NH_3	-68.49	5.07

[a]73 *wt%* aqueous HAN solution

[b]35 % ammonium hydroxide solution

3.3 Electrolytic decomposition of HAN ternary mixture and temperature measurement

3.3.1 Electrolytic decomposition and temperature measurement setup

In this section, macroscale electrolytic decomposition was conducted to provide a further understanding towards the complex decomposition behavior of HAN ternary mixtures. In addition, it is

important to conduct a preliminary screening on selection of fuel component in determining the best formula of HAN ternary mixture for micropropulsion purpose. This section enables us to explore the effect of each fuel component on HAN ternary mixtures with their respective chemical interactions. Zero oxygen balance formulation of propellant was favored and shown to be more energetic than oxidizer alone or mixture of positive oxygen balance [163]. Common liquid propellant LP1845 (63.2% HAN, 20% TEAN and 16.8% H_2O) and LP1846 (60.8% HAN, 19.2% TEAN and 20% H_2O) also have zero oxygen balance. Calculations of the oxygen balance and the formulations will be shown in Appendix I.

Photograph and schematic of experimental setup of the electrolytic decomposition are illustrated in Figure 3.3. The zero OB HAN ternary mixture which consists of 5 *g* of aqueous HAN solution and its respective fuel component, as stated in Table 3.2, was filled into a beaker and covered with a custom-made polymer lid. It is to minimize heat loss to the surroundings. A pair of commercial-grade copper wire (Element14, BS 6362, Malaysia) was used as electrodes. Copper was selected as the electrode material due to its high cost effectiveness (USD 2.634/pound), compared to platinum (USD 16096/pound) [164]. The copper ion reactions competing for electrons at the electrodes speed up the reactions. Fresh copper electrodes were used to ensure the consistency of the results.

Electrolytic decomposition of the mixture sample was initiated through a DC power supply unit (Elektro-Automatik, PS 8080-120 2U, Germany), in which voltage was set at 60 *V* of constant voltage mode. The current was capped at 5 *A*. The change in temperature of the ternary mixtures was measured using a commercially available K-type thermocouple (RS Components, RS Pro 3342622, UK) connected to a data logger (Cole Parmer, 37953-20, US). The measurement was taken at 1 *Hz*. Since existing study is to investigate the energy released during the decomposition, the temperature measurement was stopped when the HAN ternary mixture was consumed completely. Simultaneously, the event of electrolytic decomposition of the ternary mixture was recorded using a camcorder. Each experiment was repeated at least 3 times for repeatability purpose.

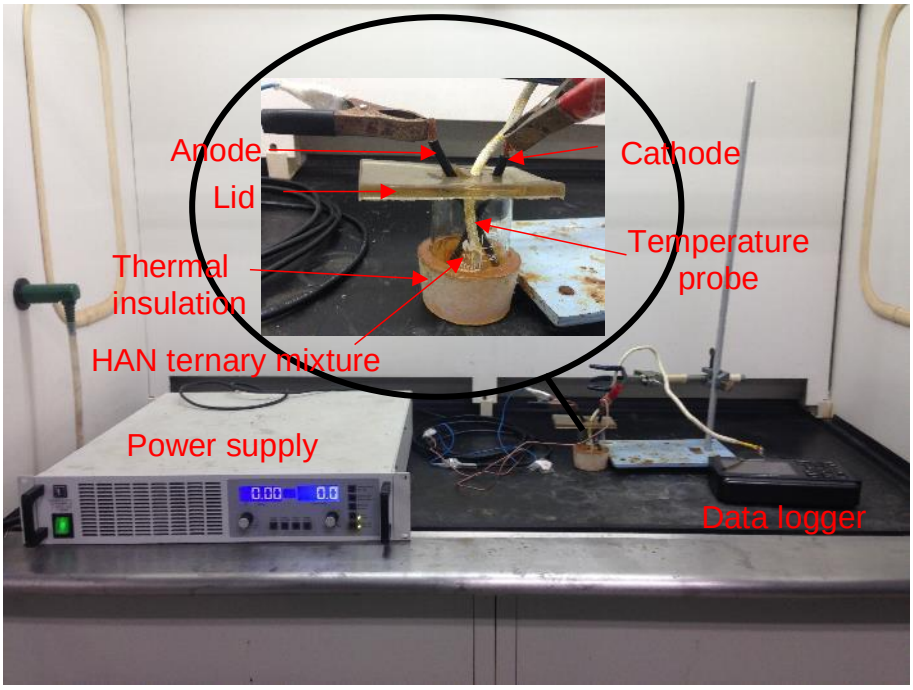

(A)

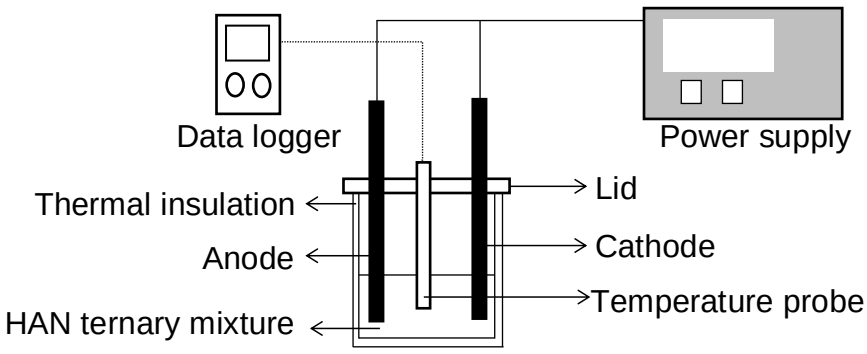

(B)

Figure 3.3 (A) Photograph and (B) schematic of experimental setup for electrolytic decomposition of HAN-based mixture decomposition in a thermally insulated beaker.

Utilizing HAN-propanol-water mixture as an example, the overall electrolytic decomposition temperature profile is depicted in Figure 3.4. Temperature of the mixture remained constant at room temperature, T_0,

for approximately 2 seconds after the power supply was switched on. This implies a delay, t_i, in the electrolytic decomposition, which is due to the induction time for the electrolysis to occur [117], and the finding coincided well with previous studies [111].

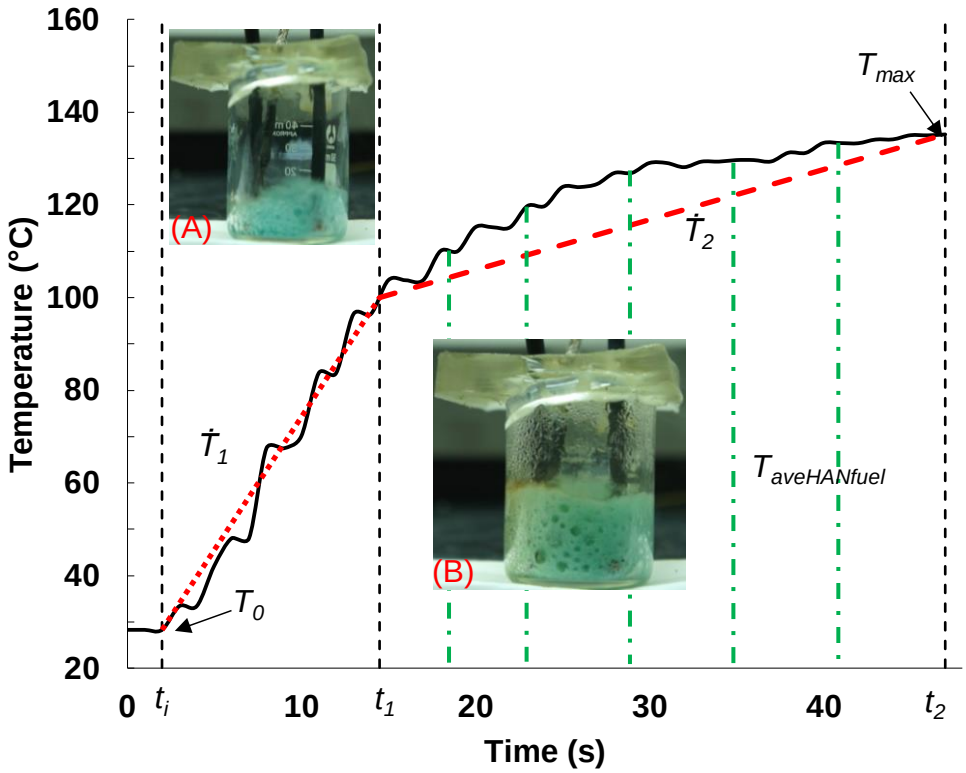

Figure 3.4 Temperature profile for decomposition of HAN-Propanol ternary mixture. Photograph of HAN-Propanol in (A) first stage and (B) second stage, during electrolytic decomposition. Note that the thermal insulation was removed in the inset photographs for the better clarity in demonstration.

Once the decomposition of HAN ternary mixture was initiated, a rapid rise in temperature was observed. The rate of temperature elevation decreases after reaching 100 °*C*, corresponding to the boiling of water in the HAN solution. Previous study shows that the initial stage

of electrolytic decomposition of HAN mixture is dominated by electrolysis of water at low temperature [165].

As the initial HAN-propanol mixture contain large amount of ions in aqueous form, its electrolysis yields a higher reaction rate at the beginning of decomposition. After water has evaporated, the effect of electrochemical reactions diminished and the performance of mixture is dependent on its thermal decomposition thereafter.

Subsequently, the decomposition of concentrated HAN is promoted by protons produced from the electrolysis of water [110]. More energy from decomposition of HAN is released to enhance the decomposition of the remaining mixture. As such, the temperature profile for electrolytic decomposition of HAN ternary mixture can generally be divided into two distinctive stages. The slopes of these two stages, $\dot{T}_1$ and $\dot{T}_2$, are illustrated as dotted and dashed line respectively, in Figure 3.4. They represent the rate at which the HAN ternary mixture is electrolytically decomposed and are evaluated as

$$\dot{T}_1 = \frac{100\ ℃ - T_0}{t_1 - t_i} \qquad \text{E3-4}$$

$$\dot{T}_2 = \frac{T_{max} - 100\ ℃}{t_f - t_1} \qquad \text{E3-5}$$

$$t_{total} = t_f - t_i \qquad \text{E3-6}$$

where T_0 is the mixture initial temperature before the decomposition began, T_{max} is the maximum attainable temperature for the electrolytic decomposition of HAN ternary mixture, t_i, t_1 and t_f are the time taken for the ternary mixture to reach initial mixture temperature, 100 °*C* (1st stage)

and T_{max} (2nd stage), respectively, t_{total} is the time taken for the electrolytic decomposition to complete.

Both temperature results (T_{max} and $\dot{T}$) are utilized as performance indications of electrolytic decomposition of HAN ternary solution. The former is peak temperature reached during the entire electrolytic decomposition, indicating the degree of completion of reaction. The latter is the indication of rate of reaction during decomposition, where $\dot{T}_1$ *and* $\dot{T}_2$ are the indication of rate of reactions at first and second stage, respectively.

In secondary analysis, evaluation was carried out on the area under the curve. Average temperature across the time of interest could be obtained by dividing the area under the curve over the time of interest. Higher average temperature reflects higher efficiency of the decomposition and vice versa.

The region of interest is of the decomposition of HAN and fuel, where the water inside the mixture has evaporated, which refers as second stage in this study. The region was bounded by the temperature curve, t_1 line and t_2 line, where the mixture hits 100 °C and T_{max}, respectively. The region was represented by the green dash-dotted area in Figure 3.4 and was denoted as $T_{aveHANfuel}$.

The inset photographs in Figure 3.4 depict the gaseous species evolvement during electrolytic decomposition of HAN-propanol ternary mixture. The HAN ternary mixture was colorless before electrolytic decomposition was initiated. Upon electrolytic decomposition, the copper

anode was consumed and copper ions (Cu^{2+}) ions were released, causing the mixture to turn blue, as shown in Figure 3.4 inset (a).

A thin layer of brown gas (NO_x) was observed in the later stage of thermal decomposition in Figure 3.4, as shown in inset (b) [110]. The phase change from liquid to gas in the HAN ternary mixture during the electrolytic decomposition was confirmed by visual inspection. The formation and bursting of bubbles has interrupted the heat transfer which is typically constant in single phase fluid.

At boiling point of water, the presence of air bubbles causes frequent and random circuit breakdown that degrades the efficiency of electrolytic decomposition. As heat is continuously released from decomposition, the mixture is effectively undergoing thermal decomposition and electrolytic decomposition simultaneously. Appearance of NO was measurable at temperature higher than 200 °*C* after decline of NO_2 [166]. The T_{max} of the decomposition of HAN-propanol was lower than 140 °*C* and the presence of brown color gas, confirmed the presence of NO_2 in Figure 3.4.

In the previous study, the slope breakpoint in temperature elevation of solution occurred at boiling point of water, when using copper electrodes to decompose HAN solution at standard room condition [115]. Similar trend was also noticed in ternary mixtures.

Electrolysis of water and HAN take place simultaneously when current is supplied through the copper electrodes, as shown in R3-5 and R3-6, respectively. The former reaction is endothermic and preferred due

to relatively low standard potential (1.23 *V*). The latter is a highly exothermic reaction and is promoted from the protons produced from the electrolysis of water [110], where the heat released enhances decomposition of the remaining mixture itself. Thus, it can be summarized that electrolytic decomposition of HAN solution is a combination of evaporation, electrochemical and chemical process.

The reactions occurred at anode and cathode are stated as below:

At anode:

$$H_2O(l) \rightarrow 2H^+(aq) + \frac{1}{2}O_2(g) + 2e^- \quad \text{R3-5}$$

$$HAN(aq) + H^+(aq) \rightarrow NH_3OH^+(aq) + HNO_3(g) \quad \text{R3-6}$$

$$Cu(s) \rightarrow Cu^{2+}(aq) + 2e^- \quad \text{R3-7}$$

At cathode:

$$2NH_3OH^+(aq) + 2e^- \rightarrow 2NH_2OH(g) + H_2(g) \quad \text{R3-8}$$

$$Cu^{2+}(aq) + 2e^- \rightarrow Cu(s) \quad \text{R3-9}$$

Overall reaction:

$$2HAN(aq) + H_2O(l) \rightarrow 2HNO_3(g) + 2NH_2OH(g) + H_2(g) + \frac{1}{2}O_2(g) \quad \text{R3-10}$$

The overall electrolytic decomposition of HAN, is a result of multiple reactions occurring at both anode and cathode, as indicated by R3-5 to R3-9, summarized in R3-10 [110]. During the initiation stage, at

the anode, the first bubble (O_2) is formed due to the electrolysis of water as represented by [110]. The production of protons (H^+) promotes the subsequent decomposition of HAN solution which is a highly exothermic reaction as shown in R3-6.

The role of copper electrode is shown in R3-7 [115], in which the copper anode was consumed and releases additional electrons to facilitate the cathode reaction in R3-8. It was shown in R3-9 that the copper ions will recombine with electrons to form solid copper at anode. As shown in the overall reaction, the number of moles of gaseous components produced at the cathode side, including hydroxylamine (NH_2OH) and hydrogen (H_2), is 20 % more than the amount of produced at the anode side, O_2 and nitric acid (HNO_3). Thus, the cathode side reaction is more dominant.

Electrolysis decomposition of HAN could be accurately modelled by involving thermal decomposition, with evaporation of water is dominant in the process [54, 110]. The entire electrolytic decomposition of HAN was initially initiated by a chain of complex electrochemical reactions and underwent a series of thermal decomposition reactions [110, 111].

3.3.2 Effect of electrical resistivity on electrolytic decomposition

Electrical resistivity indirectly reflects the rate of electron transfer in a particular solution, which is a key process in electrolytic

decomposition of HAN ternary mixtures. The measured electrical resistivity for different HAN ternary mixtures is listed in Table 3.3. As the table was arranged in the order of increasing mixture resistivity, existing study reveals that the mixture resistivity has no significant effect on the maximum temperature obtained from the electrolytic decomposition of HAN ternary mixture. Instead, the maximum temperature obtained is influenced by the type of fuel component added as explained in the next section (Section 3.3.3).

As the decomposition of HAN-based ternary mixtures is initiated via electrolysis, the electrical properties of the mixtures play an important role in the decomposition. The electrical conductivity of the prepared ternary mixtures were measured using a conductivity meter (Eutech, CON 2700, Singapore). The electrical resistivity, ρ_M, of the mixture is then taken as the reciprocal of the electrical conductivity. Based on the instrument specifications, the accuracy of electrical resistivity measurement is 0.0015 $\mu\Omega.m$. Electrical resistivity of the mixture is inversely proportional to the ease of such mixture conducting electricity, and as such the rate of temperature rise should be affected by the mixture resistivity. Effect of electrical resistivity will be correlated in the results section. All experiments were carried out under standard room conditions, with the results tabulated in Appendix 1.

Table 3.3 Electrical resistivity of different HAN ternary mixtures and the maximum temperature achieved from the electrolytic decomposition.

Fuel component	Resistivity of mixture ($\mu\Omega.m$)	T_{max} (°C)
Ammonia	0.0387	269.13
Methanol	0.0858	165.47
Ethanol	0.0899	259.37
Propanol	0.0913	137.33
Sucrose	0.1361	170.50
Urea	0.1453	233.40
Dextrose	0.1609	159.37

The rate of reaction at the first stage, $\dot{T}_1$, of electrolytic decomposition is closely associated to the electrical properties of the HAN ternary mixtures. $\dot{T}_1$ showed a general linear trend with the electrical resistivity of HAN ternary mixtures, as shown in Figure 3.5.

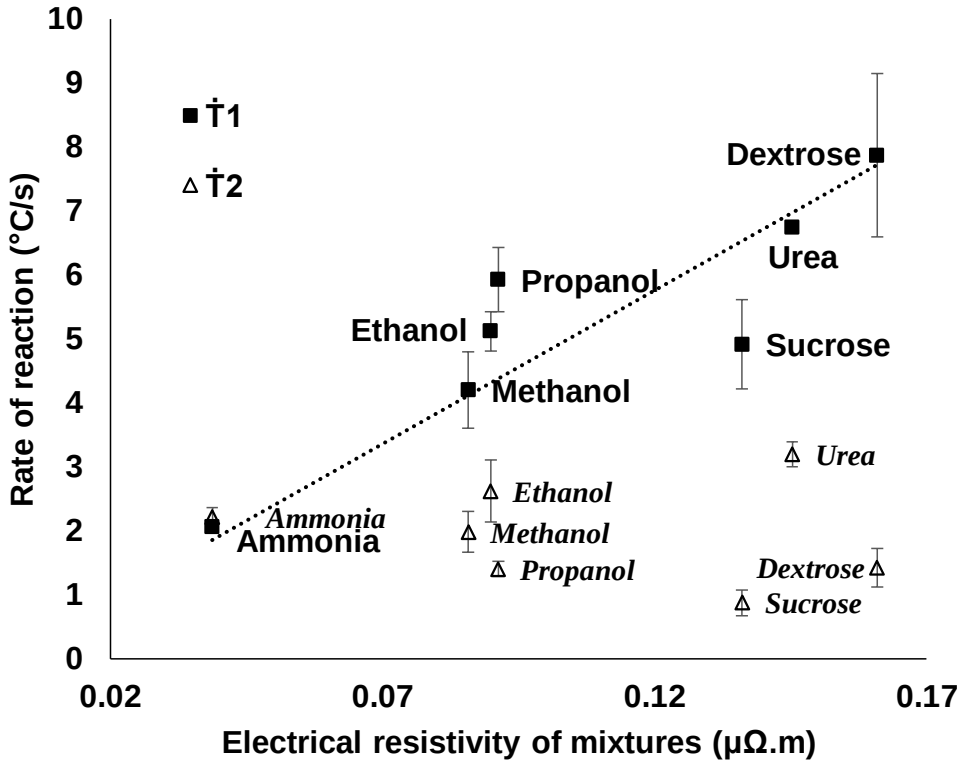

Figure 3.5 The change in rate of reaction in the electrolytic decomposition of HAN ternary mixture with different electrical resistivity.

Joule heat is represented by equation below: [167]

Joule heat, $H = I^2Rt$ E3-7

Joule heating rate, $H/t = I^2R$ E3-8

Resistance, $R = \rho l/A$ E3-9

As the length and area intact between the mixture and electrodes are constant, thus resistance is directly proportional to resistivity in this case.

Resistance, $R \propto \rho$ E3-10

As the current in this study was limited to 5 A and the current is observed to be constant during the start of the electrolysis, as shown in Figure 3.6, E3-8 can be simplified as below:

Joule heating rate, $H/t \propto R$ E3-11

As the reaction rate could be linearly correlated with mixture resistivity, thus Joule heating was shown to present in this case.

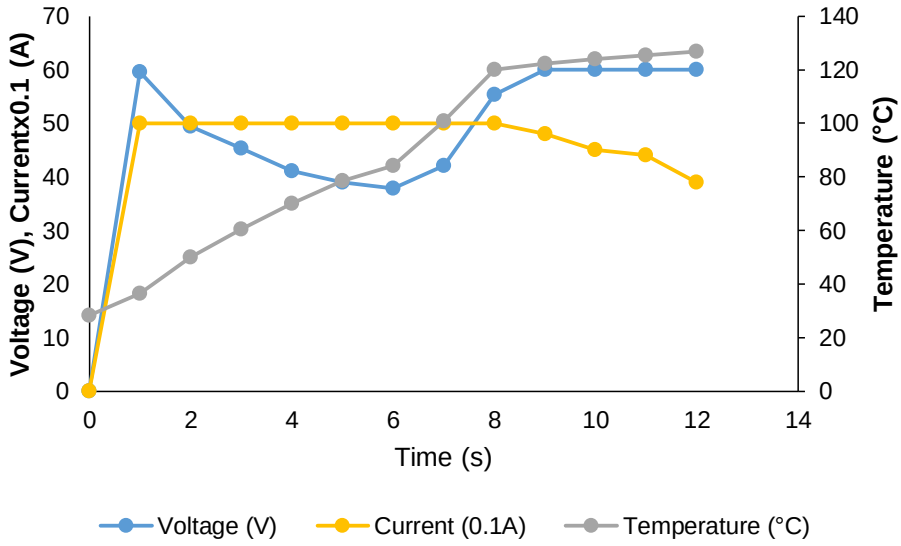

Figure 3.6 Voltage, current and temperature variation of HAN solution subjected to electrolytic decomposition, current remained constant before increment of temperature slowed down. The voltage and current values were extracted from video recording.

Lower rate of decomposition reaction of HAN-methanol ternary mixture was justified by lower boiling point of HAN-methanol ternary mixture. The heating of methanol consumes additional energy and suppresses the reaction rate. Thus, alcohol-based HAN ternary mixtures demonstrated moderate rate of decomposition reaction which agrees

well with the findings from previous study on thermal and catalytic decomposition of HAN mixtures [16, 18]. As such, HAN-methanol (4.21 *°C/s*) demonstrated highest suppression of reaction rate among all HAN ternary mixtures.

On the other hand, the electrical resistivity of the HAN ternary mixture has negligible influence on the rate of reaction at the second stage of electrolytic decomposition. After the HAN ternary mixture attains the boiling point of water, most of the water content were evaporated. The electrolysis of water has ceased taking place and hence the production of electrons too. This explains lower rate of decomposition reaction at the second stage of reaction with the exception for HAN-urea and HAN-ammonia ternary mixtures in which the fuel components continue to produce electrons to sustain the electrolysis reaction. As such, it could be deduced that the second stage of electrolytic decomposition in HAN ternary mixture is driven by chemical reactions between the remaining fuel components and the HAN oxidizer. As more heat is released continuously from decomposition, the mixture is effectively undergoing thermal and electrolytic decompositions simultaneously [111].

3.3.3 Effect of fuel components on electrolytic decomposition

3.3.3.1 General overview

To investigate the effect of different fuel components on the electrolytic decomposition of HAN ternary mixture, similar experiment was carried out under identical conditions using 5 *g* of binary HAN mixture (73 *wt%* HAN solution) for benchmarking purpose. Temperature profiles of electrolytic decomposition of all HAN ternary mixtures tested were plotted in Figure 3.7. Temperature profile of HAN binary solution was also plotted in the figure, serving as a benchmark.

Other than urea and ammonia solution, all the other fuel components being a molecular fuel, undergo thermal decomposition, rather than electro-thermal decomposition. All remaining HAN ternary mixtures have similar trend of temperature increase before boiling point of water, apart from HAN-dextrose and HAN-ammonia, as they can be electrolyzed in the first stage. Also, most of the HAN ternary mixtures have a noticeably lower rate of reaction in the second stage as it approaches T_{max}, as compared to the first stage.

As mentioned previously, HAN-propanol has two stages of decomposition. Other than the number of decomposition stages, different HAN ternary mixtures vary in their performances, either T_{max} or $\dot{T}_1$, mainly due to chemical interactions of fuel component with HAN. Figure 3.7 is broken down for further investigation to be carried out with respect to the fuel category:

1. Alcohols, 2. Saccharides, 3. Nitrogen-rich compounds

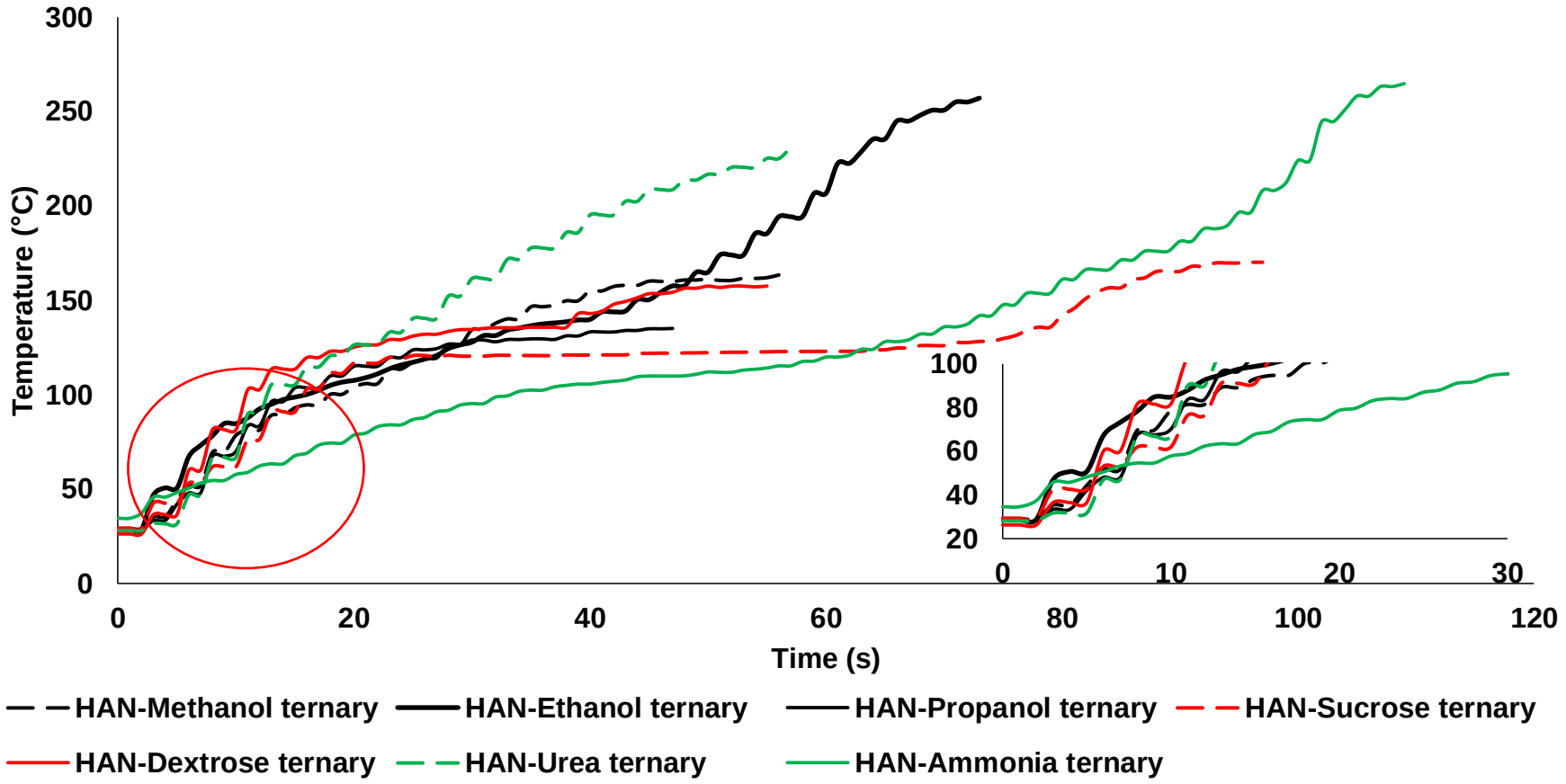

Figure 3.7 Temperature profiles for electrolytic decomposition of all HAN ternary mixtures. Figure inset show decomposition of HAN ternary mixtures before 100 *°C*, as highlighted in red circle region in main figure.

3.3.3.2 Alcohols

The temperature profiles for alcohol-based HAN ternary mixtures were plotted in Figure 3.8 for comparison with HAN binary solution. Delay was also observed in the decomposition of binary HAN solution, as shown in the red circle region in the figure. Electrolytic decomposition of binary HAN solution occurs in one stage, while HAN-alcohol has two stage decomposition as addition of fuel complicated the reactions undergone.

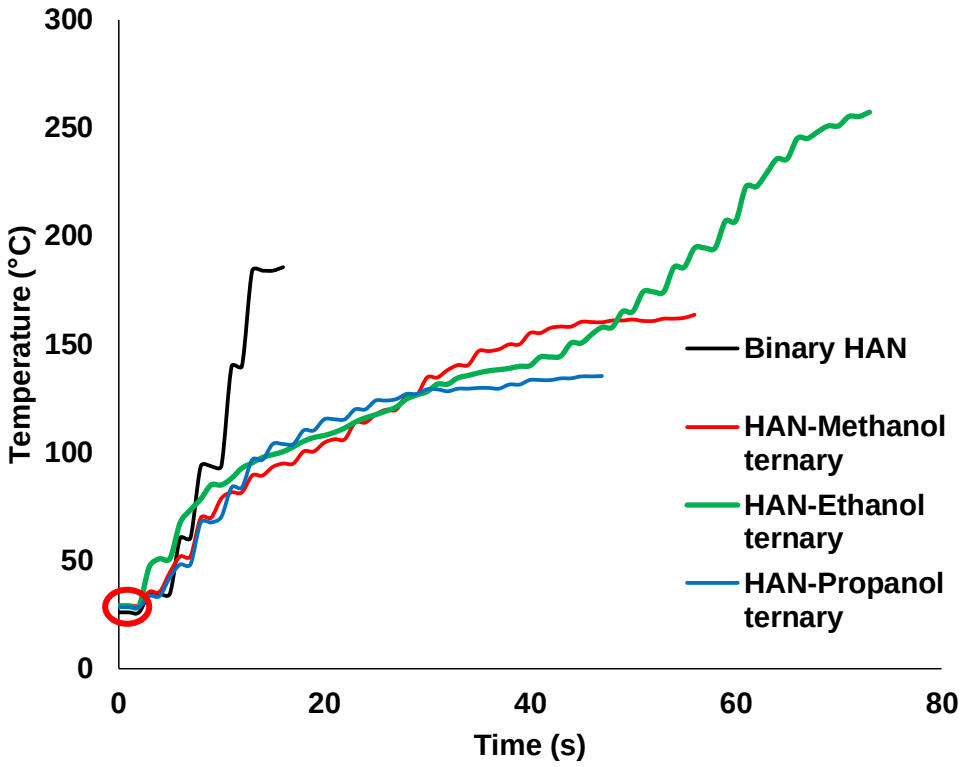

Figure 3.8 Comparison of temperature profile for electrolytic decomposition of binary HAN solution and alcohol-based HAN ternary mixture.

Once the decomposition was initiated, the temperature of binary HAN solution raised steadily to the maximum temperature of approximately 185 °*C* at a mere 16 seconds. The maximum temperature achieved in the electrolytic decomposition is 165.47 ± 16.51 °*C*, 259.37 ± 17.27 °*C*, and 137.33 ± 15.36 °*C* for HAN-methanol, HAN-ethanol and HAN-propanol ternary mixtures, respectively. The energetic behavior of HAN decomposition resulted in high deviations obtained in the results.

T_{max} of HAN-methanol and HAN-propanol are lower than that of the binary HAN solution (185.5 °*C*) but T_{max} of HAN-ethanol is higher than that of binary HAN solution. In thermal analysis of HAN-methanol ternary mixture, HAN started to decompose after methanol and water has totally evaporated [85]. Since electrolysis of water and HAN molecules occurred simultaneously, thus, addition of the fuel component, i.e. methanol, has affected the rate of temperature increase in the first and second stage, as referred in Figure 3.8. This is due to part of the energy released from decomposition of HAN molecules absorbed by the alcohols, therefore the rate of temperature increase of HAN-methanol is lower than that of binary HAN.

As alcohols have high volatility and unable to undergo electrolysis, vaporization of alcohol took place before gas-phase reactions between alcohols and HAN occurred. Once the electrolytic decomposition was initiated, the temperature increase in binary HAN and HAN-alcohol ternary mixtures were similar. However, thermal energy resulted from electrolysis in the first stage was absorbed by the alcohols due to their

high volatility, causing a slower increase in temperature at the first stage. Larger amount of total heat was required to fully vaporize methanol (0.97 *kJ*), followed by ethanol (0.51 *kJ*) and propanol (0.40 *kJ*). It is evidenced by the lower rate of reaction in the first stage for electrolytic decomposition of HAN-methanol ternary mixture in comparison to its counterpart of HAN-propanol ternary mixture.

The total theoretical amount of energy released during combustion of ethanol is highest (-18.45 *kJ*), followed by methanol (-18.08 *kJ*) and propanol (-17.15 *kJ*). Thus, the decomposition of HAN-ethanol ternary mixture achieved higher maximum temperature than HAN-propanol ternary mixture and may have absorbed sufficient activation energy from second stage of reaction and release more energy by entering third stage of reaction. According to Table 3.4, the average temperature during second stage of electrolytic decomposition is as follow: HAN-ethanol (171.99 *℃*), HAN-methanol (136.70 *℃*) and HAN-propanol (122.97 *℃*), indicating that ethanol has released more energy during the interaction with HAN. The calculations of heat of reactions and energy released were shown in Appendix I.

Table 3.4 Average temperature during second stage and time taken for decomposition to complete for HAN-Methanol, HAN-Ethanol and HAN-Propanol ternary mixture.

	HAN-Methanol		HAN-Ethanol		HAN-Propanol	
	Average	**S.D. (%)**	**Average**	**S.D. (%)**	**Average**	**S.D. (%)**
$T_{aveHANfuel}$ (°C)	136.70	9.13	171.99	7.34	122.97	7.95
t_{total} (s)	50.67	13.43	75.33	7.31	38.33	23.67

Nevertheless, the adding of alcohol fuel components has prolonged the time taken to reach the maximum temperature, as shown in Table 3.4. The time taken to reach the maximum temperature was increased from 14 *s* for binary HAN to 38.33 *s*, 50.67 *s* and 75.33 *s*, for HAN-propanol, HAN-methanol and HAN-ethanol, respectively. Longer time was taken to reach the maximum temperature, in this case, has shown that the addition of fuel has altered the rate of energy release, as compared to HAN solution.

3.3.3.3 Saccharides

Saccharides are widely used as fuel component in candy rocket (amateur rocketry) as they are commercially available and relatively safe to handle [160]. The temperature profiles for electrolytic decomposition of HAN-dextrose ternary mixture was plotted in Figure 3.9.

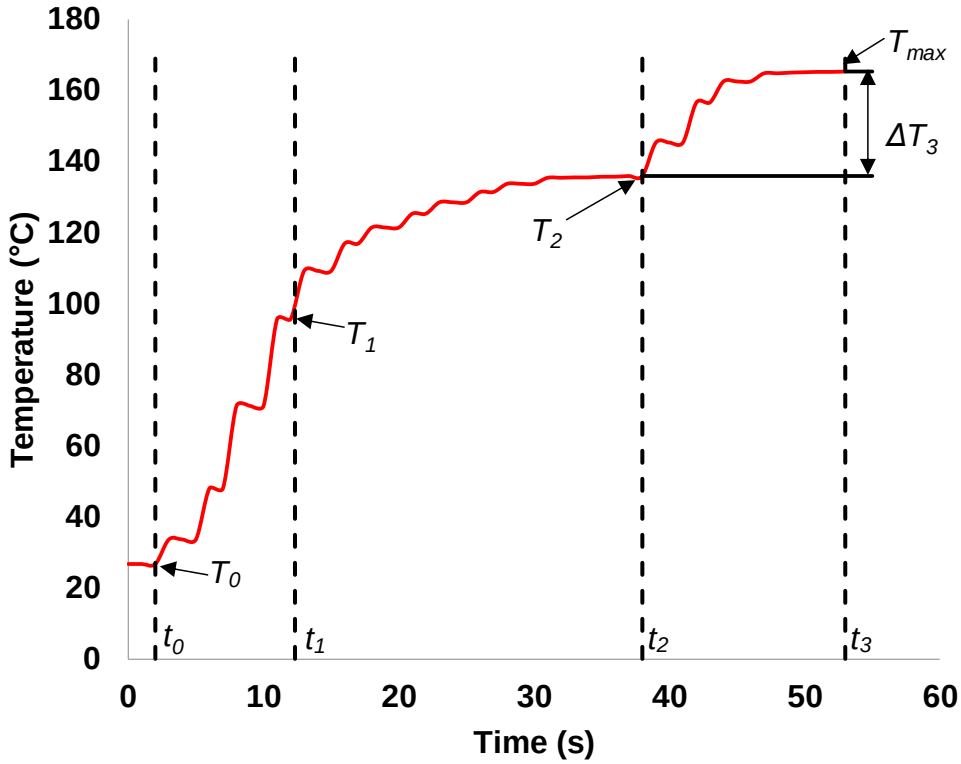

Figure 3.9 Temperature profile for decomposition of HAN-Dextrose ternary mixture.

$$\Delta T_3 = T_{max} - T_2 \qquad \text{E3-12}$$

$$\Delta t_n = t_n - t_{n-1} \qquad \text{E3-13}$$

where T_2 is the temperature before the mixture has a second rise in temperature, ΔT_3 is the temperature difference between T_2 and T_{max} in 3rd stage, Δt_n is the time required for the electrolytic decomposition to complete nth stage.

In general, the electrolytic decomposition reaction of saccharide-based HAN mixture has 3 distinctive stages. The first and second stages are similar to that of alcohol-based HAN ternary mixtures. However, the temperature rise is marginal in the second stage and rise abruptly thereafter to form the third stage of reaction. In the second stage, the

mixture is accumulating thermal energy for the decomposition of saccharide, an exothermic process, to occur.

Chemical structure of dextrose and sucrose are shown in Figure 3.10.

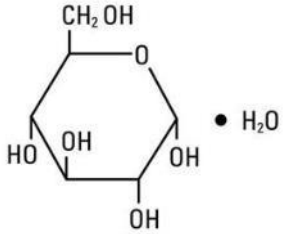	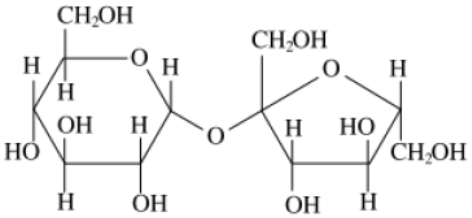
MW = 198.2 *g/mol*	MW = 342.3 *g/mol*
(A)	(B)

Figure 3.10 Chemical structure of (A) dextrose and (B) sucrose.

From Figure 3.10 and Figure 3.11, as the saccharides gain longer in chain, T_{max} increases with the expense of increase in the duration of second stage (Δt_2). Thus, polysaccharides will be able to achieve higher T_{max} but also possess lower $\dot{T}_1$ and require longer Δt_2.

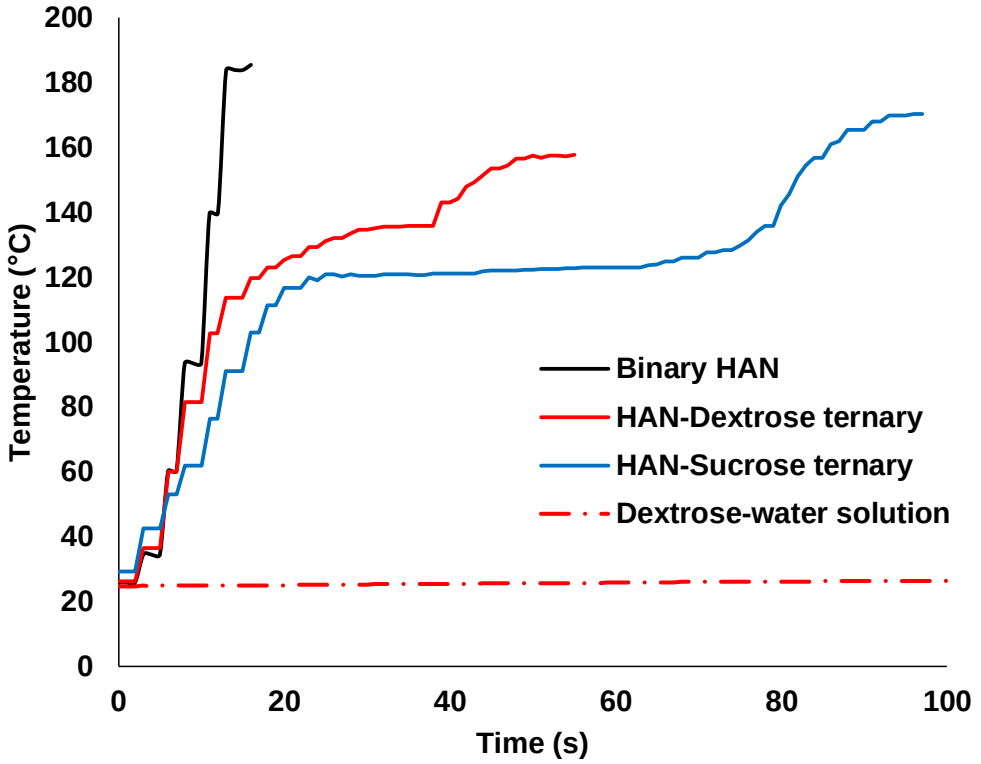

Figure 3.11 Comparison of temperature profile for electrolytic decomposition of binary HAN solution and saccharide-based HAN mixtures.

The temperature profiles for electrolytic decomposition of HAN-dextrose and HAN-sucrose ternary mixtures were plotted in Figure 3.11, in comparison with HAN binary solution and pure dextrose solution. Dextrose and sucrose are termed as reducing and non-reducing sugar, respectively. The term “reducing sugar” shows dextrose’s ability to act as chemical reducing agent while sucrose is more stable when being heated [168], thus HAN-dextrose has a higher reaction rate (7.81 *℃/s*) in the first stage, as compared to HAN-sucrose (4.92 *℃/s*).

Although saccharides are more thermally stable than alcohols, HAN-sucrose and HAN-dextrose have similar rate of temperature

elevation in the first stage as HAN from T_0 to 53 and 80 °C, respectively. This shows that simpler saccharides do not absorb the heat released from decomposition of HAN as fast as more complex saccharides. Negligible changes in temperature throughout the decomposition period of dextrose solution, showing that addition of saccharides do not affect the first stage of decomposition.

Decomposition of sucrose solution was first carried out by hydrolysis reaction, named as inversion reaction [169], shown in R3-11. The rate of reaction is almost 5000 x faster at 90 °C than at 20 °C [168]. The Δt_2 of HAN-sucrose (43 *s*) decomposition is notably longer than that of HAN-dextrose (24 *s*). Dextrose is actually an alternate form of glucose, which is a simpler form of saccharide, whereas sucrose is a more complex form of saccharide. Sucrose required extra time to be broken down, as compared to dextrose, as shown in R3-11, thus requiring more time to complete its breakdown.

$C_{12}H_{22}O_{11}$ *(sucrose)* + H_2O *(water)* → $C_6H_{12}O_6$ *(glucose)* + $C_6H_{12}O_6$ *(fructose)* R3-11

Carbon residue was observed during experiment, decomposition of sucrose first occurred via dehydration to pure carbon and water, as represented in the following reaction [170]:

$C_{12}H_{22}O_{11}$ + *heat* → 12 C + 11 H_2O R3-12

As shown in the reaction above (R3-12), dextrose undergoes similar reaction to produce carbon and water. However, the heat of

reaction resulting from decomposition of dextrose (-16.88 *kJ*) is lower than that of sucrose (-17.03 *kJ*). Calculations for the heat of reaction were shown in Appendix I. This results in lower T_{max} achieved in electrolytic decomposition of HAN-dextrose mixture. The maximum temperatures of HAN-dextrose and HAN-sucrose ternary mixtures are 159.37 ± 5.48 °*C* and 170.5 ± 10.17 °*C*, respectively. Dextrose is less thermally stable and possesses lower melting temperature than sucrose. Therefore, dextrose tends to caramelize at elevated temperature and degrading its effectiveness as fuel component [171].

The existence of third stage extended the reaction time of saccharide-based HAN mixture. This implies heat energy released from the saccharides for a longer period. From Table 3.5, the reaction time for 5 *g* of HAN-sucrose and HAN-dextrose ternary mixtures are as long as 95.67 ± 4.59 *s* and 52.33 ± 11.06 *s*, respectively. HAN-dextrose has a slightly longer t_{total}, which is 3.29 % longer than that of HAN-methanol ternary mixture. The larger heat of reaction resulted from decomposition of sucrose also contributed to larger ΔT_3 than HAN-dextrose, shown in Figure 3.11.

Table 3.5 Time taken for second stage of decomposition to complete (Δt_2), time taken for decomposition to complete (t_{total}), temperature difference between T_2 and T_{max} (ΔT_3) and average temperature during second and third stage ($T_{aveHANfuel}$) for HAN-Dextrose and HAN-Sucrose.

	HAN-Dextrose		HAN-Sucrose	
	Average	**S.D. (%)**	**Average**	**S.D. (%)**
Δt_2 **(s)**	24.0	8.33	43.0	4.17
t_{total} **(s)**	52.33	21.13	95.67	4.71
ΔT_3 **(°C)**	23.50	29.98	46.90	22.70
$T_{aveHANfuel}$ **(°C)**	137.03	1.79	131.04	4.19

As shown in Table 3.5, saccharide-based HAN ternary mixtures have a slightly higher $T_{aveHANfuel}$ than alcohol-based HAN ternary mixtures, showing that decomposition of saccharide-based HAN ternary mixtures released larger amount of energy. $T_{aveHANfuel}$ of HAN-dextrose is higher than that of HAN-sucrose, due to much shorter t_{total} of HAN-dextrose (54.7 %) and close T_{max} (92.6 %), compared to HAN-sucrose.

3.3.3.4 Nitrogen-rich compounds

The temperature profiles for electrolytic decomposition of HAN-nitrogen-rich-compound ternary mixtures were plotted in Figure 3.12, with HAN binary solution as reference.

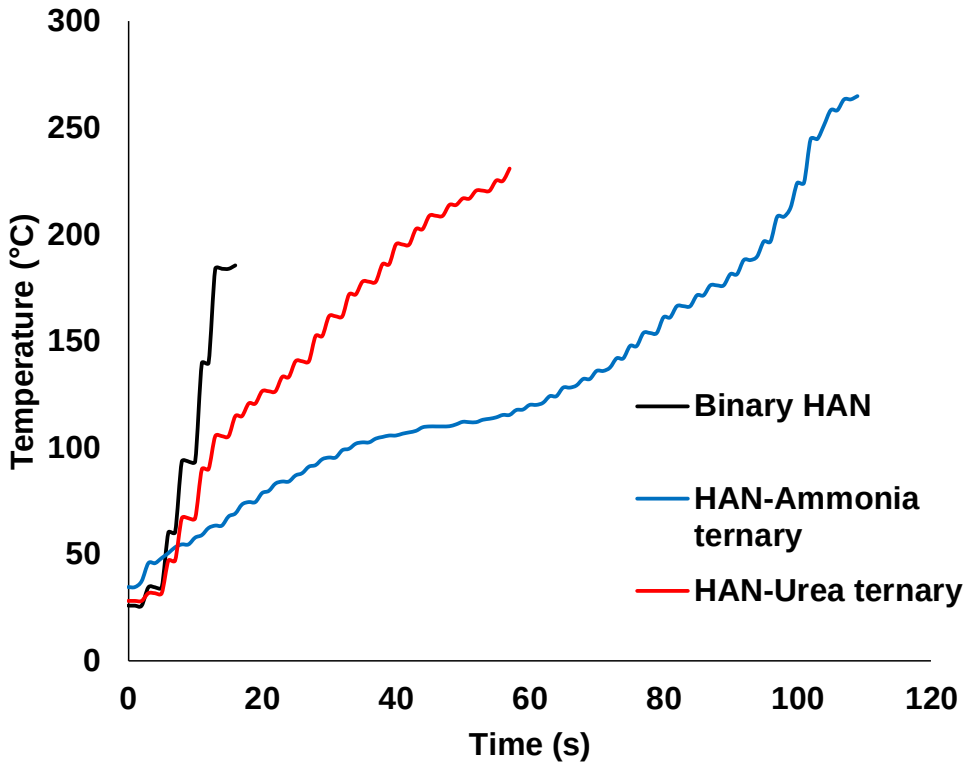

Figure 3.12 Comparison of temperature profile for electrolytic decomposition of binary HAN solution and HAN-nitrogen-rich compounds ternary mixtures.

At the first glance, the temperature profile of electrolytic decomposition of HAN-urea ternary mixture is rather similar to the HAN-alcohol mixtures in which two stages of reaction were observed. A closer inspection by comparing the reaction rates of different HAN ternary mixtures at the first and second stage of electrolytic decomposition is shown in Figure 3.13.

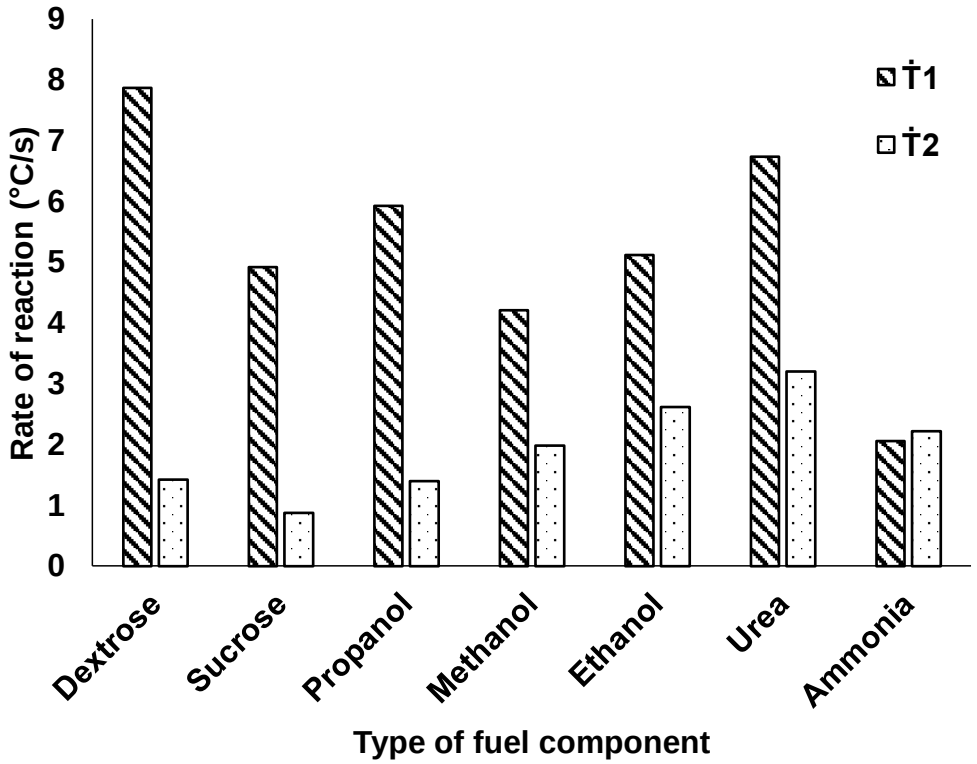

Figure 3.13 Comparison of reaction rates of different HAN ternary mixtures at the first and second stage of electrolytic decomposition.

Of all the cases studied, the temperature profile of electrolytic decomposition of HAN-ammonia ternary mixture is the most unique. Instead of two-stage reaction as observed previously, the electrolytic decomposition of HAN-ammonia ternary mixture took place as if a near single stage reaction. The difference in reaction rates between the two stages is a mere 7.41 %.

While other HAN ternary mixtures have lower reaction rate at the second stage of decomposition reaction, electrolytic decomposition of HAN-ammonia ternary mixture has higher reaction rate at the second stage.

The reaction rate at the second stage of electrolytic decomposition of HAN-urea ternary mixture is noticeably higher than that of the other mixtures. The notable difference in the reaction rate is due to the dissolution of urea into water and undergoes electrolysis process. The electrolysis of urea that occurs at anode can be represented as [172]:

$$CO(NH_2)_2 + 6\ OH^- \rightarrow N_2 + 5\ H_2O + CO_2 + 6\ e^- \qquad \text{R3-13}$$

The production of additional electrons from electrolysis of urea has facilitated the decomposition of HAN at the second stage, due to higher current density, as shown in R3-8 at cathode side reaction, thereby increasing the reaction rate [110, 111].

The electrolysis of ammonia, as shown in R3-14, releases electrons that participate actively in the second stage of electrolytic decomposition. This is consistent with the previous argument for HAN-urea ternary mixture. As a result, the maximum temperature achieved for electrolytic decomposition of HAN-ammonia ternary mixture is the highest at 269.13 ± 11.76 °*C*.

$$2\ NH_3 + 6\ OH^- \rightarrow N_2 + 6\ H_2O + 6\ e^- \qquad \text{R3-14}$$

The reason of lower maximum temperature of HAN-urea than HAN-ammonia ternary mixture was unknown and should be investigated in the future. As seen from Table 3.4, HAN-ammonia achieved the highest T_{max}, however safety issues in handling ammonia mixture (LD_{50} oral 350 *mg/kg*) should be emphasized [173]. As the second rich in

nitrogen containing compound, urea (LD_{50} oral 8471 *mg/kg*) gave the second highest T_{max} among all the fuel mixtures but it is safer to handle.

According to Table 3.6, HAN-urea has a higher second stage average temperature than HAN-ammonia. Decomposition of nitrogen-rich HAN-based ternary mixtures released the highest amount of energy among the three families, as evidenced by the highest average $T_{aveHANfuel}$.

Table 3.6 Average temperature during second stage and time taken for decomposition to complete for HAN-Urea and HAN-Ammonia ternary mixture.

	HAN-Urea		**HAN-Ammonia**	
	Average	**S.D. (%)**	**Average**	**S.D. (%)**
$T_{aveHANfuel}$ **(°C)**	168.82	4.23	153.43	4.43
t_{total} **(s)**	52.67	15.81	108	2.78

T_{max} of each fuel was plotted in Figure 3.14, with their respective time of decomposition for HAN ternary mixture (t_{total}). It was shown that HAN-urea and HAN-ammonia ternary outperformed HAN binary in their respective T_{max} despite the heat energy was released for a longer time. The other four ternary mixtures might underperform binary HAN, for example HAN-sucrose, took longer time to release its energy, which could be used in applications requiring prolonged heat release.

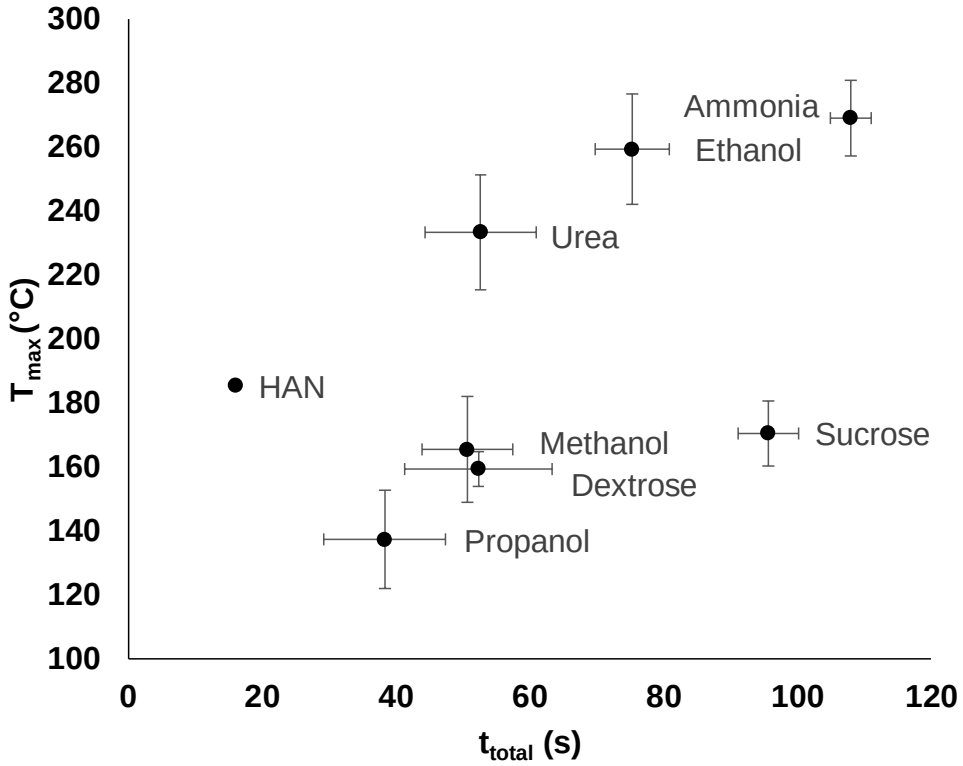

Figure 3.14 Comparison of T_{max} of different HAN ternary mixtures, with HAN as comparison.

The analysis in Figure 3.14 could be further interpreted in determining suitable HAN-fuel combinations for different applications. Electrolytic decomposition performance of HAN-fuel combinations are summarized in Table 3.7.

Table 3.7 Summary of electrolytic decomposition performance of HAN-fuel combinations.

HAN-fuel combinations	T_{max} (°C)	Time (s)
HAN-Methanol	165.47	50.67
HAN-Propanol	137.33	38.33
HAN-Dextrose	159.37	52.33
HAN-Sucrose	170.50	95.67
HAN-Urea	233.40	52.67
HAN-Ammonia	269.13	108.00

3.4 Summary

Synthesis of hydroxylammonium nitrate (HAN) solution was described in the first section, where nitric acid is titrated against hydroxylamine solution under temperature-controlled environment. Further purification to the pristine HAN solution to obtain HAN concentrations of interest, i.e.73 *wt%*. Current work only focuses on this concentration due to safety concern.

Macroscale electrolytic decomposition of HAN ternary mixture was conducted using calorimetric technique to explore the effect of chemical interaction on various mixtures. In general, decomposition of the HAN ternary mixtures have two stages. The reactions are dominated by electrolysis of water in the first stage which demonstrated a notably higher rate of reaction than the second stage.

Electrical resistivity reflects the rate of electron transfer in a particular solution, which is a key process in electrolytic decomposition of HAN mixture. The electrical properties of liquid mixture are closely associated to the rate of temperature elevation ($\dot{T}$) instead of maximum temperature reached during decomposition process (T_{max}).

The rate of reaction in the first stage of electrolytic decomposition shows a general linear trend with respect to the electrical resistivity of the HAN ternary mixtures. As the current remained constant in the first stage, the associated Joule heating has positive assists in the rates of reaction. This showed electrolytic and thermal decomposition took place in the first stage of decomposition. After attaining the boiling point of water, the rate of reaction is independent of electrical resistivity of the HAN ternary mixture. Thus, the second stage of reaction in the electrolytic decomposition of HAN ternary mixtures is dominated by the chemical reactions between remaining HAN and fuel.

The behavior of electrolytic decomposition varies with the type of fuel component added into the HAN ternary mixtures. The electrolytic decomposition for mixture containing saccharides evolves into a three-stage reaction and releases more energy. The maximum temperatures obtained from the nitrogen-rich-compounds-based HAN ternary mixtures, i.e. urea and ammonia, are the highest among all the HAN ternary mixture studied because the production of additional electrons from electrolysis of urea and ammonia has facilitated the electrolytic decomposition reaction.

In summary, this chapter provides another perspective towards decomposition of propellant mixtures. Electrochemical-related physical property is important for the performance of the mixture. This study provides a preliminary benchmark for decomposition which will be carried out in future studies.

Chapter 4 Design and fabrication of microreactor system

4.1 Introduction to microfabrication

Xurographic microfabrication technique uses common vinyl film in which the design was plotted using cutting plotter machine and transferred into a glass mold for multiple replica molding process. This fabrication technique was favored for short fabrication time (< 4 hours), low startup cost, no requirement of clean room facilities as well as relatively lesser equipment needed compared conventional microfabrication techniques such as deep reactive-ion etching (DRIE) and soft-lithography.

However, xurography disadvantageous in offering low resolution as low as 10 *μm*, compared to other fabrication techniques. Besides, microchannel defects in cutting operation and adhesion of film to cutting blade is common. To counter these defects, a technique was developed to tackle the aforementioned shortcomings. This chapter aimed at providing detailed description of fabrication technique employed the setup used for microscale decomposition in Chapter 5.

An appropriate design was created using xurographic technique and a positive vinyl film was produced on a glass mold subsequently. It was then followed by replica production, where PDMS was used as a structural material. Incorporation of microelectrodes is important in leading to triggering of electrolytic decomposition in an electric insulating

PDMS. Lastly, fabrication of the microreactor was completed through chemical bonding to another PDMS layer. The details of the fabrication is described in the following Section 4.2.

For microscale decomposition of HAN solution, a high speed camera setup was used to capture images of decomposition will be described in Section 4.3. In the same section, different techniques in triggering the high speed camera are elaborated. A switch was integrated into the experimental setup, enabling a better control over triggering of electrolytic decomposition with the power supply and high speed camera. Analysis of the high speed camera triggering techniques is described in Section 4.4 and image analysis technique employed in this study will be further discussed in Section 4.5, to give a better understanding of the technique.

The challenges that overcame in this chapter are as below:

1. Concept of integrating DPST switch into the high speed camera visualization setup

2. Cost-effectiveness and stability of DPST switch

3. Using of image analysis technique to determine the HAN reaction rate

4.2 Fabrication of PDMS microreactor

The cutting plotter which was used in the work is shown in Figure 4.1(A). The front and side view of the cutting plotter blade are shown in

Figure 4.1(B) and (C), respectively. Parameters optimization using the cutting plotter (CE6000-60, Graphtec, Japan) was carried out in the group and is described in the Section 4.2.1.

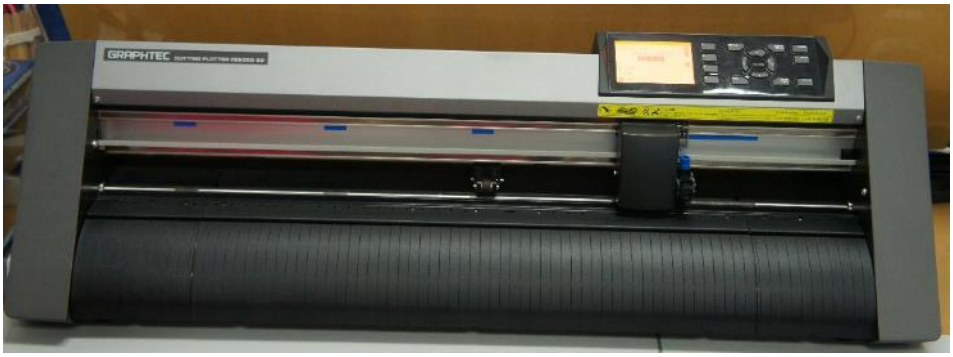

(A)

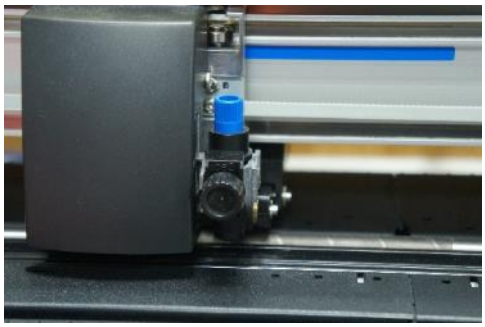

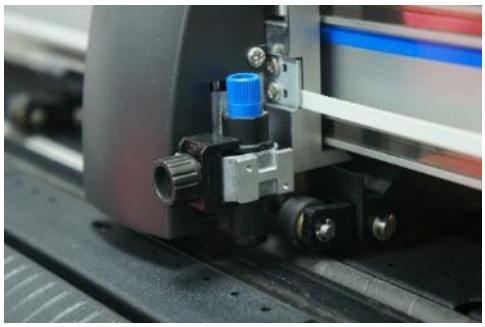

(B) (C)

Figure 4.1 (A) Photograph of cutting plotter, (B) Front view of cutting plotter blade, (C) Side view of cutting plotter blade.

The cutting of vinyl film was schematically illustrated in Figure 4.2. The optimum blade length should exceed the thickness of vinyl film in order to have a good cut on the vinyl film.

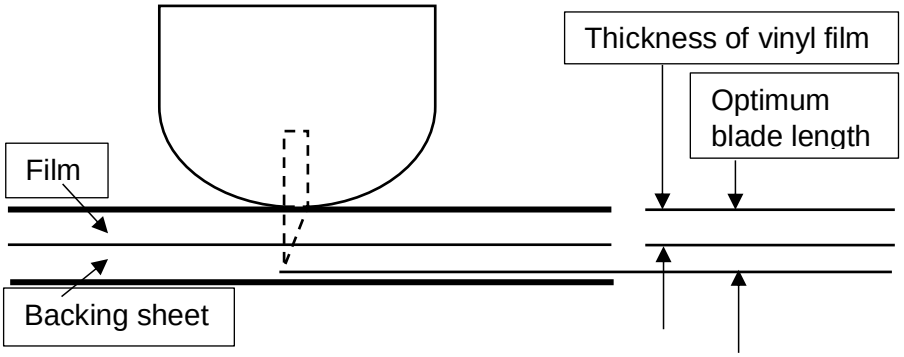

Figure 4.2 Schematic diagram to illustrate the cutting of vinyl film.

4.2.1 Cutting plotter parameter optimization

In xurography, there are two main cutting parameters that determines good cutting. They are:

1. Cutting mode
2. Cutting force

As the vinyl film is 180 *μm* thick, cutting blade CB09UA was chosen as the diameter and the angle of the blade is 0.9 mm and 45 °, respectively. It is most commonly available and it is suitable for thickness of media up to 250 *μm*.

The slowest speed and acceleration of the cutting blade (1 *cm/s* and 1 cm/s^2, respectively) was chosen to provide the highest resolution possible. The material independent machine setting was found to be best, which include offset angle, offset force and step pass to be 0, 4, 0, respectively.

4.2.2 Cutting mode

Three types of cutting methods are used in cutting plotters, namely drag knife (TM0), true tangential (TM1) and emulated tangential (TM2), as shown in Figure 4.3.

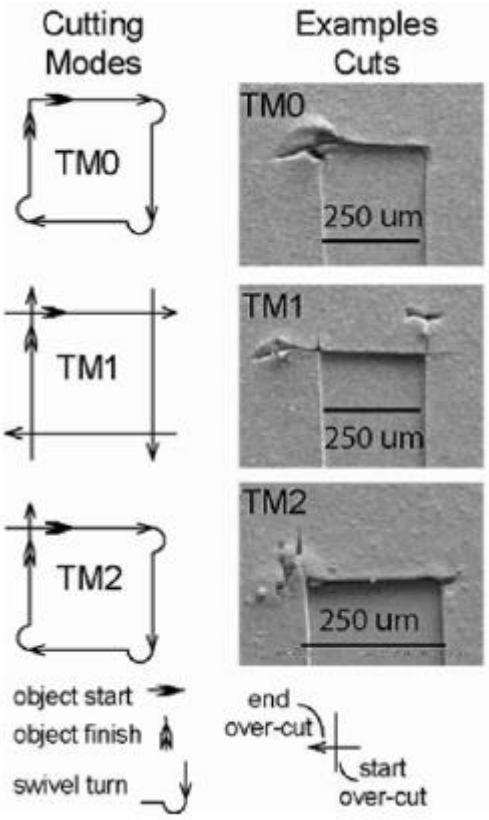

Figure 4.3 Illustration of cutting modes [126].

The advantages and disadvantages are stated in Table 4.1.

Table 4.1 Advantages and disadvantages of three cutting modes.

	Advantages	**Disadvantages**
Drag knife (TM0)	Follows cutting path of the feature as it moves relative to material	Introduces lateral force from the blade at sharp feature corners
True tangential (TM1)	Feature corners are completely cut using over-cut	Not particularly useful for designs with more curves
Emulated tangential (TM2)	Reduces lateral force on the blade	Feature corners are completely severed from the rest of the material

True tangential mode (TM1) was employed in this study as the design consists of a number of feature corners.

4.2.3 Cutting force

The force settings were gradually increased until it was possible to remove the square without putting up the triangle, thus indicating a complete cut.

The optimized parameters were tabulated in Table 4.2.

Table 4.2 Optimized cutting plotter condition

Cutting plotter model	Graphtec CE6000
Cutting blade	CB09U
Cutting force	12
Offset force	4
Speed	1 *cm/s*
Acceleration	1 cm/s^2
Cutting mode	TM1
Offset angle	0
Step pass	0
Over-cut	100 *μm*

4.2.4 Fabrication of microreactors using xurographic technique

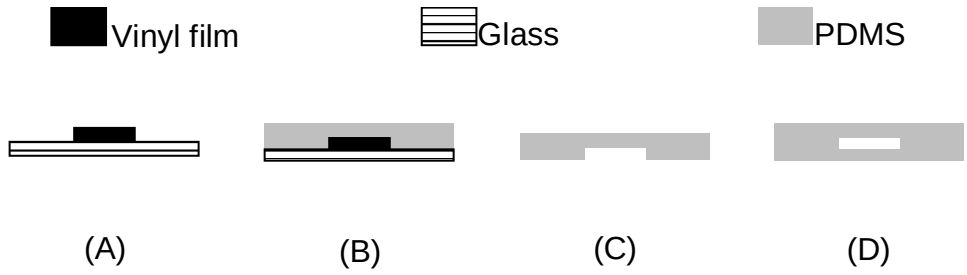

Figure 4.4 Schematic of xurography technique. (A) Preparation of master mold, (B) PDMS replication, (C) De-molding, (D) Sealing to form microreactor.

Fabrication process of the transparent microreactor is schematically shown in Figure 4.4, which is a standard method used to make microfluidic devices. The process consists of four major steps:

(1) Preparation of the master mold

(2) Replication of microreactor design onto PDMS layer

(3) De-molding of replicated PDMS layer

(4) Sealing of the layer to form the microreactor

Xurography technique was used to produce the positive pattern of the microreactor design [126]. The pattern was drawn using a professional graphical package (CorelDraw X7, Canada) and cut on a vinyl film (Oracal 651, Orafol, Germany) of 180 *μm* thick using a cutting plotter (CE6000-60, Graphtec, Japan), as shown in Figure 4.1(a). The pattern was transferred onto a glass petri dish using a transfer liner, as shown in Figure 4.2(A).

In the second step, the PDMS polymer mixture (Dow Corning, Sylgard 184, USA), consisting of the prepolymer and curing agent at 10:1 ratio was prepared and poured onto the master mold, Figure 4.2(B). After the mixture was thermally cured, the PDMS layer which replicated from the design patterns was peeled off from the master mold, as shown in Figure 4.2(C). After creating an inlet and outlet for the replicated PDMS layer, it was chemically bonded to a back PDMS layer using tetrabutylammonium fluoride (TBAF) solution to form an enclosed microreactor, Figure 4.2(D).

PDMS microreactor was fabricated to investigate the effect of number of copper electrode pair, HAN flowrate and voltage on electrolytic decomposition phenomena at microscale. Commercial copper wires of

diameter 300 *μm* (Element 14, BS 6231, Malaysia) were manually inserted from the side to serve as electrodes in microreactor. Microreactor has three pairs of electrodes, respectively. The chamber width and length for microreactor is 2 and 6 *mm*, respectively. The microreactor was divided into two sections in the analysis, in which the first half, denoted as L1, consists of the microreactor chamber with electrodes. The second half, denoted as L2, is an elongated chamber from the microreactor chamber, to further investigate the efficiency of the decomposition. The completed microreactor is shown in Figure 4.5, in comparison with a Malaysia 10 cents coin, accompanied by SEM image of the exit view of microreactor.

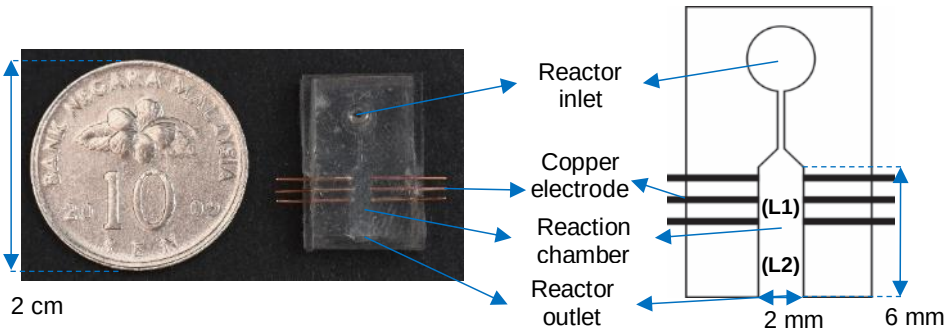

(A) (B)

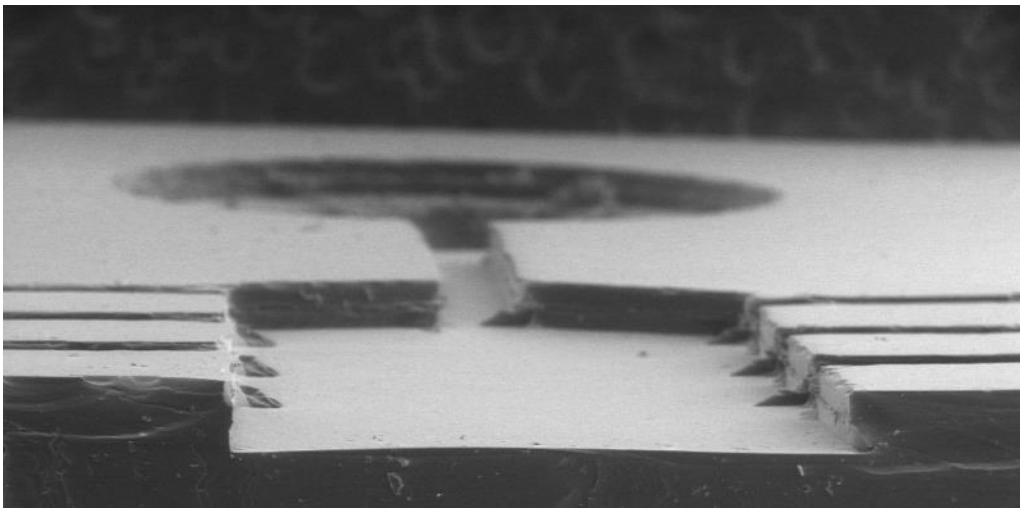

(C)

Figure 4.5 (A) Microreactor device overview. Fabricated microreactor device in comparison with a Malaysia 10 cents coin, (B) Schematic of the microreactor, showing L1 and L2 section specifically, with L1 and L2 in the first and second half of the reactor length, respectively, (C) SEM image of the exit view of the microreactor.

4.3 Visualization of Electrolytic Decomposition of HAN solution at microscale

The experimental setup for visualization of electrolytic decomposition of HAN in PDMS microreactor is shown in Figure 4.6. The transparent PDMS microreactor was placed under a light inverted microscope (Olympus, IX51, Japan) with the HAN solution delivered into the microreactor continuously via a syringe pump (KD Scientific, KDS 210, US). After filling up the entire microreactor with the HAN solution, electrolytic decomposition was initiated using a DC power supply (Elektro-Automatik, PS-8080-12-2U, Germany) which is able to supply voltages range from 0 to 80 *V*.

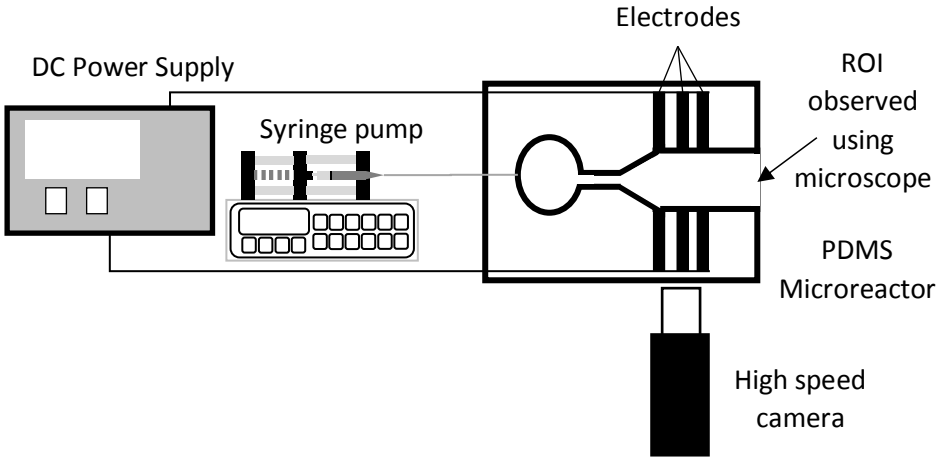

Figure 4.6 Schematic diagram of standard high speed camera setup.

Electrolytic decomposition of HAN solution is an instantaneous event. A high speed camera (Phantom, Miro M110, USA) attached to the microscope recorded the sequences of decomposition of HAN solution. During the experiment, decomposition phenomena were captured at

speed of 5000 *frames per second* (*fps*). A double pole single throw (DPST) switch was integrated into the setup enabling the decomposition phenomena to be captured more accurately. Once the switch is closed, the open circuits of DC power supply to the electrodes and internal circuit of the high speed camera will be closed simultaneously. The falling edge of voltage in the high speed camera itself was used to trigger the high speed camera, hence the entire decomposition of HAN solution in the microreactor can be captured.

The images captured were analyzed using the image analysis software (ImageJ, v1.49q, U.S. National Institutes of Health, USA), which is able to evaluate the region of interest (ROI) occupied by gas bubbles generated during the decomposition of HAN solution, which is the L1 section, whereas the L2 section serves as an efficiency study. The images were extracted and processed to obtain boundaries of bubbles in ImageJ and respective bubble areas were measured. Complete schematic setup of the experimental setup for visualization of electrolytic decomposition of HAN solution at microscale is shown in Figure 4.7.

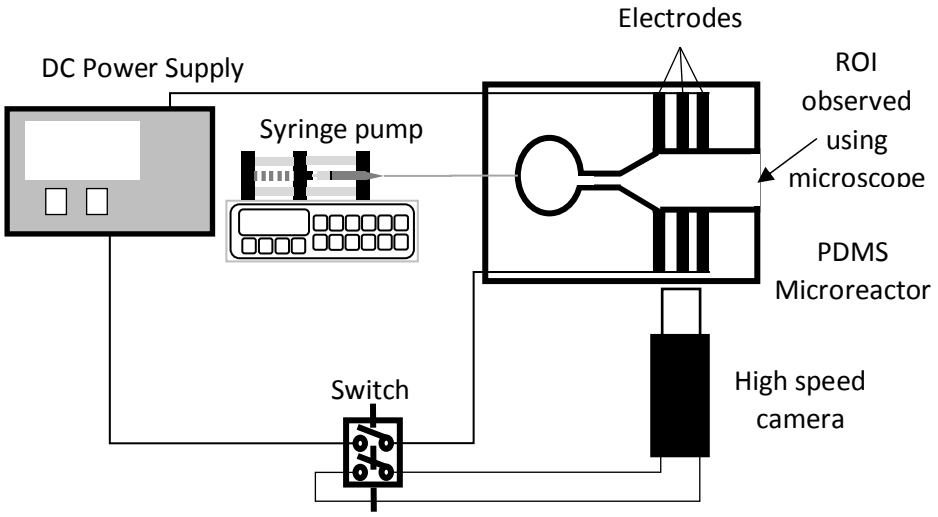

Figure 4.7 Schematic diagram of experimental setup with addition of DPST switch.

The complete microscale electrolytic decomposition of HAN in PDMS microreactor is shown in Figure 4.8. The highlighted part in Figure 4.8(A) showing the platform, where the microreactor was placed during the experiment, is further zoomed in and is shown in Figure 4.8(B).

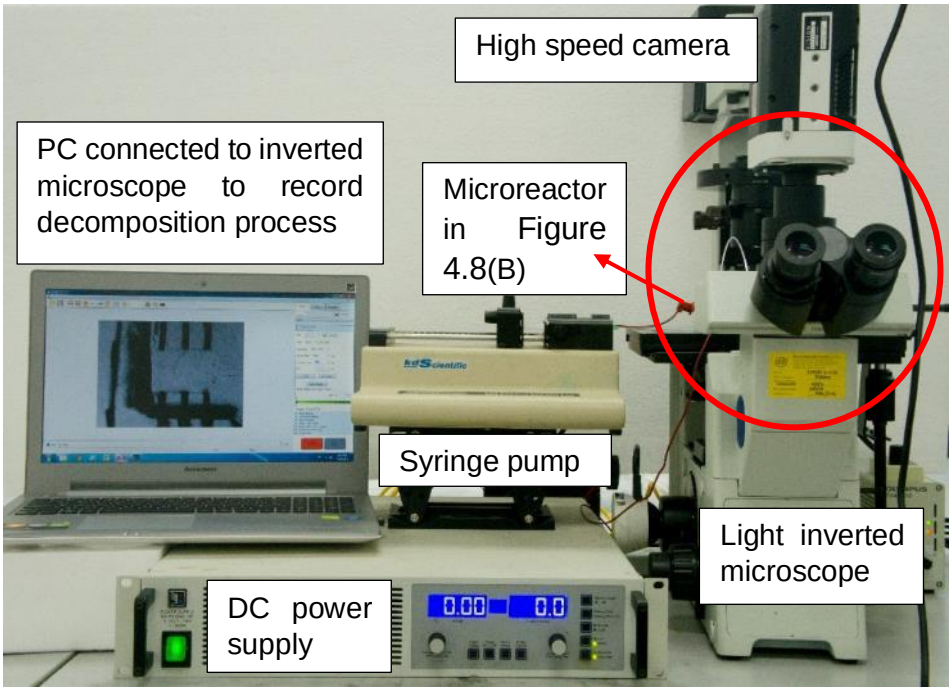

(A)

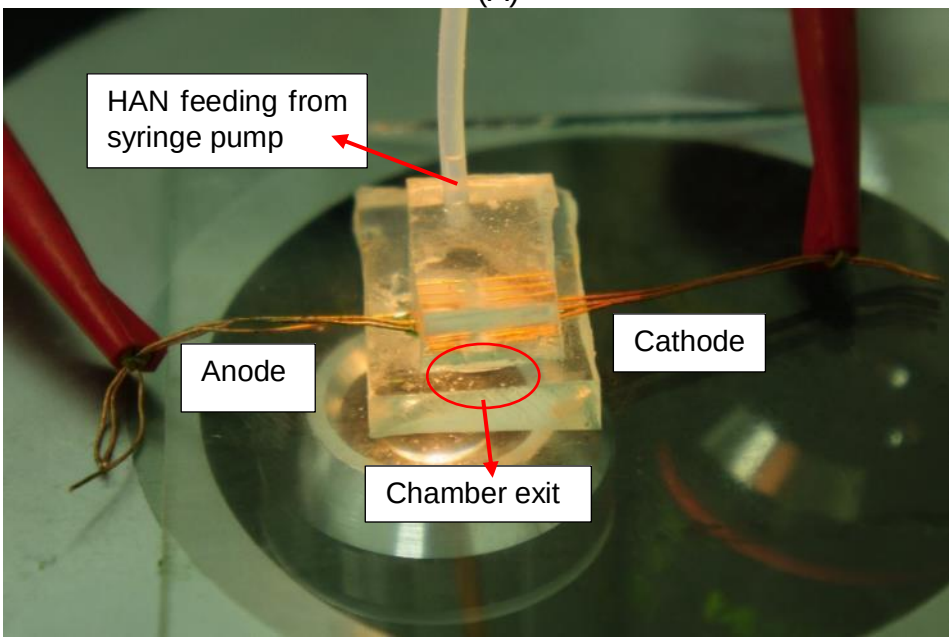

(B)

Figure 4.8 (A) Microscale electrolytic decomposition of HAN solution setup, (B) zoom in of the highlighted area of the platform containing microreactor.

4.4 High speed camera triggering method

Triggering of high speed camera is important in the decomposition experiment as proper triggering enables the time frame of the decomposition to be captured accurately. There are two main triggering categories available in the high speed camera itself, which is soft triggering and hard triggering. The triggering method available in each triggering category for high speed camera, with its respective usage is summarized in Table 4.3. Some advantages and disadvantages of using both triggering methods are also stated in Table 4.3.

Although hard triggering method is able to synchronize with digital acquisition (DAQ) system, other hard triggering methods are not able to capture initiation of decomposition accurately. While applying a low transistor-transistor logic (TTL) pulse signal is able to synchronize with DAQ system, DAQ system itself is costly. Hard triggering method is selected throughout the work, with the effort to integrate into the high speed microscale decomposition setup at lower cost.

Ideally, triggering of the high speed camera should correspond to the starting of the experiment, in which electrons start to flow though the HAN solution in PDMS microreactor. In manual triggering by switch, de-pressing the switch will close the internal circuit of the high speed camera, creating a falling edge in the circuit, from +5 V to ground. The delay time from detection of falling edge to triggering is 32 μs, as it is the default filter time for the high speed camera itself.

Taking advantage of such a short delay time, the ideal case could be realized if two circuits could be closed together. Normally, a DAQ system will be used. However, the costliness and bulkiness of the entire DAQ system making it not user friendly. Thus, in order to be cost-effective and minimize resources used, semi-automation was employed. The two methods were selected and evaluated for their usefulness, which are image-based auto trigger and manual triggering with a DPST switch. The switch used in manual triggering was replaced with a RM 6 (approximately $ 1.50) DPST switch.

Table 4.3 High speed camera triggering methods and usage.

Category	Triggering method	Usage	Pros	Cons
Soft trigger	Manual triggering in recording software	Most direct method in soft triggering, where navigation and triggering in recording software are done manually	• Trigger camera remotely without external device • Adjust the triggering time	• Hard to control, leading to low repeatability
	Image-based auto trigger	Automatically trigger the camera when exceeds set value of change in area within ROI		
Hard trigger	Manual triggering by switch	Manually trigger the camera with some distance	• More direct method in triggering with or without external device	• Costly DAQ system integration
	Depressing trigger button on camera itself	Most direct method to trigger the camera		
	Applying a low TTL pulse signal	To be used with DAQ system		

4.4.1 Comparison between image-based auto trigger and DPST switch

In current work, bubble growth profile was selected as analysis ground work. Although limited by equipment for gas analysis, image analysis on bubble growth could provide information such as reaction rate, steady state bubble area, decomposition efficiency. In this subsection, performance of both image-based auto trigger (IBAT) and DPST switch will be compared and discussed.

Image-based auto trigger was first being chosen due to its ease in operation and readily available in the software provided. The camera will trigger itself when the change in area and light exceeded the set value. The sensitivity parameter is crucial in making the trigger as accurate as possible. As decomposition only resulted in bubbles, which will appear as black color as edges in the region inspected, the light threshold value remained constant. The pixel and area change % threshold value were set to 2 and 0.01 %, respectively. The values were determined from the software, resulting in triggering with lowest delay.

DPST switch, on the other hand, was chosen due to its high feasibility with manual triggering in the high speed camera setup. The DPST switch closes two independent circuits altogether, enabling it to trigger the high speed camera and electrolytic decomposition of HAN in PDMS microreactor at the same time.

Comparison of bubble area ratio on time scale, using IBAT technique and DPST switch, was shown in Figure 4.9. The deviation

between trials of IBAT technique is larger than that of DPST switch. This resulted in inconsistency during analysis, especially in the determination of starting point of decomposition and also the calculation of rate of reaction. Furthermore, pre-ignition delay could not be recorded properly. DPST switch, on the other hand, have a more consistent results among different trials. Pre-ignition delay and the trends could also be recorded.

In this subsection, it can be concluded that DPST switch implementation is more suitable for this study. Subsections below consisted of the characterization of a DPST switch.

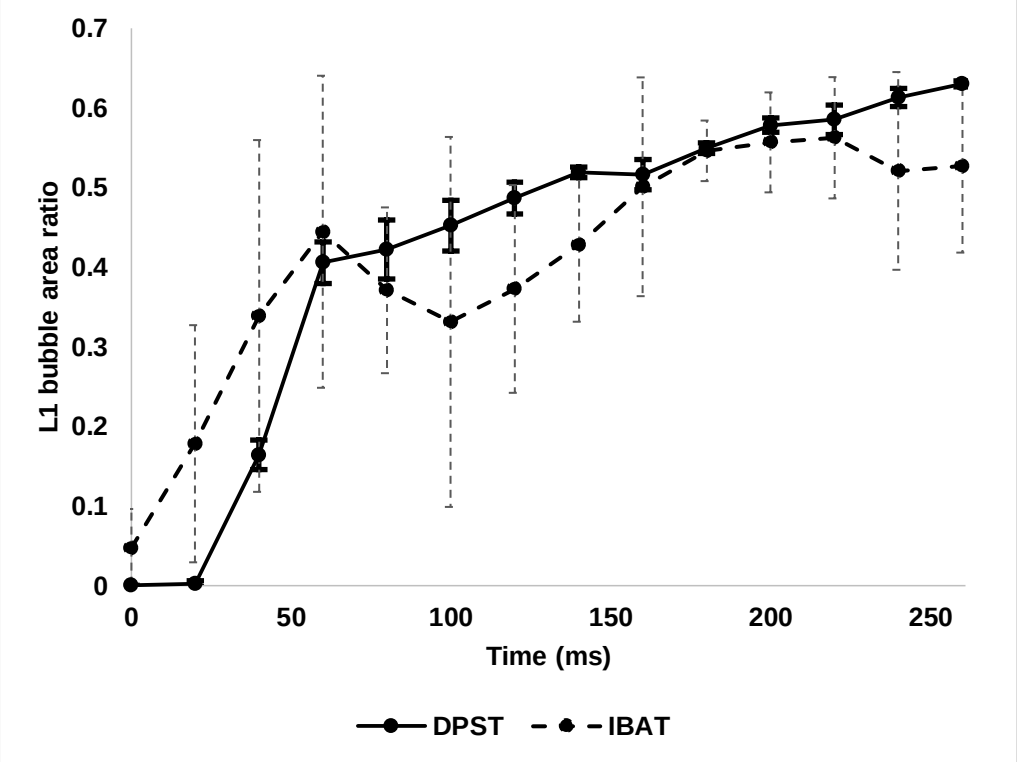

Figure 4.9 Comparison of bubble area ratio as a function of time between setup with DPST switch (solid line) and image-based auto trigger (dotted line), (mean ± *SD* (n=3)), error bars were plotted according to *SD* relatively to each triplicate.

4.4.2 DPST switch delay test

This subsection focuses on implementation of DPST switch selection method criteria. DPST switch was selected due to its cost effectiveness, as compared to a data acquisition (DAQ) system. The following subsection will be divided into two parts, which is the delay of the switch and also the stability of the switch.

A common switch and a DPST switch has one and two pair of input and output terminals, respectively, in which they can be connected or disconnected with a single throw. The DPST switch, which has two output terminals, enable it to drive two independent circuits at the output. The high speed microscale decomposition setup consisted of two independent circuits, the main electric circuit in the decomposition system and triggering in high speed camera.

As compared to a DAQ system, the implementation of switch is more cost effective. This subsection deals with the delay between the channels. An oscilloscope (Tektronix, TDS 1002B, USA) was employed to test the delay between the two channels by using a Bayonet Neill–Concelman (BNC) cable. The setup was schematically shown in Figure Figure 4.10.

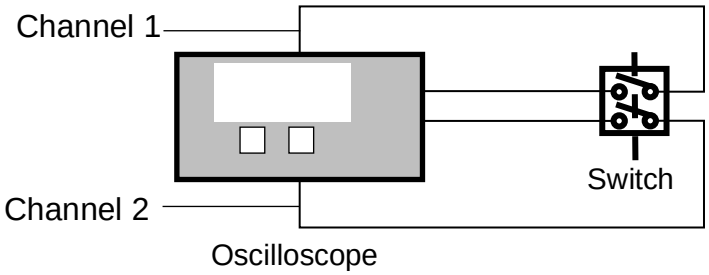

Figure 4.10 Schematic diagram of DPST switch delay test.

Each channel of the oscilloscope contains signal and ground. Oscilloscope is able to record the noise signal in an electrical circuit. When the circuit is open, the oscilloscope detects the potential difference between two ports; but when the circuit is closed, the circuit is 'grounded' and thus, the noise level will be reduced to zero. In this case, there will be two signals suddenly reduced to zero. The DPST switch delay is obtained by the difference where both curves hit zero.

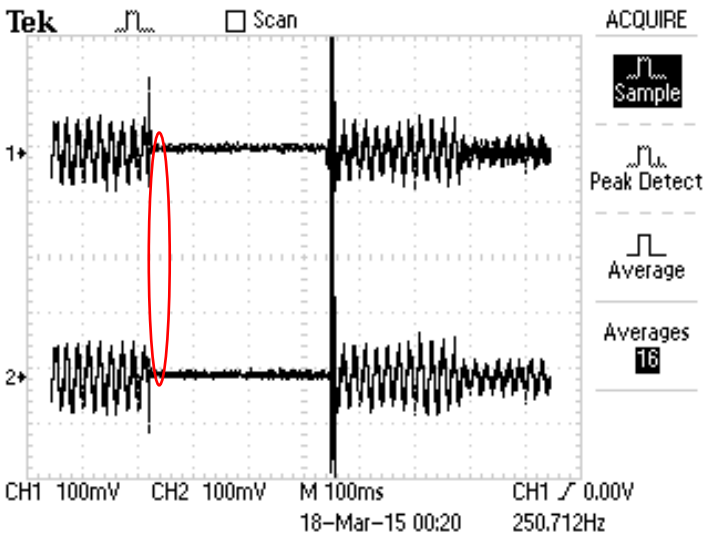

Figure 4.11 Sample of oscilloscope recording.

The part highlighted in red Figure 4.11 was zoomed in and was shown in Figure 4.12. The first and second channel are at their lowest at

224.8 *ms* and 223.6 ms, respectively, which means the delay is 1.2 *ms*. The delay is 2.6 ± 0.9562 *ms*. It can be concluded that the DPST switch implementation will impose a maximum delay of 4 *ms*. Image analysis was carried out at a minimum of 4 *ms*, thus the DPST switch maximum delay is within acceptable range.

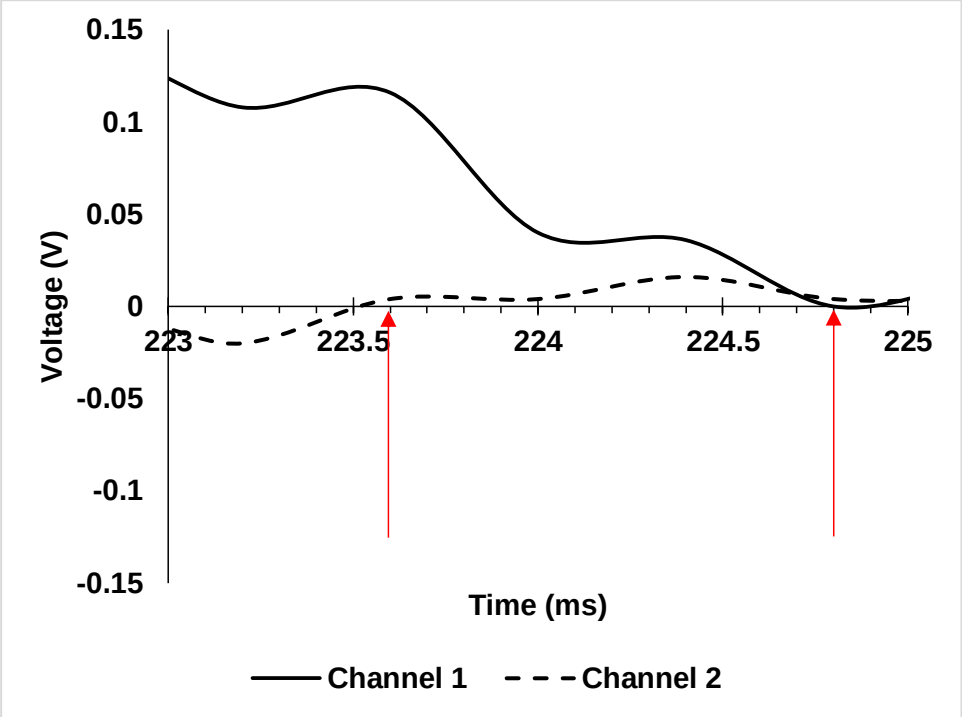

Figure 4.12 Zoomed in part of the circled section in Figure 4.11.

4.4.3 DPST switch safety test

As electrolytic decomposition of HAN is performed, current will be drawn continuously from power supply to the microreactor. A range of different voltages will be applied during the study. Thus, constant usage of the DPST switch need to be investigated.

A LED was placed in channel 1, connected to the positive terminal of DC power supply, and another power line was connected to channel 2, connected to negative terminal of DC power supply. If the switch failed, the inner of the switch would melt, resulting in two independent circuits to connect together, causing the LED to light up for a short period of time. If the power provided was higher than that of power required, the LED will be overpowered and will not light up. The setup was schematically shown in Figure 4.13.

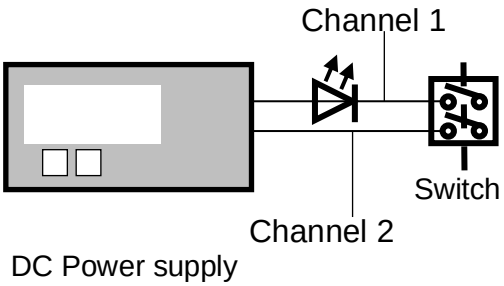

Figure 4.13 Schematic diagram of DPST switch stability test.

The test was conducted for voltages ranging from 1 to 80 V, with a constant current of 0.1 A. Each test lasted for 5 minutes and was repeated at least thrice for repeatability purpose. The LED was still able to light up after testing, showing that the switch did not have a meltdown after testing with all the voltages. Hence, it is concluded that the switch is safe to use under different voltages.

4.5 Image analysis method

The entire decomposition was recorded in Vision Research Phantom CINE camera video file (CINE) format of high speed camera, as the video quality is of the highest that the high speed camera is able to provide. The video was extracted into images prior to post image analysis. This subsection discusses about the image extraction method.

The CINE video was converted into series of frame of images. The interval of the images was selected as below:

1. The interval was 4 *ms* from the initiation of the experiment till 20 *ms* during the initiation stage
2. The interval was 20 *ms* from point 1 onwards till 250 *ms*

The short interval at the beginning is due to rapid increase of bubble area in the first 20 *ms* for high voltage case. The images were converted into .TIFF format in order to be analyzed in the ImageJ software, as .TIFF format offers higher bit depth, and better thresholding.

As shown in Figure 4.14, the first frame in a series of images was identified as the initial frame (0 *ms*). New image was produced by obtaining the absolute value of difference between the initial image and the to-be-analyzed image. The new image will then have less boundary of microreactor and more focus on the bubble itself. The resulted image was then being thresholded. The area enclosed in the region is the bubble area. Analysis was performed on the bubble area obtained and will be further discussed in Chapter 5.

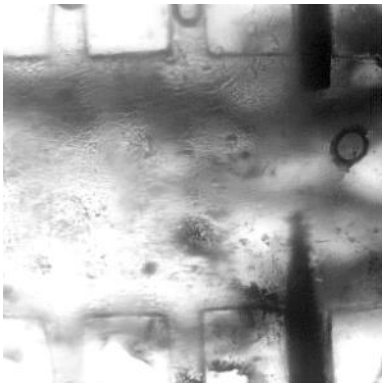

(A) First frame

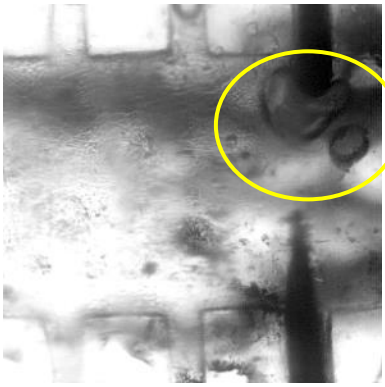

(B) To-be-analyzed image

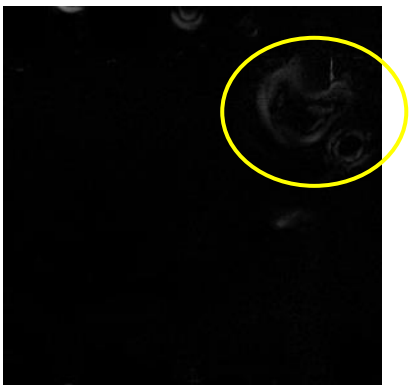

(C) New image

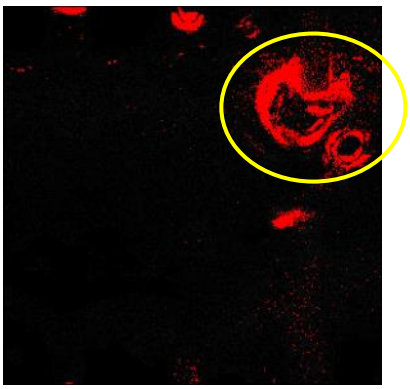

(D) Thresholded image

Figure 4.14 Images captured and used in analysis. (A) First frame of the series of image, (B) To-be-analyzed image, (C) Resulted new image from the difference between (A) and (B), (D) Thresholded image showing thresholding being applied.

Image extraction steps were outlined as below in Figure 4.15.

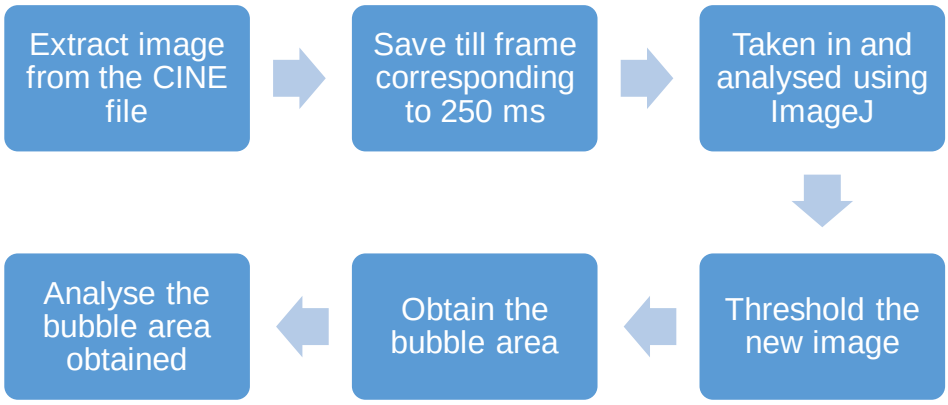

Figure 4.15 Image extraction steps.

4.6 Summary

Fabrication of PDMS microreactors were detailed and xurography was successfully demonstrated to fabricate the microreactors used in this study. The complete visualization setup using high speed camera was detailed and displayed.

Current bubble area ratio study compares the bubble growth profile by using image-based auto trigger and DPST switch integration. DPST switch integration shows a more repeatable trend than image-based auto trigger. This indicates DPST switch integration is more effective in triggering high speed camera. DPST switch was integrated into the high speed camera setup, enabling the decomposition phenomena of HAN to be captured successfully. Testing results show that DPST switch delay between two channels is acceptable within the image analysis range and it is safe to use under all voltages.

Image analysis was also demonstrated successfully in analyzing the images captured. The current image analysis method was adjusted to obtain the results effectively.

Chapter 5 Microscale decomposition of HAN

5.1 Introduction to microscale decomposition of HAN

As highlighted previously in introduction section (Section 1.3.1), excessive heat loss occurring at microscale, due to high surface area to volume ratio, hinders development of metal microchambers. To overcome this issue, ceramic-based material, which is of lower heat conductivity, was studied and employed to fabricate such systems. However, ceramic-based microthruster, which has low thermal expansion ratio and resistance to thermal shock, cracked after testing, showing the importance of controlling the reaction rate and to avoid associated pressure build up from exceeding the limit of material properties of ceramic [22].

Conventional microchambers or microthrusters were fabricated using opaque materials, such as metal and ceramic, because of their capability at high temperature, typically 1000 °*C* or higher. However, visualization of decomposition phenomena inside the microchamber is impossible. Although two-phase flow had been demonstrated in metal reactor, the decomposition phenomena of HAN was not studied in depth, only qualitative results were presented [165]. PDMS was chosen as structural material for microreactor in this current work due to its optical accessibility.

In this chapter, electrolytic decomposition of HAN solution at microscale using a PDMS microreactor was demonstrated visually and

the reaction rate was studied comprehensively, with optimization of parameters affecting the reaction rate. The optimized parameters were used on the best performing HAN ternary mixture, as obtained in Chapter 3. The performance was then compared against the HAN binary solution. The microreactor was examined under scanning electron microscope (SEM) to investigate the damage that the decomposition done to the PDMS microreactor.

In current work, a few parameters were studied, including:

1. Effect of number of electrodes

Investigating effect of number of electrodes in microreactor on HAN decomposition can be interesting, as it affects the total surface area for reaction. Moreover, by increasing the number of electrodes, more initiation sites are available for reaction. Increase in electrode surface area facilitates ion exchange between electrode and HAN in microreactor, which enhances the overall decomposition performance. Therefore, the investigation on the effect of number of electrodes on the decomposition of HAN solution is detailed in Section 5.2.

2. Effect on flowrate of HAN

As the entire decomposition was carried out under flowing HAN solution, flowrate of HAN solution has a significant impact towards the decomposition phenomena. HAN flowrate is inversely proportional to its residence time in the microreactor. An optimum flowrate is required for

HAN to be decomposed efficiently. Effect of flowrates on decomposition of HAN solution is detailed in Section 5.3.

3. Effect of applied voltage

Voltage is a measure of difference in drive for electron flow. Higher voltage affects the entire system directly by easing the flow of electrons between electrodes. Determining the threshold voltage is critical to minimize power required to initiate decomposition in microscale. Effect of applied voltage of HAN solution is detailed in Section 5.4. Optimization of these parameters can lead to a more cost-effective approach in overall. This chapter is aimed at providing detailed analysis of results employing the microscale decomposition setup described in Chapter 4.

5.2 Electrolytic decomposition of HAN solution

As a charge-rich ionic liquid, HAN solution decomposes when a potential difference is applied. The overall decomposition mechanism of HAN is still not well understood due to complex multiple reactions. As such, the role of each component was discussed in Section 3.3.1. As chemical reactions took place in the reaction chamber, the end products of the reactions are gaseous products. In this study, we assumed that the reaction is rapid (ignition in microseconds scale), all end product are gases and the rate of gas bubble formation is equivalent to rate of reaction.

The sequential event for the electrolytic decomposition of HAN solution using 1 pair of electrodes was captured using the high speed camera and depicted in Figure 5.1. The images from A1 to A3 were captured at interval of 4 *ms* but appeared to be identical as there was no occurrence of decomposition. This implies the existence of delay in decomposition of HAN solution after the DC voltage was applied. The decomposition delay is 16 *ms* for 1 pair of electrodes. Short delay is an added benefit for realization of a responsive micropropulsion system. As a consequence, the propulsion system can be operated more frequently.

Once the decomposition of HAN solution is initiated, a few small bubbles started to appear at the cathode, as shown in B1. The small bubbles continued to grow and coalesced to bigger bubble within 40 *ms*, as seen from B2 to B3. As the decomposition progresses, the bubble grew larger and occupied most of the area of the ROI, as shown in C1 to C3. A steady state of the reaction is achieved.

There is bubble generation on the anode side from 0 to 20 ms, but the rate is insignificant compared to the cathode side. This is most likely due to dominance of gas generation on the cathode side at microscale. As mentioned in Section 3.3.1, cathode side reaction is more dominant than the anode side as the number of moles of hydrogen generated is more than oxygen. Oxygen is also more water soluble than hydrogen. However, further work should be carried out to verify this issue.

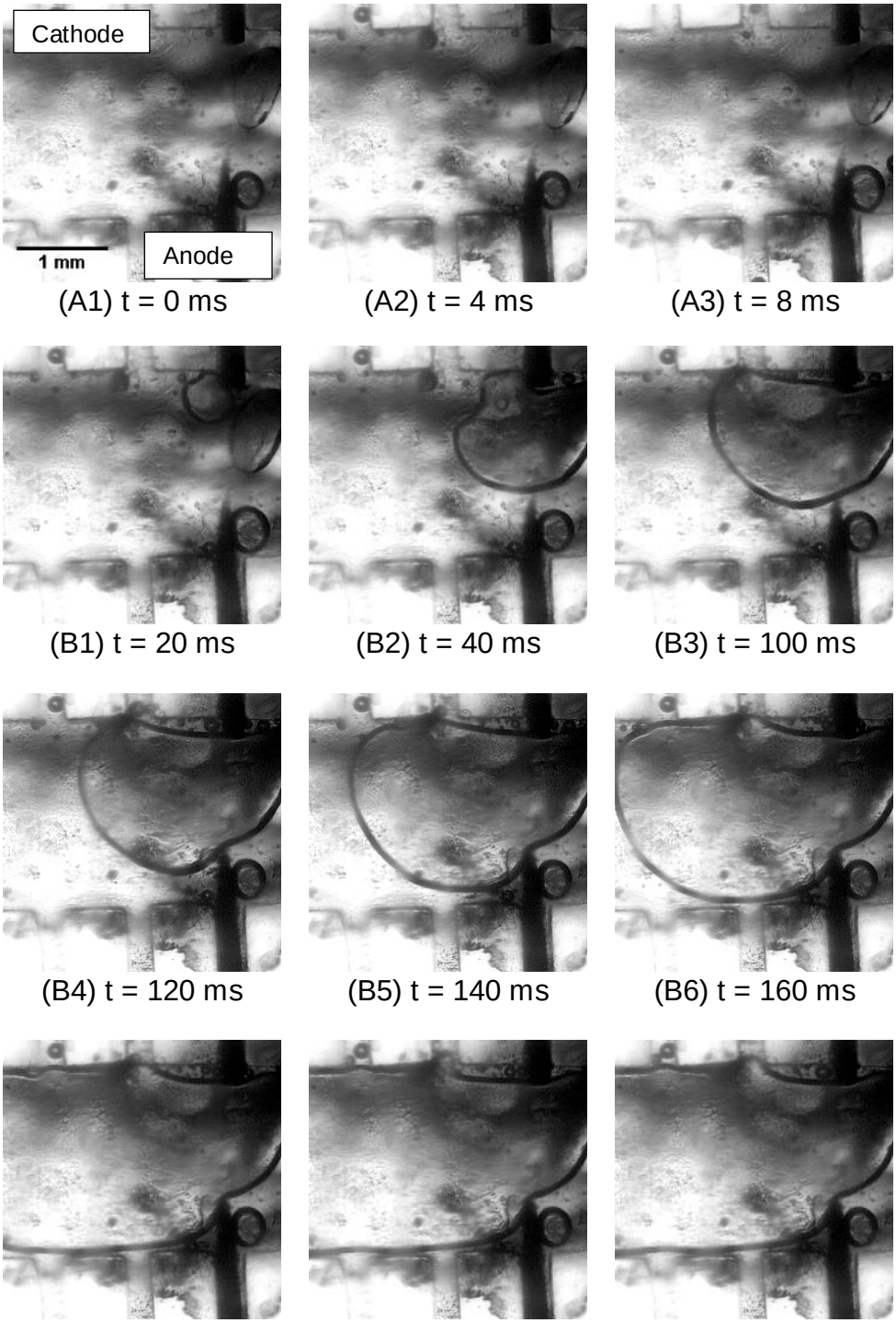

Figure 5.1 Images captured using the high speed camera to show the decomposition of HAN propellant flowing in the microreactor with 1 pair of electrodes at 50 *µl/min* and applied voltage of 50 *V*.

5.3 Effect of number of electrodes on decomposition of HAN solution

Parametrical studies on electrolytic decomposition of HAN solution was conducted with the electrolytic decomposition being detailed in Section 5.2. Previous study has shown that choice of electrode played an important role in electrolytic decomposition of HAN solution [115]. Although different material was studied and compared, effect of number of electrodes in microscale reaction was not reported elsewhere. Electrodes used in this study focuses only on copper electrodes, with the change in number of electrodes, as the electrode is common and could be extended from previous result. Separate electrode entity has to be considered instead of single electrode entity in this case. Such approach can greatly reduce the total volume of electrodes used, thereby increasing the decomposition efficiency.

Electrodes are expected to provide more sites for reaction of discharging of copper ions. Thus, number of electrodes towards decomposition phenomena was investigated. The sequential event for the electrolytic decomposition of HAN solution using 3 pairs of electrode is depicted in Figure 5.2. The interval of images A1 – A3 is identical to their counterparts in Figure 4.13 for the ease of comparison. In overall, the phenomenon of HAN decomposition using 3 pairs of electrode (surface area 1.0602 mm^2) is very similar to that of using 1 pair of electrodes (surface area 0.3534 mm^2). From the successive images captured, delay in the decomposition of HAN was observed too.

Nevertheless, there is a distinctive difference in the formation of bubbles in the anode. Small bubbles were seen forming at each cathode, as evidenced by more gaseous components being released at cathode-side reaction in Section 3.3.1. These small bubbles coalesce and grow separately until they are large enough to occupy the chamber.

The effect non-homogeneity of the shape of the electrodes did not affect the accuracy of the results obtained, as described in Section 5.5.1. The effect of distance of electrode from reservoir and the location of the electrode towards the overall reaction rate were confirmed by the visual inspection of the thinning of the third anode in Figure 5.2. It showed that the reaction rate is higher with increased distance of electrode.

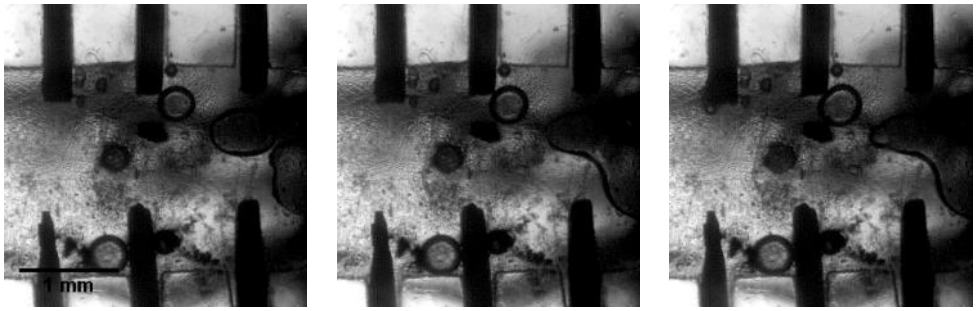

(A1) t = 0 ms (A2) t= 4 ms (A3) t = 8 ms

(B1) t = 20 ms (B2) t = 60 ms (B3) t = 100 ms

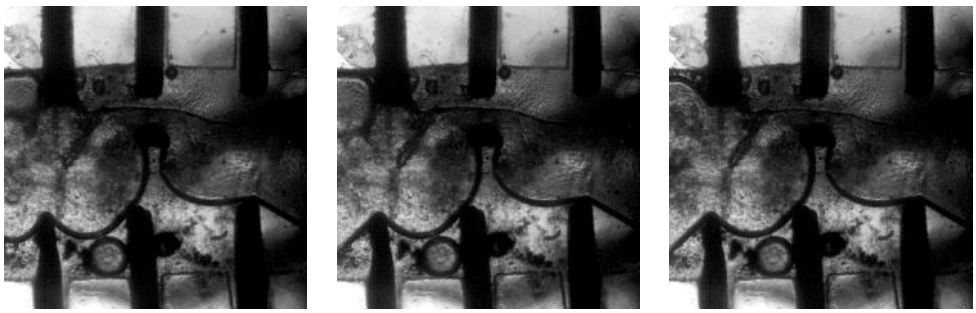

(C1) t = 200 ms (C2) t = 220 ms (C3) t = 240 ms

Figure 5.2 Images captured using the high speed camera to show the decomposition of HAN propellant flowing in the microreactor with 3 pair of electrodes at 50 *µl/min* and applied voltage of 50 *V*.

In analysis of the images, bubble (gas phase) area ratio is defined as the ratio of area occupied by the bubble to the total area of *ROI*. Higher ratio implies more gases released and a more complete reaction. The change in bubble area ratio in L1 section during the electrolytic decomposition using 1 pair and 3 pairs of electrode was evaluated respectively and plotted in Figure 5.3 for comparison.

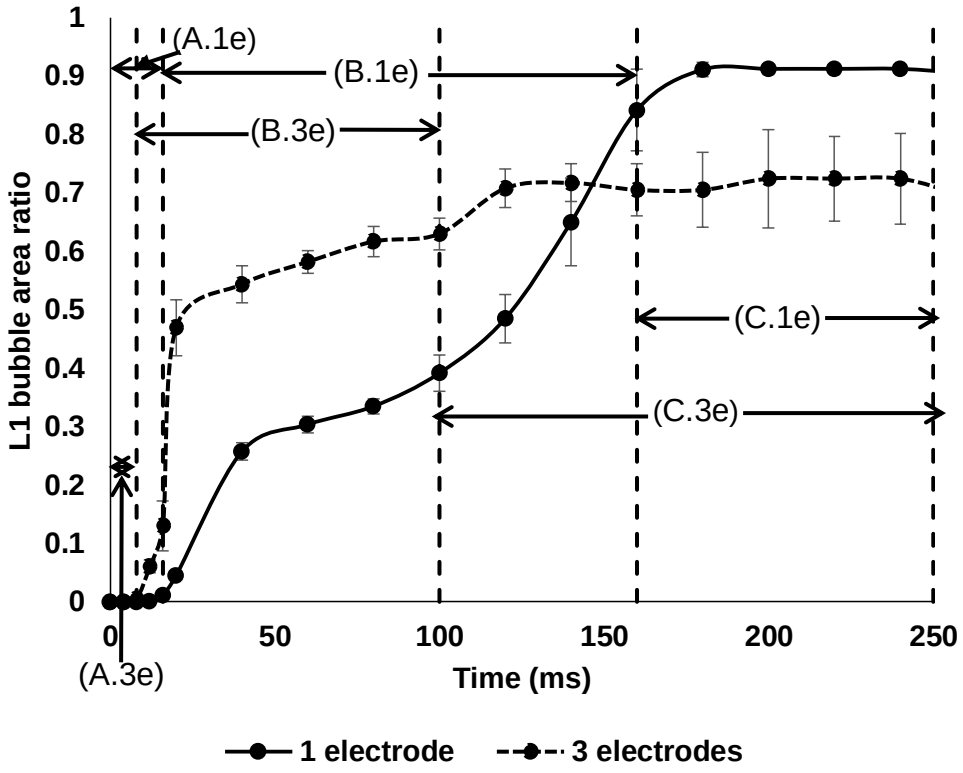

Figure 5.3 Change in area of ROI covered by bubble generated from decomposition of HAN solutions feeding at 50 *µl/min*, with comparison between 1 and 3 electrode pair.

The figure can be divided into three distinct regions. The region designated as (A) represents the delay in decomposition of HAN in which the bubble area is zero. The delay was shortened by half to 8 *ms* when 3 pairs of electrodes was used. Shorter delay means HAN is more

responsive, thereby reducing the overall delay when initiating HAN in an electrolytic decomposition.

The increase in bubble area ratio in region (B) marks the start of electrolytic decomposition of HAN, as shown in Figure 5.3. A similar trend of increase in bubble area ratio was observed for using 1 pair and 3 pairs of electrode in initiating the decomposition.

Initially, the bubble areas grew rapidly as evidenced by the steep slopes in region (B), followed by slowdown in their growths and grew drastically again before reaching the peak value. By consuming the energy released at the early stage of decomposition, a portion of water content in the HAN solution was evaporated. The concentrated HAN became reactants for the subsequent thermal decomposition which released more energy in the later stage of reactions and accelerated the growing of bubbles [101].

After this transition period, the bubble area is stable and finally reaches the steady state at region (C). This is known as bubble area ratio at steady state thereafter. Alternatively, the ratio can be evaluated from the amount of decomposed HAN solution at steady state which is represented by the difference between the amount of feeding and residual HAN in the microreactor. However, it is noteworthy that the growth of bubble area could be affected by compressibility of air and should be taken into consideration. As the chamber is open to atmosphere and the pressure buildup is negligible due to absence of nozzle, thus compressibility of air was assumed to be constant in our

study. As this study is focused on the decomposition phenomena during the ignition period and it occurred very rapidly, thus our study focused on the first 250 *ms* of the decomposition.

3 pairs of electrodes have initiated higher rate of decomposition of HAN solution. Approximately 50 % of the chamber area (*ROI*) was filled by the bubble within the first 25 *ms* of reaction. In contrast, it required up to 40 *ms* for 25 % of the chamber area filled with the bubble produced using 1 pair of electrodes. In overall, it takes a shorter time of approximately 120 *ms* for decomposition of HAN solution to achieve steady state using 3 pairs of electrodes. The time taken has increased by 50 % to 180 *ms* for using 1 pair of electrodes. This is attributed to the additional pair of electrodes which provide increased surface area for initiation.

The advantage of increase in reaction rate by using 3 pairs of electrodes is achieved with the expense of reaction stability. The bubble area ratio in the region (C.1e) maintained almost constant throughout the course, showing that the decomposition was a stable and sustained reaction. However, the bubble area ratio was fluctuating after achieving the maximum. This fluctuation is due to inconsistent contact between the in-flowing HAN solution and 3 pairs of electrodes. Such phenomenon also observed in decomposition of HAN droplets [112]. On a separate note, the bubble area ratio at steady state using 3 pairs of electrodes is about 20 % lower than that using 1 pair of electrodes. The electrodes protrude from the edge of microchannel due to the difficulty to ensure a

perfect insertion at this micro-scale level. As such, the narrow gaps between protruded electrodes have trapped some of the in-flowing HAN solutions. Worst still, the enhanced hydrodynamic resistance of the narrow gap due to its smaller dimension than the chamber width restricted the fresh HAN solution from entering the gap. Restricted in-flowing of HAN solution reduced HAN solution in contact with the electrodes, leading to lower bubble area ratio for 3 electrode pairs setting.

t = 300 ms t = 400 ms t = 500 ms

Figure 5.4 Continuous decomposition was ensured as an extension from Figure 5.1

The electrolytic decomposition was able to be sustained after the ionic flow between the electrodes was blocked by the gaseous product. Continuous decomposition occurred after 250 ms in the micro channel experiments, as shown in Figure 5.4. Continuous gaseous flow was also observed at the exit of the channel after the initial process shown in Figure 5.1 and 5.2.

In this subsection, 3 electrodes perform better than 1 electrode pair at giving a higher overall reaction rate and a shorter pre-ignition delay under the same setting. However, the 3 electrode pairs has

achieved lower bubble area ratio, as compared to 1 electrode pair. Finalized parameters for entire study were stated in Table 5.1.

Table 5.1 Operating condition for entire study.

Flowrate (*µl/min*)	25, 50, 75, 100, 125
HAN concentration (*wt%*)	73
Applied power (*W*)	30, 40, 50, 60, 70 (30 – 70 *V*, 1 *A*)
Chamber pressure	Open to atmosphere

5.4 Effect of flowrates on decomposition of HAN solution

Understanding the decomposition of HAN solution at different flowrates has significant implication as the flowrate has a significant impact on contact time. The overall reaction rate is taken from the gradient in entire section in region (B) as an indication of reactivity of electrochemical reaction and plotted in Figure 5.3. The rate of bubble growth represents the rate of gaseous components released during the electrochemical reactions, which corresponds to the reaction rate. The "reaction rate" is the gas generation rate as a result of HAN decomposition. The ability to trigger and achieve targeted reaction rate at lower flowrate is desired, leading to lower usage of propellant.

In Figure 5.5, the reaction rate for using 3 pairs of electrodes can be as high as 225 % as compared to its counterpart using 1 pair of

electrodes. It is consistent with the previous study of *Koh* and *Kuo* that higher flowrates favor the reaction rate [14, 165].

In general, higher flowrate pushes the bubbles downstream more rapidly and increases the frequency of contact between the in-flowing HAN solution with copper electrodes, thereby increasing the overall reaction rate. However, the increment in overall reaction rate with flowrate is not indefinite.

When the flowrate was increased to a sufficiently high level (100 *µl/min* and 50 *µl/min* for 1 and 3 electrode pairs, respectively), the overall reaction rate began to decline, because the frequency of contact between the in-flowing HAN solution with copper electrodes exceeded the rate of decomposition at the copper electrodes. This suggests sufficient residence time is required for deposition of electrical energy into HAN solution to initiate the decomposition.

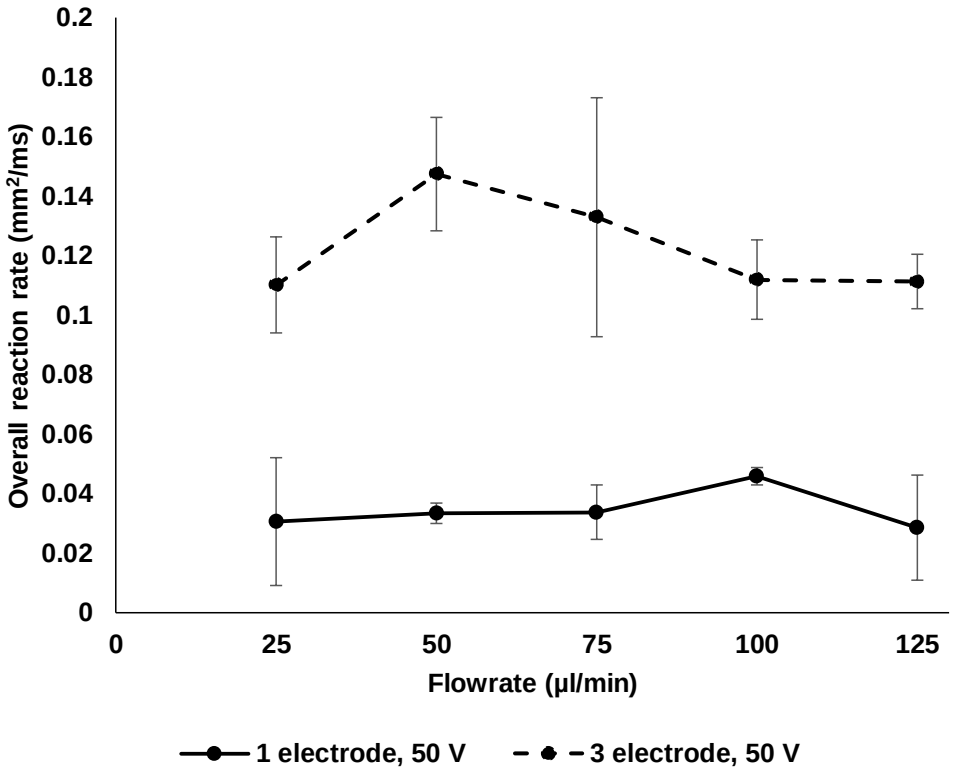

Figure 5.5 Influence of flowrates towards overall reaction rate.

Completeness of the decomposition of HAN solution at a particular flowrate is critical for its application in micropropulsion system. Complete decomposition of HAN solution will release maximum amount of hot gases which consequently produce the maximum level of thrust. The bubble area ratio at L1 section at different flowrates was evaluated and plotted into Figure 5.6.

At flowrate as low as 25 *µl/min*, both 1 and 3 pairs of electrodes managed to decompose the HAN solution almost completely as indicated by the bubble area ratio approaching the value of unity. As the flowrate increases, the bubble area ratio drops in both cases. It is noteworthy that the completeness of decomposition of HAN using 1 pair of electrodes shows only marginal reduction with increasing flowrate from 50 to 100

µl/min. The bubble area ratio is 0.81 ± 0.05 at the highest flowrate of 125 *µl/min*. From the images taken at this flowrate, the gas bubbles only generated at cathode and continued to grow. The bubble only elongated but not disrupted, even when flowrate was increased. This means that for 1 pair of electrodes, the decomposition only focused on one site instead of multiple sites. This shows that continuous decomposition of in-flowing HAN solution was ensured with no other electrode pair to compete with.

On the other hand, the bubble area ratio for 3 pairs of electrodes reduced significantly with the increasing flow rates. At the highest flowrate tested (125 *µl/min*), the bubble area ratio has dropped to a mere 0.55 ± 0.02. The image captured at this flowrate shows numerous bubbles of different sizes near the anode electrodes. At this flowrate, the residence time of 2.074 *s* is too short for those smaller bubbles to coalesce into a bigger bubble and drifted away by the in-flowing HAN solution. This has disrupted the electrochemical reaction which causes an incomplete decomposition of HAN. Calculations for residence time was shown in Appendix I. As the flowrate is increased, the decrease in L1 bubble area ratio represents decrease in the decomposition completion. Low flowrate is therefore more desired as HAN decomposition is more complete at low flowrate. Therefore, it is critical to determine the optimum flowrate for different electrode pair setting to achieve complete HAN decomposition.

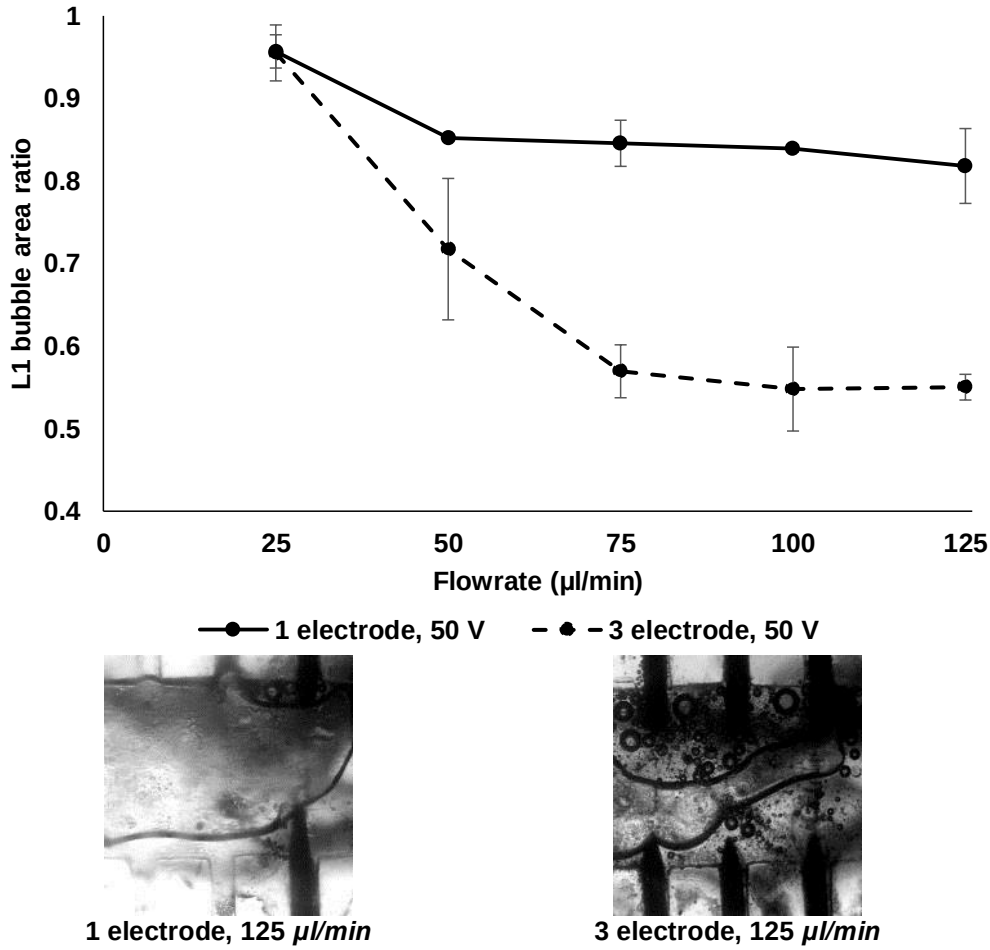

Figure 5.6 Influence of flowrate on the completeness of decomposition.

The zoomed in images of the chamber including both sections of L1 and L2 are illustrated in Figure 5.7, to inspect the completeness of decomposition of HAN after leaving the electrodes. At flowrate of 25 *µl/min*, the decomposition is complete at L2 for both cases of 1 pair and 3 pairs of electrodes, as shown in Figure 5.7 (a) and (c). This justifies the importance of residence time for the complete decomposition of HAN solution.

At flowrate of 125 *µl/min*, the strong hydrodynamic force has pushed a small amount of HAN solution to pass through the chamber

without any decomposition, as highlighted in red circle region in Figure 5.5 (b). The continuity of the bubble formed by 1 pair of electrodes has restrained more HAN solution from escaping without reaction. This explains the completeness of the reaction at 80 % or above for all flowrates tested.

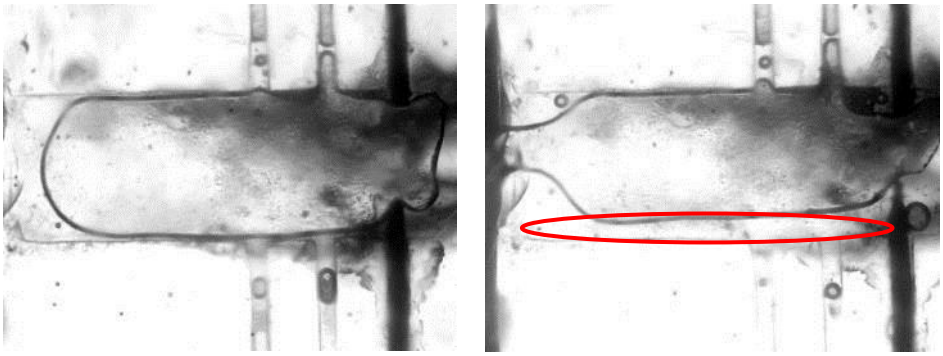

(a) 1 electrode, 25 *µl/min*

(b) 1 electrode, 125 *µl/min*

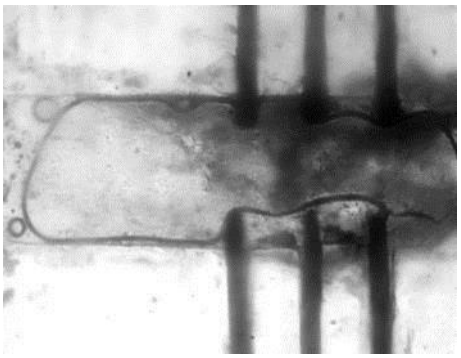

(c) 3 electrode, 25 *µl/min*

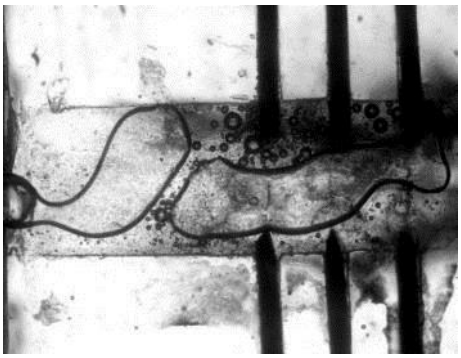

(d) 3 electrode, 125 *µl/min*

Figure 5.7 Completeness of HAN decomposition at different flowrates. Applied voltage is 50 *V*.

In the case of using 3 pairs of electrodes for 125 *µl/min*, the small bubbles at the electrodes fail to coalesce to bigger gas bubbles. This causes more HAN solution leaving the chamber without decomposition.

The situation does not improve but worsen in L2 as the moderately coalesced bubble has broken into two due to the high shearing force from the increased flowrate, Figure 5.7(d).

As can be observed in Figure 5.7, as the flowrate is increased from 25 to 125 *µl/min*, the hydrodynamic resistance of the narrow gap between the electrodes became more noticeable, resulting from the dead volume formation, which causes the effective area of decomposition to reduce under the influence of flowrate, as shown in Figure 5.8(B). The actual residence time is lower than the calculated value, which should take into account of the reduced decomposition area. This also explains the optimum reaction rate (peak) for 3 pairs of electrodes occurred at lower flowrate in Figure 5.3, as compared to 1 pair of electrodes.

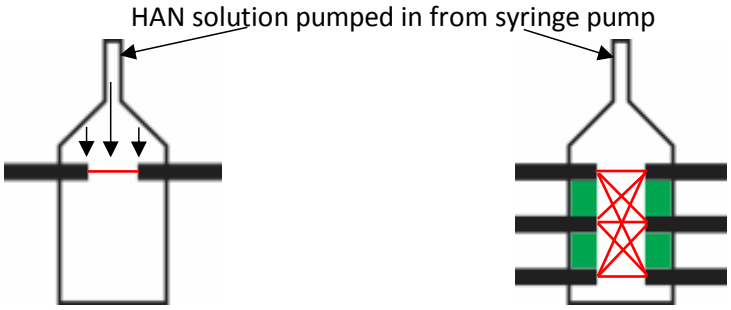

Figure 5.8 Illustration of decomposition involved in (A) one, and (B) three pairs of electrodes.

As seen in Figure 5.8, as the initiations sites are increased in 3 pairs of electrodes case, the selectivity of initiation sites increased as well. For example, the NH_3OH^+ ion which evolved at the anode has 3 cathodes to choose from, instead of 1 cathode, in the case of 1 pair of electrodes. As number of electrodes pair increases, the dead volume formation becomes more apparent, as opposed to point ignition in the case of 1 pair of electrodes.

In this subsection, the highest overall reaction rate could be achieved with an optimum flowrate for 1 and 3 electrode pair setting. Overall reaction rate for 3 electrode pair setting is generally higher than that of 1 electrode pair setting. Despite having advantage over overall reaction rate, L1 bubble area ratio during steady state is generally lower for 3 electrode pair setting, as compared to 1 electrode pair setting. Discontinuity of the bubbles resulted in escaping of HAN solution, in 3 electrode pair setting.

5.5 Effect of applied voltage on decomposition of HAN solution

Applied voltage has always been the most critical parameter in studying electrolytic decomposition of HAN solution, as voltage provides the potential for driving the electrolytic decomposition. This study focuses on the fundamental of decomposition phenomena, as the phenomena of each parameter could be visualized, and explained quantitatively. The

applied voltage has to be optimized to save energy on initiating decomposition on microscale.

Effect of applied voltage towards reaction rate is depicted in Figure 5.9, with the applied voltage varied from 30 to 70 *V*. The overall reaction rate is directly proportional to the applied voltage. Higher applied voltage results in more electrical energy directly deposited into the HAN solution, resulting in a higher reaction rate [22, 109, 112]. The difference in overall reaction rate by using 1 pair and 3 pairs of electrodes is considerably small at applied voltage threshold of 30 V. As the applied voltage is increased, the difference becomes significant. The trend is identical for all flowrates tested.

At the highest applied voltage of 70 *V*, the using of 3 pairs of electrodes has decomposed the HAN solution at a rate of as high as 4 times in comparison to the using of 1 pair of electrodes. It is noteworthy that from 60 to 70 *V*, 3 following conditions: 1 electrode, 25 *µl/min*, 3 electrodes, 75 *µl/min* and 3 electrodes, 125 *µl/min* have highest increase in overall reaction rate as the voltage is increased. This shows that using 70 *V* at these conditions will have a higher overall reaction rate.

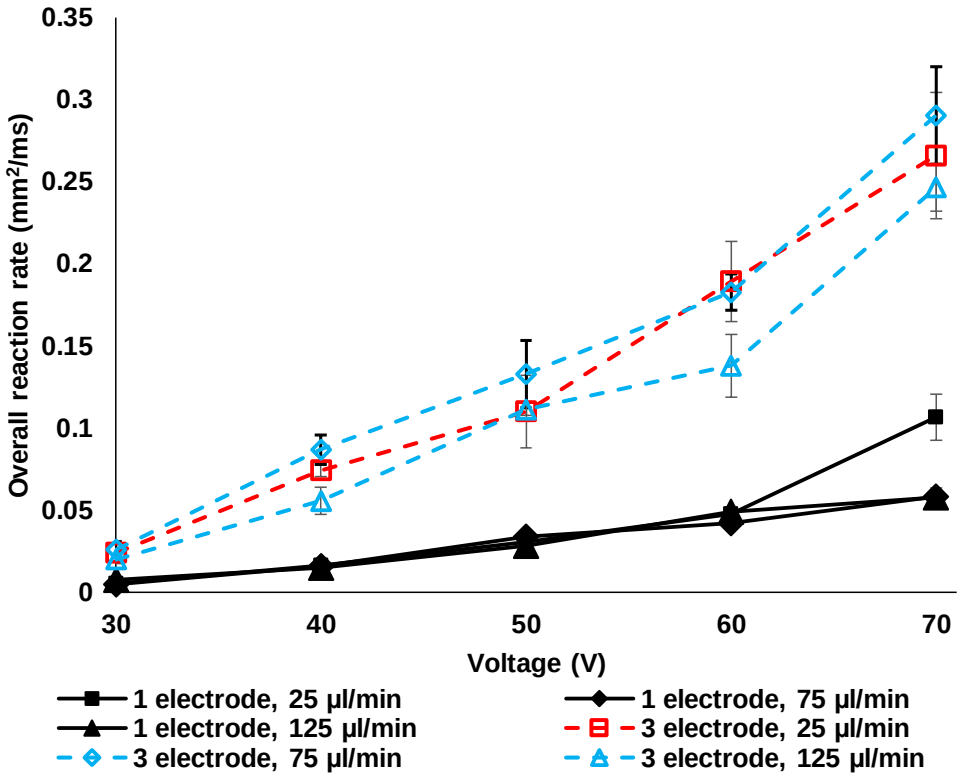

Figure 5.9 Influence of voltage towards overall reaction rate.

The effect of applied voltage to the completeness of decomposition is studied and presented in Figure 5.10. Under applied voltage of 30 *V*, the bubble area ratio at L1 was only approximate 0.25 for the case of using 1 pair of electrodes at low flowrate of 25 *µl/min*. A medium size bubble (approximately 25 % of *ROI*) was seen forming at the electrode without growing further into a bigger bubble to occupy the chamber. As the applied voltage was increased to 40 *V* and above, the bubble area ratio at L1 section increased sharply to a range of 0.75 to 0.96, depending on the flowrates, due to higher potential to drive the electrolytic decomposition. This suggests that a higher applied voltage is required to initiate a sustained decomposition.

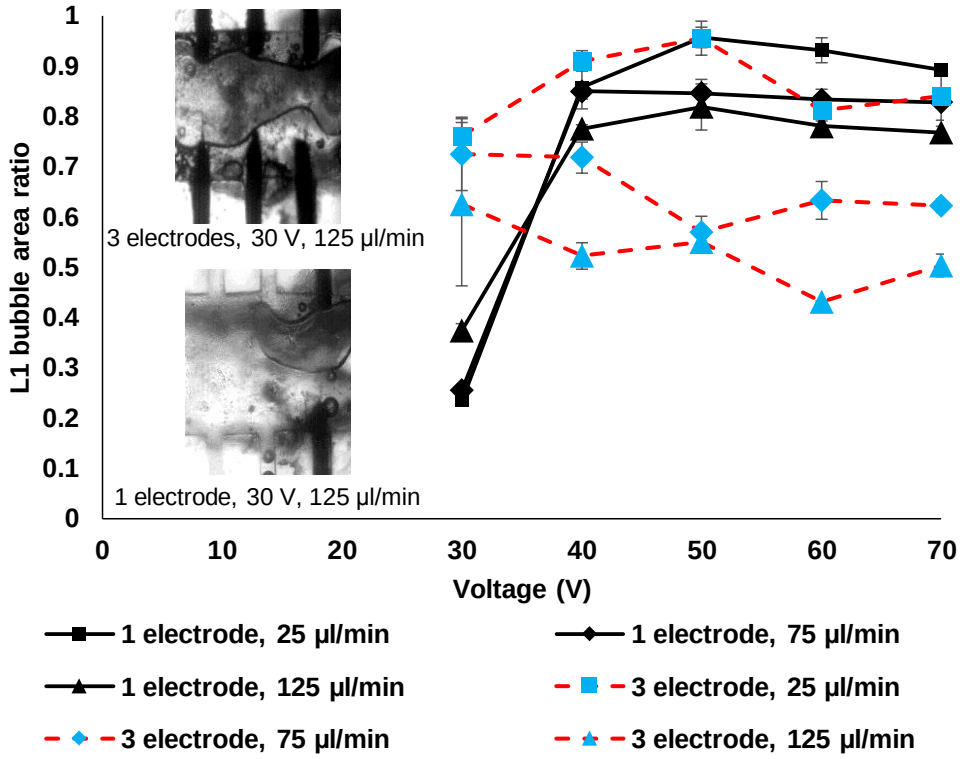

Figure 5.10 Influence of voltage towards L1 steady state area.

As the applied voltage was increased further to 50 *V* for 1 electrode pair case, the influence of applied voltage towards L1 bubble area ratio has reached its maximum. This shows that further increase in applied voltage does not contribute to higher decomposition efficiency, indicating that the decomposition efficiency is maximum upon reaching the critical voltage of 50 *V* for decomposition efficiency.

An interesting phenomenon was observed on the using of 3 pairs of electrodes in the decomposition of HAN solution. The additional pair of electrodes has positive effect on the decomposition at low applied voltage. The bubble area ratio for applied voltage of 30 *V* is approximately 0.65, which is 2.5 times higher than the case using 1 pair of electrodes, even at the highest flowrate of 125 *µl/min*. Nevertheless,

the increment in applied voltage do not benefit the completeness of decomposition of HAN.

For 3 pairs of electrodes, completeness of decomposition at 25 *µl/min* is higher than that of 75 and 125 *µl/min*. This was similar to the effect of flowrate, as discussed in Section 5.4, where increased flowrate resulted in dead volume formation in between electrodes, causing the low decomposition efficiency at both 75 and 125 *µl/min*.

From 40 *V* and above, the L1 bubble area ratio ranged from 0.76 – 0.95 and 0.43 – 0.95 for 1 and 3 pairs of electrodes, respectively. The number of small bubbles formed at electrodes increases at high applied voltage which interrupts further decomposition of HAN. In addition, the flowrate is identified as the more dominant factor than applied voltage for the complete decomposition of HAN. This is evidenced by the notably lower bubble area ratio at L1 section at high flowrate of 125 *µl/min* even though the applied voltage is at the highest of 70 *V*.

5.5.1 Copper anode degradation

In previous chapter, copper anode was shown to degrade during the electrolytic decomposition of HAN when employing copper electrodes, with the reaction Cu -> Cu^{2+} + $2e^{-}$. However, effect of degradation of copper was not carried out during our analysis.

As seen in Figure 5.7, the protrusions of copper anode in both 1 and 3 pairs of electrodes cases were degraded from cylinder shape

(original shape) for 25 *µl/min* to cone-shaped like (worst-case scenario) for 125 *µl/min*, as shown in Figure 5.11 Thus, the effect of the shape changing will be analyzed as below:

(A) (B)

Figure 5.11 Illustration of (A) cone shape and (B) cylinder shape.

For this, it is required to know that the surface area (S.A.) of the copper anode in contact with HAN. Equations for S.A. of both cone and cylinder were given by:

$$\text{S.A. for right circular cone} = \pi r\sqrt{(h^2 + r^2)} \qquad \text{E5-1}$$

$$\text{S.A. for cylinder} = 2\pi rh + \pi r^2 \qquad \text{E5-2}$$

As the copper wire diameter is 300 *µm* and the protrusion is 500 *µm*, the values were substituted into both E5-1 and E5-2 to obtain the ratio of S.A. of degraded copper anode over original copper anode, which was obtained to be 0.4540. As can be seen from the calculations, the surface area of copper anode decreased as it degraded. However, it was shown in Figure 5.8 that the applied voltage has positive influence towards overall reaction rate, in which the decreased surface area of copper anode did not affect the increase in overall reaction rate. Thus, the effect of copper degradation is not apparent in our study. Calculations of the ratio of S.A. of degraded copper anode over original copper anode were shown in Appendix I.

In this subsection, 40 *V* is concluded as the minimum voltage needed for complete sustained decomposition. The overall reaction rate is proportional to the applied voltage under each test condition. 3 electrode pair has higher overall reaction rate than that of 1 electrode pair. The bubble area ratio has a major difference at 30 *V* for different number of electrode pair.

Highest overall reaction rate (0.29 ± 0.03 mm^2/ms) was obtained with 3 pairs of electrodes, flowrate of 75 *µl/min* and applied voltage of 70 *V*. The delay in region (B) of Figure 5.3 could be reduced by improving the overall reaction rate, and thereby further reducing the overall delay, in hope to achieve a real-time micropropulsion system in usage of microsatellite.

5.5.2 Significance test of parameters affecting overall reaction rate

As seen in Figure 5.9, three parameters were varied to obtain the overall reaction rate, i.e. number of electrode pair, HAN flowrate and applied voltage. Both increase in number of electrode pair and applied voltage give proportional increase to overall reaction rate. However, the effect of flowrate is still unclear. Thus, a statistical test was performed on the data obtained to deduce which parameter gives the most impact towards the overall reaction rate.

A two-level full factorial design (2^3) was carried out to investigate the effects and interactions of important parameters in overall reaction rate of HAN decomposition in PDMS microreactors. Three independent parameters, including number of electrode pairs (A), HAN flowrate (B) and applied voltage (C) were taken into account and studied at two widely spaced levels. The low (-) and high (+) levels of the factors were 1 and 3 for number of electrode pairs, 25 and 125 *μl/min* for HAN flowrate, 30 and 70 *V* for applied voltage.

Utilizing a statistical software package (Design Expert, DX7, Stat-Ease, USA), the analysis of variance (ANOVA) was performed to verify the models validity, evaluate statistical significance of all factors and determine the influence of these factors on the response variables. The model consisted of three main effects, three two-parameter interactions, and one three-parameter interaction. The full statistical results for response variable “Overall reaction rate” are shown in Table 5.2.

Table 5.2 Results of the ANOVA analysis on the factors affecting overall reaction rate.

Source of variation	Sum of squares	Degree of freedom	Mean square	F value	p-value
Model	0.24	5	0.048	191.71	<0.0001
A	0.054	1	0.054	216.15	<0.0001
B	0.001867	1	0.001867	7.49	0.0136
C	0.14	1	0.14	576.93	<0.0001
AC	0.038	1	0.038	151.32	<0.0001
BC	0.001658	1	0.001658	6.65	0.0189
Residual	0.00490	18	0.0002494		
R^2	0.9816	Adj R^2	0.9764	Pred R^2	0.9672

According to the results, the f-value of 191.71 with low probability value (p-value < 0.0001) indicates that the overall regression model was significant with 95 % of confidence. The values of the coefficient of determination (R^2) and adjusted R^2 can be utilized to assess the ratio of total variation ascribed to each fit and measure the accuracy of the model for the response variable, respectively. High R^2 of 0.9816 demonstrates a good response between the model and the experimental results. The adjusted R^2 of 0.9764 and predicted R^2 of 0.9762, show the predicted values are compatible with the experimental results.

p-values of less than 0.05 indicates that the model terms are statistically significant model terms, while values larger than 0.10 show that those are insignificant model terms. For overall reaction rate, the regression analysis of the experimental results have indicated that the linear model terms (A, B and C) and interactive model term (AC and BC) are the significant model terms. By using only significant model terms, the new model was attained for response variable “Overall reaction rate”. Using ANOVA, the statistical analysis demonstrated that the model was significant at a confidence level of 95 %. By taking into account of the significant linear model terms and interactions, the regression analysis of Overall reaction rate data provided the following first-order model, as shown in E5-3:

Overall reaction rate = 0.092 + 0.047A - 0.008821B + 0.077C + 0.04AC - 0.008312BC	E5-3

Generally, the contribution of the model terms to the response variables can be evaluated using the degree of corresponding coefficients of the linear regression equations. From the regression equation, it can be observed that the applied voltage (C) has the strongest positive effect on overall reaction rate.

5.6 Performance comparison with HAN ternary mixture

With the optimized parameters obtained from Section 5.2 to 5.4, it was finalized that highest reaction rate of HAN solution was obtained by

using 3 electrodes, with applied voltage of 70 *V* and flowrate of 75 *µl/min*. With the aim of understanding on electrolytic decomposition of HAN ternary mixture further in microscale, HAN-dextrose was selected based on the highest $\dot{T}_1$ result, which was obtained in macroscale electrolytic decomposition experiment that was conducted in Chapter 3. $\dot{T}_1$ of HAN-dextrose is the closest to that of binary HAN, among all the HAN ternary mixture tested, showing that they have closest performance before boiling point of water during electrolysis stage.

Table 5.3 Optimized parameters on microscale experiment of HAN-dextrose.

Number of electrode pairs	3
Applied voltage (V)	70
Flowrate (µl/min)	25

Electrolytic decomposition of HAN-dextrose was performed with this set of optimized parameters, as stated in Table 5.3. The flowrate of highest overall reaction rate was 75 *µl/min* but was adjusted to 25 *µl/min*, as complete decomposition and higher overall efficiency were achieved with flowrate of 25 *µl/min*. The overall reaction rate and L1 bubble area ratio of HAN solution and HAN-dextrose were shown in Figure 5.12.

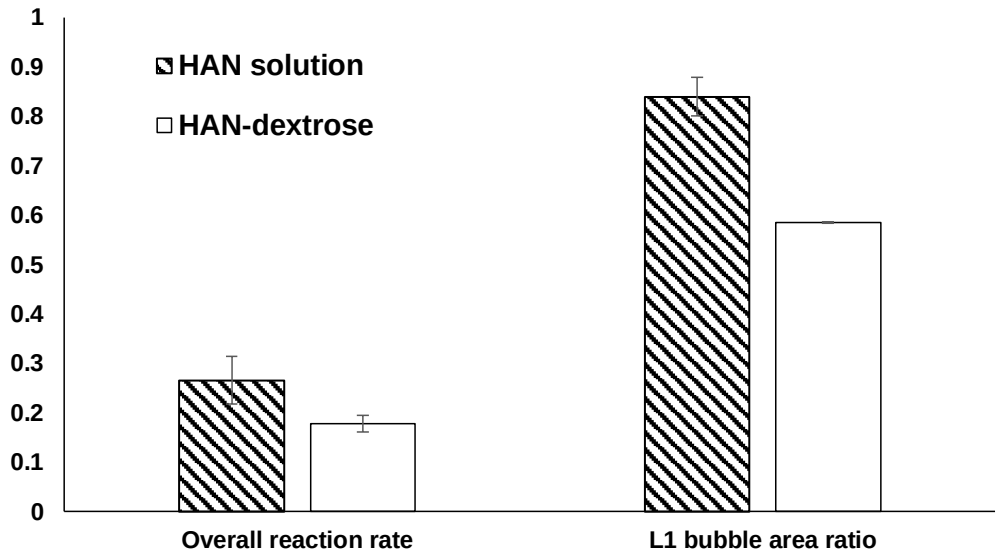

Figure 5.12 Performance comparison between HAN solution and HAN-dextrose.

Overall reaction rate and L1 bubble area ratio could be compared to $\dot{T}_1$ and T_{max} in Section 3.3.2 and 3.3.3, respectively. Higher overall reaction rate of HAN solution, as compared to HAN-dextrose, indicated that HAN solution decomposed at a higher rate in the absence of dextrose.

As highlighted in Chapter 3 on the effect of resistivity on $\dot{T}_1$, it was shown that higher mixture resistivity led to higher $\dot{T}_1$, in this case, higher overall reaction rate. However, lower overall reaction rate was observed in HAN-dextrose case, despite having higher mixture resistivity (0.1609 $\mu\Omega.m$), as compared to 73 wt% HAN solution (0.0779 $\mu\Omega.m$). It was discussed in Section 3.3.3 that fuels absorb thermal energy from decomposition of HAN, causing the overall reaction rate of HAN-dextrose to be lower than that of binary HAN. This indicates that effect of fuel

towards reaction rate is more dominant than mixture resistivity in this case.

As indicated in Figure 5.12, the L1 bubble area ratio of HAN-dextrose is lower than that of HAN, which was also shown by lower T_{max} of HAN-dextrose than HAN solution. This was complemented by the duration required for dextrose to absorb energy released from HAN decomposition in Section 3.3.3.3. As opposed to the fixed volume of liquid propellant used in the calorimetric study, flowing HAN-dextrose caused the decomposition to be partially complete. Moreover, energy released from the decomposition of HAN component was deposited to HAN solution, as opposed to, absorbed by dextrose, in order to enter the next stage of decomposition, as discussed in Section 3.3.3.3.

5.7 Effect of electrolytic decomposition on PDMS microreactor structure

From Section 5.2 to 5.6, PDMS microreactors were shown to sustain the decomposition. However, the effect of electrolytic decomposition on PDMS structure remained unclear. After decomposition, the PDMS microreactors were examined under scanning electron microscope (SEM) to determine the effect of decomposition on the structure of PDMS microreactor. They were also examined under energy-dispersive X-ray spectroscopy (EDX) to determine the components change on the surface.

PDMS is known to be a chemically inert and electrically insulating material, and thus suitable to be structural material in this study [174]. However, structural change in PDMS structure was observed on the PDMS surface. Inlet of PDMS device was connected to syringe pump and the other end was open to atmospheric pressure.

In Figure 5.13A, it was shown that PDMS structure suffered from damage after decomposition (AII), as compared to the PDMS structure before decomposition (AI). The red and blue circle in Figure 5.13A refers to the cathodes and anodes. Figure 5.13B and Figure 5.13C show the PDMS structure before (I) and after (II) decomposition at 1000x magnification of the red and blue circle region in Figure 5.13A, respectively. Irregular holes and cracks were noticed in zoomed section of the both circled region. It could be observed that the depth of the cracks in Figure 5.13BII is greater than that in Figure 5.13CII, while the width of the cracks is larger in Figure 5.13BII (432 – 865 *μm*) and Figure 5.13CII (298 – 382 *μm*). It showed that reaction at cathode is more vigorous than anode.

No work has reported usage of PDMS microreactor for micropropulsion purpose. A study showed that cracks on microthruster could result in longer ignition delay and lower thrust, which is undesirable in micropropulsion purpose [117]. PDMS was shown to sustain the decomposition throughout the study, showing that the impact towards the structural properties is insignificant. However, deteriorations of structural

properties should be taken into consideration during microreactor design if PDMS was used as structural material for microcombustion chamber.

When HAN was decomposed, the gaseous species were evolved in all directions, impacting the PDMS microreactor surface. High reaction rate of energetic reaction, coupled with heat released from HAN decomposition and low pH nature of HAN solution, caused the structural changes on PDMS microreactor surface, turning the smooth surface to a cracked surface.

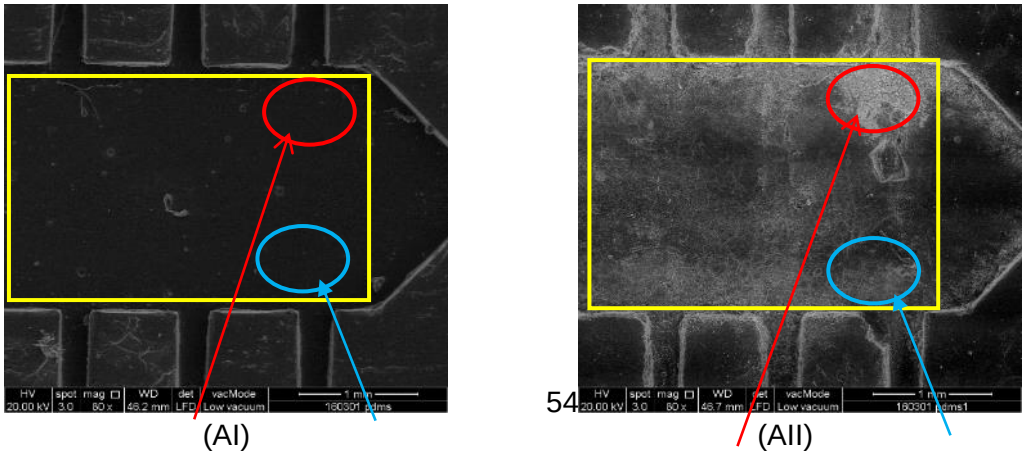

(AI) (AII)

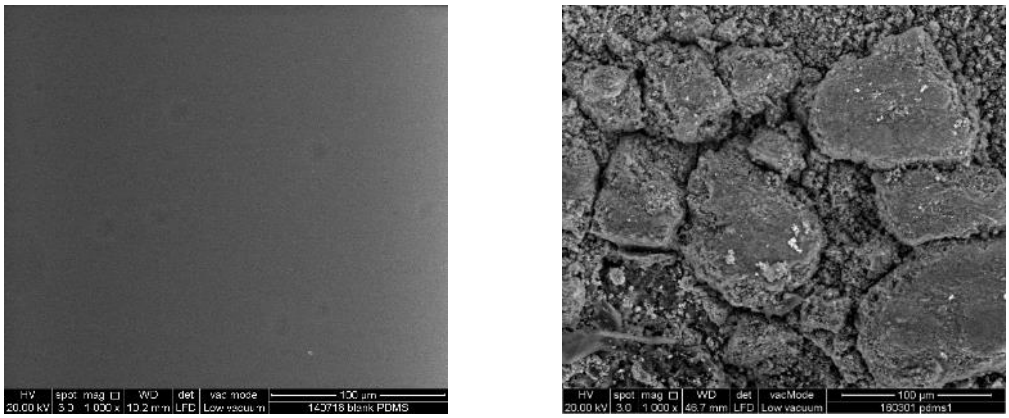

(BI) (BII)

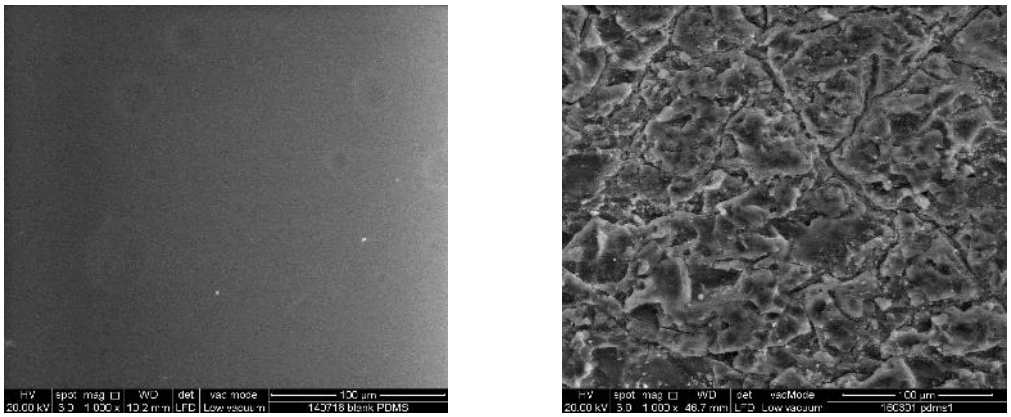

(CI) (CII)

Figure 5.13 PDMS structure (I) before and (II) after decomposition at (A) 80x, (B) 1000x at cathode side and (C) 1000x magnification at anode side under SEM.

Results in Figure 5.14 refer to EDX analysis on PDMS microreactor surface (yellow rectangle part Figure 5.13A) before and

after decomposition. Presences of N and O after the decomposition were attributed from HAN leftover, led by decomposition of HAN on surface of PDMS microreactor. As HAN is a strong oxidizer, the decomposition of HAN caused the inert PDMS to oxidize and thus led to the increase in oxygen content. PDMS has chemical formula of $(C_2H_6OSi)_n$, as shown in Figure 5.15, with C atomic percentage double than that of Si and C atomic percentage is 1.5 times than that of O. Atomic percentage of oxygen is slightly larger than the theoretical value, where C atomic percentage should be 2 times than that of O.

As compared to the blank sample, presence of Cu after decomposition indicated leftover of decomposed copper on surface. In addition, presence of Cl most likely attributed to trace amount of Cl present in the copper electrode and only will be revealed after decomposition, as shown in Figure 5.18B.

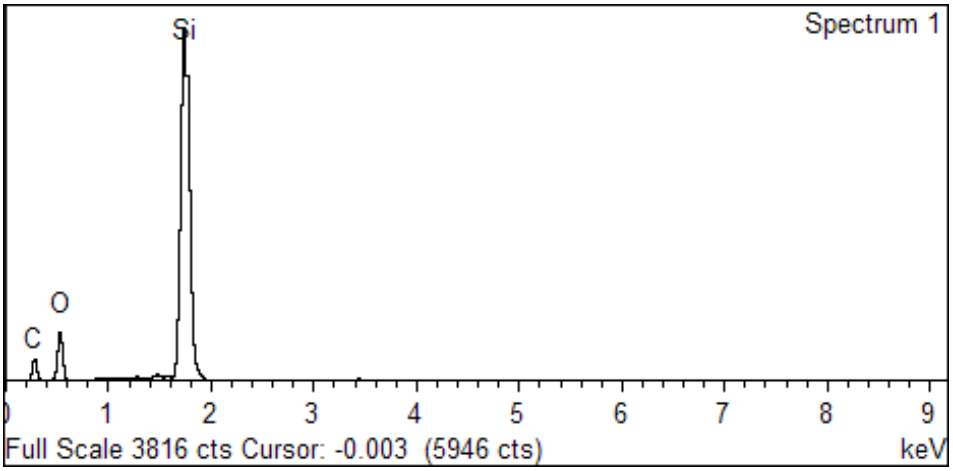

(A)

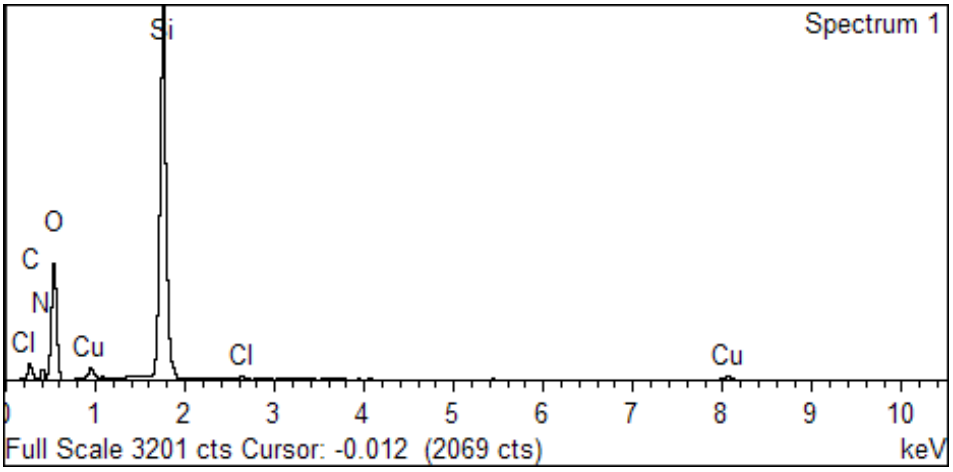

(B)

Figure 5.14 EDX analysis on PDMS chamber (A) before and (B) after decomposition.

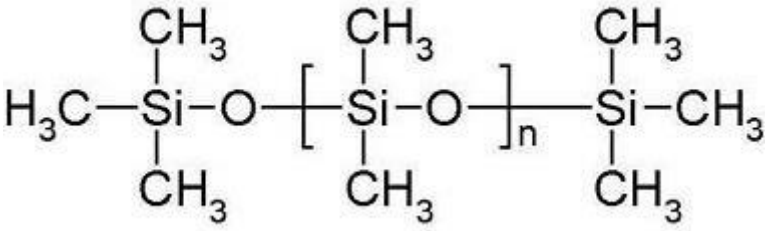

Figure 5.15 PDMS chemical structure.

Effect of decomposition towards chamber wall on anode and cathode was shown in Figure 5.16. As mentioned in Section 3.3.1, electrolysis of HAN solution produced more gaseous species on the cathodes [117]. In addition, the first pair of electrodes in three electrode pair PDMS microreactor have higher frequency of contact with HAN solution, causing the reaction to be more vigorous towards chamber inlet and on the cathode side.

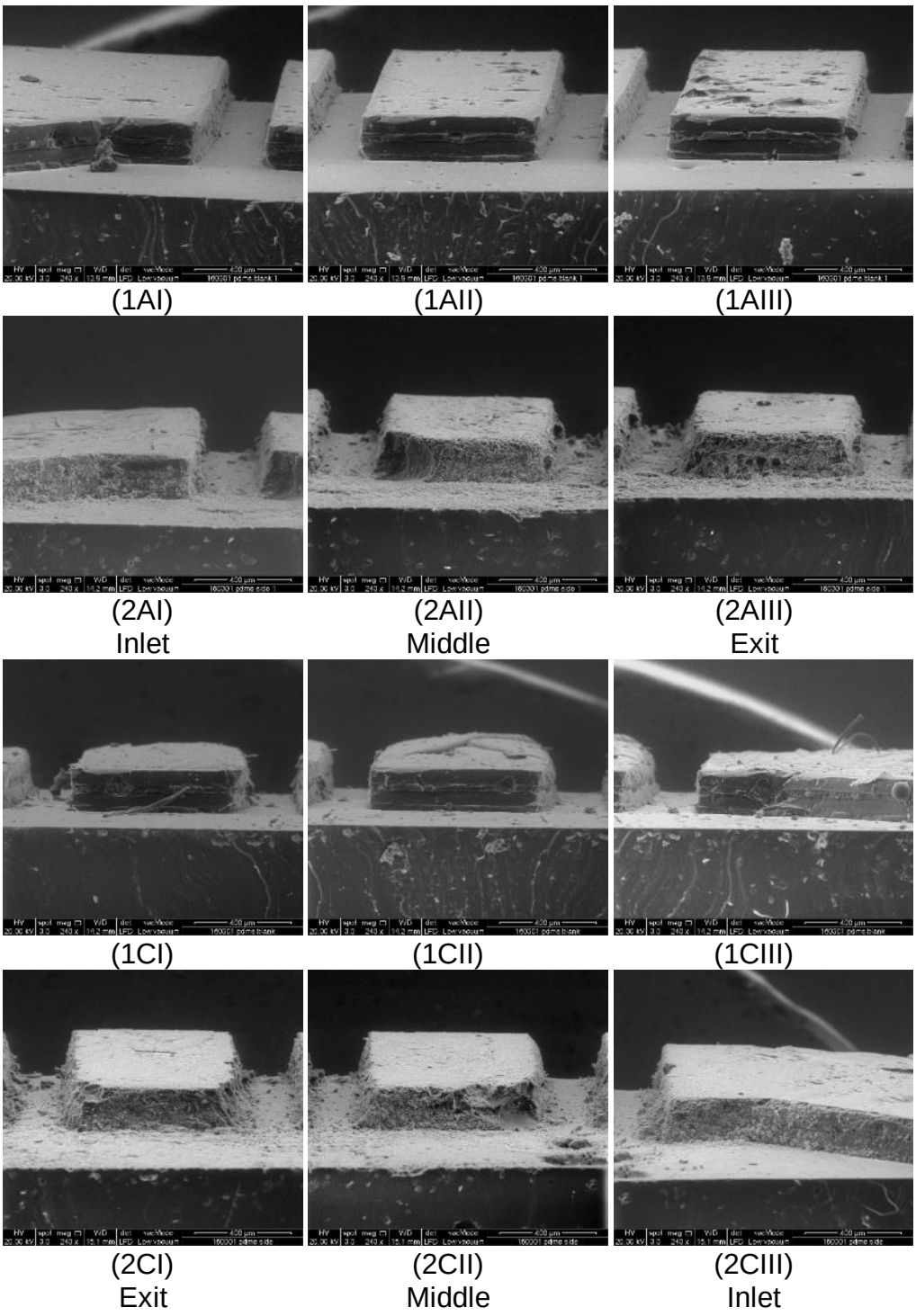

Figure 5.16 Comparison images of (1) before and (2) after decomposition at (A) positive anode electrode side and (C) negative cathode electrode side from (I) exit to (III) inlet.

Figure 5.17 presents the SEM image of copper anode before and after decomposition at 100x and 1000x magnification while Figure 5.18 shows EDX analysis of copper anode before and after decomposition. The smooth surface of copper electrode, as observed in Figure 5.17A, was oxidized and corroded, leading to thinning of copper electrode and appearance of corroded surface in Figure 5.17B. From Figure 5.18A and B, large amount of O indicated that the electrode was heavily oxidized. The presence of traces of chlorine might be due to the use of distilled water in diluting nitric acid for HAN synthesis.

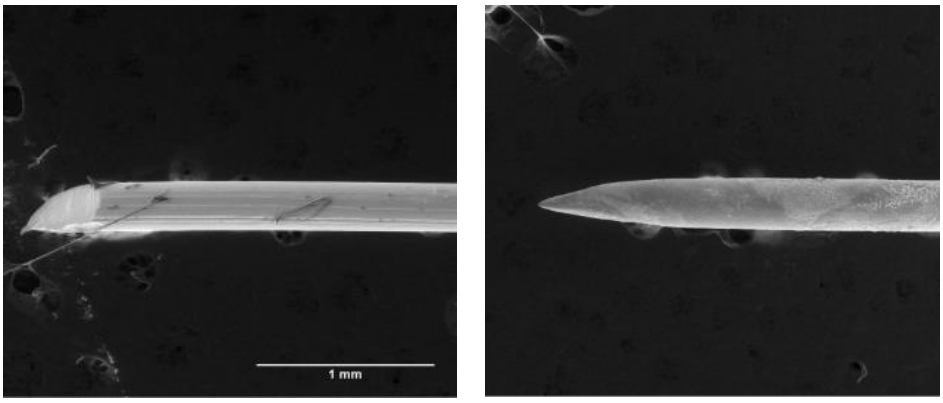

(AI) (AII)

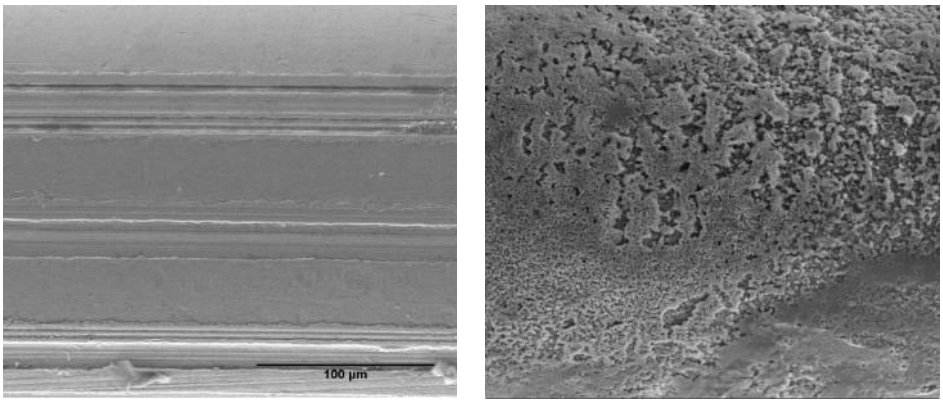

(BI) (BII)

Figure 5.17 Comparison of SEM images on copper anode structure (I) before and (II) after decomposition at (A) 100x and (B) 1000x magnification.

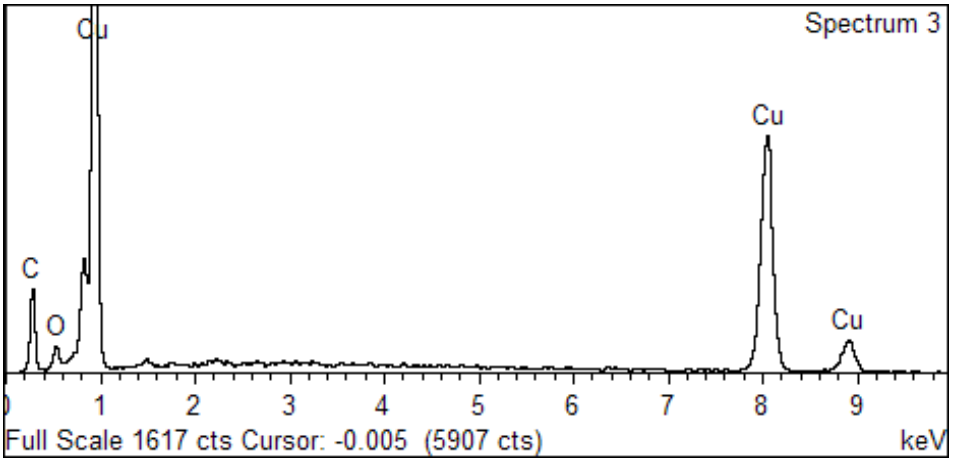

(A)

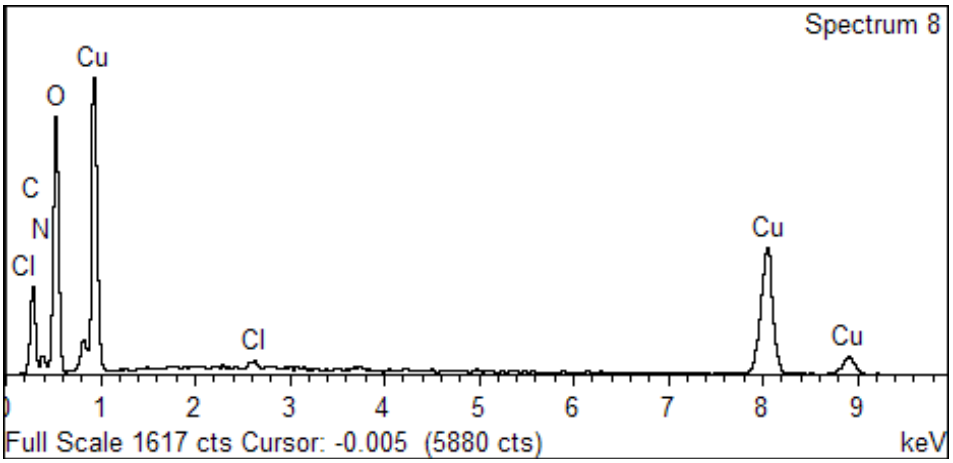

(B)

Figure 5.18 EDX analysis on copper anode (A) before and (B) after decomposition.

5.8 Summary

In this study, the electrolytic decomposition of HAN solution in microscale was investigated by analyzing the change in bubble area inside the reaction chamber in microreactor. Parameter optimization study on HAN decomposition was also carried out in this study. Usage of 3 pairs of electrodes has shortened the ignition delay of HAN solution and the time taken for the reaction to achieve steady state. The additional pairs of electrode provide more activation site for decomposition of in-

flowing HAN solution. As such, the increase in overall reaction rate is as high as 225 % when using the 3 pairs of electrodes.

In general, the overall reaction rate increases with the flowrate. However, a drop in overall reaction rate and incomplete decomposition was observed after optimum flowrate. This implies that a sufficient residence time is required for the decomposition to occur. Subsequent parametric study shows that overall reaction rate is proportional to the applied voltage. Using of 3 pairs of electrodes has initiated the decomposition of HAN solution even in the low applied voltage regime. Based on the parametric study done on 3 parameters, the highest reaction rate of 0.29 mm^2/ms can be achieved by using 3 electrodes, with applied voltage of 70 V and flowrate of 75 $\mu l/min$.

A statistical analysis was conducted on the experimental results obtained. All three parameters were significant towards the overall reaction rate. The significance of three parameters were arranged in descending order: applied voltage, number of electrode pair and flowrates. Applied voltage has the strongest positive effect on overall reaction rate in electrolytic decomposition of HAN in PDMS microreactor.

Based on the optimized parameters obtained on HAN, electrolytic decomposition of HAN-dextrose was carried out in microreactor. As noted by effect of fuel addition in Chapter 3, both overall reaction rate and L1 bubble area ratio were also lower than that of HAN solution. SEM and EDX morphological tests were also carried out on the microreactor

before and after decomposition. The results showed that PDMS microreactor was able sustain the decomposition.

Chapter 6 Conclusion and future work

6.1 Conclusions

The entire work is focused on characterization of low power electrolytic decomposition performance of hydroxylammonium nitrate (HAN) solution and ternary mixture at microscale and macroscale, respectively.

HAN ternary mixture was of interest, because addition of fuel has higher energy density. Three classes of fuels were selected for analysis: alcohols, saccharides and nitrogen-rich compound. As zero oxygen balance mixture (OB) has the highest theoretical potential energy, thus a zero OB HAN ternary mixture was prepared and subjected to electrolytic decomposition at macroscale. Results showed that the overall decomposition was split into two main stages. First stage took place once the electrolytic decomposition was initiated, until the solution temperature raised to 100 °C, while the second stage occurred after boiling point of water. Most of the decomposition pattern of ternary mixtures have two stages.

Due to nature of electrolytic decomposition, effect of electrochemical properties of HAN mixtures, i.e. electrical resistivity, towards decomposition performance was investigated. The resistivity of HAN ternary mixtures was found to be linearly proportional with rate of temperature rise, $\dot{T}_1$, before boiling point of water. The linear correlation

between resistivity and rate of temperature rise, $\dot{T}_1 = 48.006\rho_M$, showed that Joule heating is present during the electrolysis stage.

Effect of fuel addition to HAN solution towards decomposition performance was not fully understood, thus chemical interaction of HAN ternary mixture was studied. Results revealed that chemical interaction of HAN and fuel does have direct relationship with maximum temperature achieved, T_{max}.

Alcohols and saccharides are molecular fuels, while nitrogen-rich compounds behaved ionically when subjected to electrolytic decomposition. T_{max} of alcohols and saccharides are affected by their respective thermal energy released upon combustion within their own family. Both alcohols and nitrogen-rich compounds have two stages of decomposition, while saccharides have three. Additional stage of decomposition in saccharides released heat for a longer period of time. Ionic behavior of nitrogen-rich compounds cause them to have highest average T_{max} of all families.

The study was followed by detailed description of visualization setup for capturing decomposition phenomena of electrolytic decomposition of HAN solution. Double pole single throw (DPST) switch was integrated into the high speed visualization setup to trigger the high speed camera. Feasibility of DPST switch integration was discussed and compared with image-based auto trigger method, which showed the maximum delay of triggering high speed camera using DPST switch is 4 *ms*. Low price and short delay of DPST switch, coupled with its feasibility

to perform the triggering, greatly reduced the cost of employing DAQ system. In order to further understand the decomposition phenomena of HAN solution and to tackle the ceramic microthruster cracking issue, experiments including the effect of number of electrode pair, HAN flowrate and applied voltage were performed.

Quantitative analysis, using image analysis technique, was carried out on bubble growth during electrolytic decomposition of HAN solution. Overall reaction rate was defined as rate of bubble area growth. Higher overall reaction rate implies shorter delay before decomposition reaching steady state, improving towards realization of real-time HAN decomposition in microsatellite.

In general, all three parameters: number of electrode pair, HAN flowrate and applied voltage have positive influence towards overall reaction rate. The ignition delay and time taken for the reaction to achieve steady state was shortened using 3 pairs of electrodes, as compared to 1 pair of electrodes. It was due to more reaction sites of electrode available for decomposition of in-flowing HAN solution when the additional pairs of electrode were present.

Further increase in flowrate causes decrease in overall reaction rate and incomplete decomposition. This implies that sufficient residence time is required for decomposition to occur continuously. Optimum flowrate of maximum overall reaction rate using 3 electrode pair (50 *μl/min*) is lower than that of 1 electrode pair (100 *μl/min*) due to smaller area for reaction. It should also be ensured that HAN solution and

electrodes are in contact frequently for the decomposition to occur continuously.

Although decomposition efficiency of 3 electrode pair might be lower than that of 1 electrode pair at high flowrate (> 75 *µl/min*), it was able to initiate the decomposition of HAN even at the lowest applied voltage (30 *V*). The decomposition efficiency for 1 electrode pair increased the most when the applied voltage was increased from 30 to 40 *V*. This implies that 30 *V* is the applied voltage threshold for 1 electrode pair.

Results above could be optimized to determine an optimal setting for desired operation on microthruster. Highest reaction rate of 0.29 mm^2/ms was obtained by using 3 electrode pair, applied voltage of 70 *V* and flowrate of 75 *µl/min*. Optimized parameters from decomposing HAN solution were then compared with HAN-dextrose, a HAN ternary mixture selected based on highest $\dot{T}_1$. Performance of HAN solution, in terms of overall reaction rate and L1 bubble area ratio, were higher than that of HAN-dextrose, due to energy absorbed by dextrose from the heat released from decomposition of HAN component. According to SEM and EDX results on on PDMS microreactors before and after the decomposition, despite PDMS microreactors suffered from minor surface damage, PDMS microreactors was able to sustain the decomposition.

For selection of mixture, my suggestion would be the fuel which can produce additional electrons, such as HAN-urea. For electrolytic

ignition conditions,I would suggest to use high applied voltage, electrode with larger surface area and suitable HAN-fuel flowrate.

6.2 Recommendations for Future Work

Limitations of existing work were mentioned throughout the work. Recommendations are outlined as below for improvement in the future:

- **Technical improvements**

1. Evolvement of heat during current HAN synthesis method possesses an issue as ammonium nitrate will be produced at elevated temperature instead of hydroxylammonium nitrate. Laboratory scale HAN synthesizer with proper control over temperature and flowrate could be developed as final HAN concentration and yield could be controlled properly.

2. Pressurized chamber could be used to verify influence of boiling point of water on electrolytic decomposition. Electrolytic decomposition could be more effective at higher pressure as higher chamber pressure resulted in higher boiling point of water. Although pressurized chamber was used commonly in combustion studies, handling such system still face challenges if the user is not experienced.

3. Effect of power supply cutoff interval should be studied to optimize the decomposition process and enhance its efficiency. More energy could be saved by applying the cutoff.

4. Effect of other electrochemical properties of HAN mixtures can be further studied towards performance of electrolytic decomposition of

HAN mixtures. A more rigorous method could be devised to characterize the decomposition process more properly.

5. Embedding micro temperature and pressure sensors into the microreactor, enables temperature and pressure profile during decomposition to be measured. But, such system will require a proper DAQ system, which will add cost to the entire experimental setup

6. In this study, the phenomena of HAN decomposition was studied using point ignition method. It showed good demonstration of decomposing HAN by using copper electrodes. However, the point ignition method was particularly hindered by the influence of HAN flowrate. Using new fabrication route, the electrodes placement could be carried out more accurately. Screen printing electrodes on reactor chamber should be considered, with emerging of screen printing technology.

7. Heat loss in chemical microthrusters was proved to be a significant issue when thermal decomposition and catalytic decomposition technique were employed. Thermal conductivity and mechanical properties of ceramic-based material could be improved to overcome the heat loss and cracking issue.

8. Experiments performed in the microreactor could be repeated with other HAN ternary mixtures studied at macroscale level. Visualization of HAN ternary mixtures could be done to verify the performance of such mixtures.

- **Recommendations**

1. Numerical modelling has been carried out on electrolytic decomposition of HAN binary solution. However, chemical interaction between HAN and fuel was still not fully understood. Numerical simulations and respective theories on HAN-fuel decomposition should be determined in order to understand the decomposition kinetics further.

2. Reaction kinetics on LP 1846 was studied but no other HAN-fuel ternary mixtures. Decomposition should be further studied, as a fundamental study to extend the understanding of decomposition of other HAN-fuel ternary mixtures.

3. HAN decomposition was conducted at atmospheric pressure. Further studying the HAN decomposition in vacuum conditions, making it one step closer in realizing the potential of HAN usage in outer space.

4. Addition of a catalytic reactor after the electrolytic decomposition chamber to increase decomposition efficiency. Further improving the decomposition efficiency could lead to a more efficient microthruster.

5. Embedding of micro-temperature sensors into the microreactor and study the temperature mapping, together with HAN modelling, in order to further study HAN decomposition.

APPENDIX 1

Table 1 TGA results of HAN weight percentage

Trial	HAN concentration (wt%)
1	73.86
2	73.74
3	70.72
Average	72.77
Standard deviation (%)	2.45

Oxygen balance calculation

For 73 wt% HAN solution (33.3 OB%) and methanol (-149.83 OB%), mass of methanol required to be added to 5 *g* of 73 *wt%* HAN solution

= (mass of HAN solution x OB% of HAN solution / OB% of methanol)

= (5 g x 0.73 x 33.3% / -149.83 %)

= 0.8112 g (4 s.f.)

Calculations of area under curve, which represents the average temperature in the particular time region

Area under curve could be evaluated using trapezoidal rule

Taking HAN-Propanol as an example, from t = 2 s to t = 3 s, temperature for HAN-Propanol increases from 28.3 °C to 33.43 °C,

Area under curve from t = 2 s to t = 3 s

= 0.5 x (3-2) s x (28.3 + 33.43) °C

= 30.8650 °C s (4 s.f.)

Total area under curve

= sum of area under curve from t= 2 s to t = 47 s

= 4895.5167 °C s (4 s.f.)

Average temperature for the entire decomposition of HAN-Propanol

= Total area under curve / Total time taken

= 4895.5167 °C s/ (47-2) s

= 108.7893 °C

Calculations of heat of vaporization required for complete vaporization of methanol in HAN-methanol ternary mixture

Total heat of vaporization required for vaporization of methanol

= m x Hvap

= 0.81 g x 38.278 kJ/mol / 32.04 g/mol

= 0.9677 kJ (4 s.f.)

Calculations of heat of combustion resulted in decomposition of methanol in HAN-Methanol ternary mixture

Total heat released resulted from combustion of methanol

= mass of methanol x heat of combustion of methanol

= 0.81 g / 32.04 g/mol x -715 kJ/mol

= -18.08 kJ (4 s.f.)

Calculations of heat of reaction resulted in decomposition of HAN-Dextrose

$C_6H_{14}O_7$ -> 6C + 7 H_2O

Heat of reaction resulted in decomposition of HAN-dextrose

= $\sum H_{f,products} - \sum H_{f,reactants}$

= ∑ (Product coefficient x Heat capacity of product) - ∑ (Reactant coefficient x Heat capacity of reactant)

= (6 x -373 kJ/mol + 7 x -285.8 kJ/mol) – (1 x -2221 kJ/mol)

= -2655.62 kJ/mol

= -2655.62 kJ/mol x mass of dextrose/molecular weight of dextrose

= -2655.62 kJ/mol x 1.26 g / 198.2 g/mol

= -16.88 kJ (4 s.f.)

Table 2 Result of electrical resistivity measurement of ternary mixture.

Fuel in HAN ternary mixture	Electrical resistivity (μΩ.m)				Standard deviation (%)
	Trial 1	Trial 2	Trial 3	Average	
Methanol	0.0857	0.0859	0.0858	0.0858	0.1310
Propanol	0.0914	0.0916	0.0910	0.0913	0.3289
Dextrose	0.1623	0.1611	0.1594	0.1609	0.8960
Sucrose	0.1360	0.1359	0.1363	0.1361	0.1364
Urea	0.1453	0.1452	0.1455	0.1453	0.1051
Ammonia	0.0389	0.0392	0.0381	0.0387	1.4680

Residence time calculation

Chamber volume calculation

= chamber width x chamber height x chamber depth

= 2 mm x 12 mm x 180 μm

= 0.002 m x 0.012 m x 0.0018 m

= 4.32×10^{-9} m^3

Residence time for flowrate of 125 μl/min

= Chamber volume / Volumetric flowrate

= 4.32×10^{-9} m^3 / 125 μl/min x 1/60 min/s x 1/1000000000 m^3/μl

= 2.074 s (4 s.f.)

Ratio of surface area of degraded copper anode over original copper anode calculation

Ratio of S.A. of degraded copper anode over original copper anode

$= (\pi r\sqrt{(h^2 + r^2)})/(2\pi rh + \pi r^2)$

$= \sqrt{(h^2 + r^2)})/(2h + r)$

$= \sqrt{(0.0005^2 + 0.00015^2)}/(2 \times 0.0005 + 0.00015)$

= 0.4540 (4 s.f.)

References

[1] DePasquale, D. and J. Bradford. *Nano/Microsatellite Market Assessment 2013*. 2013 [cited 2013 2nd Novemeber 2013]; Available from: http://www.spaceworksforecast.com/docs/SpaceWorks_Nano_Microsatellite_Market_Assessment_2013.pdf.

[2] Buchen, E. and D. DePasquale. *2014 Nano/Microsatellite Market Assessment*. 2014 [cited 2015 9th Novemeber 2015]; Available from: http://www.sei.aero/eng/papers/uploads/archive/SpaceWorks_Nano_Microsatellite_Market_Assessment_January_2014.pdf.

[3] Janson, S., *25 Years of Small Satellites*. 2011, The Aerospace Corporation.

[4] Obland, M., et al. *The Montana State University NASA Space Grant Explorer-1 Science Reflight Commemorative Mission*. in *15th Annual AIAA/USU Conference on Small Satellites*. 2001.

[5] Micci, M.M. and A.D. Ketsdever, *Micropropulsion for Small Spacecraft, Volume 187 of Progress in Astronautics and Aeronautics*. 2000: American Institute of Aeronautics and Astronautics.

[6] Jankovsky, R.S., *HAN-Based Monopropellant Assessment for Spacecraft*, in *32nd AIAA/ASME/SAE/ASEE Joint Propulsion Conference*. 1996, American Institute of Aeronautics and Astronautics: Lake Buena Vista, FL, USA. p. 2863/1-2863/9.

[7] Shea, H.R. *MEMS for pico- to micro-satellites*. in *MOEMS and Miniaturized Systems VIII* 2009. San Jose, CA.

[8] Epstein, A.H., *Millimeter-scale, micro-electro-mechanical systems gas turbine engines.* Journal of Engineering for Gas Turbines and Power, 2004. **126**(2): p. 205-226.

[9] Kaisare, N.S. and D.G. Vlachos, *A review on microcombustion: Fundamentals, devices and applications.* Progress in Energy and Combustion Science, 2012. **38**(3): p. 321-359.

[10] Izquierdo, U., et al., *Hydrogen production from methane and natural gas steam reforming in conventional and microreactor reaction systems.* International Journal of Hydrogen Energy, 2012. **37**(8): p. 7026-7033.

[11] Fahrat, K., et al., *Application of Ionic Liquids to Space Propulsion*, in *Application of Ionic Liquids in Science and Technology*, S. Handy, Editor. 2011. p. 447-466.

[12] Meinhardt, D., et al., *Performance and Life Testing of Small HAN Thrusters*, in *35th Joint Propulsion Conference and Exhibit*. 1999, American Institute of Aeronautics and Astronautics: Los Angeles, CA. p. 2881/1-2881/12.

[13] T.W. Hawkins, A.J.B., M.B. McKay, M. Tinnirello (AFRL/RZSP), *Reduced Toxicity, High Performance Monopropellant at the U.S. Air Force Research Laboratory*, in *4th International Association for the Advancement of Space Safety Conference*. 2010: Huntsville, AL.

[14] Koh, K.S., *Synthesis, Characterization of Hydroxylammonium Nitrate (HAN) Solution and Its Low Power Electrolytic Decomposition in Microcombustion Chamber*, in *Department of Chemical and Environmental Engineering*. 2013, University of Nottingham.

[15] Hua, J., M. Wu, and X. Shan, *Studies on Combustion Characteristics in Micro-Combustor and Its Applications*, in *Chemical Engineering Research Trends*, L.P. Burton, Editor. 2007, Nova Science Publishers: New York. p. 1-70.

[16] Wucherer, E.J., S. Christofferson, and B. Reed, *Assessment of High Performance HAN-monopropellants*, in *36th AIAA/ASME/SAE/ASEE Joint Propulsion Conference*. 2000, American Institute of Aeronautics and Astronautics: Hunsville, AL, U.S. p. 3872/1-3872/9.

[17] Eloirdi, R., et al., *Design and use of a batch reactor for catalytic decomposition of propellants.* Journal of Propulsion and Power, 2003. **19**(2): p. 213-219.

[18] Katsumi, T., et al., *Combustion Characteristics of a Hydroxylammonium Nitrate Based Liquid Propellant. Combustion Mechanism and Application to Thrusters.* Combustion, Explosion and Shock Waves, 2009. **45**(4): p. 442-453.

[19] Fukuchi, B., et al., *HAN/HN-Based Monopropellant Thrusters.* IHI Engineering Review, 2010. **43**(1): p. 22-28.

[20] Zhang, K.L., S.K. Chou, and S.S. Ang, *Development of a low-temperature co-fired ceramic solid propellant microthruster.* Journal of Micromechanics and Microengineering, 2005. **15**(5): p. 944.

[21] Zhu, D., et al., *Thermal Conductivity of Ceramic Thermal Barrier and Environmental Barrier Coating Materials*. 2001, NASA Glenn Research Center. p. 1-21.

[22] Wu, M.-H., R.A. Yetter, and V. Yang, *Development and Characterization of Ceramic Micro Chemical Propulsion and Combustion Systems*, in *46th AIAA Aerospace Sciences Meeting and Exhibit*. 2008, American Institute of Aeronautics and Astronautics: Reno, NV. p. 12076-12088.

[23] Tsai, T.-H., et al., *Effect of viscosity of base fluid on thermal conductivity of nanofluids.* Applied Physics Letters, 2008. **93**(23): p. 233121/1-233121/3.

[24] Freedman, E., *A Survey of the thermodynamics of HAN-based liquid gun propellants*. 1980, DTIC Document.

[25] Kaufman, J.J. and W.S. Koski, *Study of the Hydroxylammonium Nitrate - Isopropyl Ammonium Nitrate Reaction.* 1980, DTIC Document.

[26] Comer, R.H., *Ignition and Combustion of Liquid Monopropellants at High Pressures.* Symposium (International) on Combustion, 1977. **16**(1): p. 1211-1219.

[27] Klingenberg, G., et al., *Liquid Propellant Gun Technology*. Progress in Astronautics and Aeronautics Series, V-175, AIAA (American Institute of Aeronautics & Astronautics). 1997, Reston, Virginia, USA: American Institute of Aeronautics and Astronautics.

[28] Kappenstein, C.J., et al., *Propulsion and catalysis - Historical survey, up-to-date overview, and current challenges.* International Journal of Energetic Materials and Chemical Propulsion, 2010. **9**(5): p. 413-436.

[29] Kappenstein, C., et al. *Non toxic ionic liquids as hydrazine substitutes. Comparison of physico-chemical properties and evaluation of ADN and HAN*. in *2nd International Conference on Green Propellants for Space Propulsion*. 2004. Cagliari, Sardinia, Italy.

[30] Courthéoux, L., et al., *Thermal and Catalytic Decomposition of HNF and HAN Liquid Ionic as Propellants.* Applied Catalysis B: Environmental, 2006. **62**(3-4): p. 217-225.

[31] Dragomir, O.-E., *Experimental investigation on hydrazinium nitroformate (HNF) combustion and its modification*. 2009, Delft University of Technology.

[32] Sjöberg, P., *Chemistry and applications of dinitramides*, in *Energetic Materials: Part 1. Decomposition, Crystal and Molecular Properties*, P. Politzer and J.S. Murray, Editors. 2003, Elsevier: Hungary.

[33] Wingborg, N., M. Johansson, and L. Bodin. *ADN-based liquid monopropellants: Propellant selection and initial thruster development*. in *European Space Agency, (Special Publication) ESA SP*. 2006.

[34] Agrawal, J.P. and R. Hodgson, *Organic chemistry of explosives*. 2007, Chichester: Wiley.

[35] Bottaro, J.C., P.E. Penwell, and R.J. Schmitt, *1,1,3,3-Tetraoxo-1,2,3-triazapropene Anion, a New Oxy Anion of Nitrogen: The Dinitramide Anion and Its Salts.* Journal of the American Chemical Society, 1997. **119**(40): p. 9405-9410.

[36] Wingborg, N. and R. Tryman. *ADN-based monopropellants for spacecraft propulsion*. in *10th International Workshop on Combustion and Propulsion*. 2003.

[37] Wingborg, N., C. Eldsäter, and H. Skifs. *Formulation and characterization of ADN-based liquid monopropellants*. in *European Space Agency, (Special Publication) ESA SP*. 2004. Sardinia.

[38] Scharlemann, C., *GRASP-A European Effort to Investigate Green Propellants for Space Application*, in *Space Propulsion 2010*. 2010: San Sebastian.

[39] Dan, A., et al., *Influence of the Fuel on Thermal and Catalytic Decompositions of Ionic Liquid Monopropellants*, in *41st AIAA/ASME/SAE/ASEE Joint Propulsion Conference & Exhibit*. 2005, American Institute of Aeronautics and Astronautics: Tucson, AZ.

[40] Wingborg, N., *Ammonium dinitramide−water: Interaction and properties.* Journal of Chemical & Engineering Data, 2006. **51**(5): p. 1582-1586.

[41] Venkatachalam, S., G. Santhosh, and K. Ninan Ninan, *An Overview on the Synthetic Routes and Properties of Ammonium Dinitramide (ADN) and other Dinitramide Salts.* Propellants, Explosives, Pyrotechnics, 2004. **29**(3): p. 178-187.

[42] Vyazovkin, S. and C.A. Wight, *Ammonium dinitramide: Kinetics and mechanism of thermal decomposition.* The Journal of Physical Chemistry A, 1997. **101**(31): p. 5653-5658.

[43] Reed, B.D., *On-board chemical propulsion technology*, in *10th International Workshop on Combustion and Propulsion*. 2004: La Spezia.

[44] Dieter, Z., et al., *Evaluation of HAN-Based Propellant Blends*, in *39th AIAA/ASME/SAE/ASEE Joint Propulsion Conference and Exhibit*. 2003, American Institute of Aeronautics and Astronautics.

[45] Nagamachi, M.Y., et al., *ADN - The new oxidizer around the corner for an environmentally friendly smokeless propellant.* Journal of Aerospace Technology and Management, 2011. **1**(2): p. 153-160.

[46] Ledgard, J.B., *The Prepatory Manual of Explosives*. 3rd ed. 2007, United States of America. 574.

[47] Schoyer, H.F.R., et al., *Overview of the development of hydrazinium nitroformate.* Journal of Propulsion and Power, 2002. **18**(1): p. 131-137.

[48] Suceska, M., *Test Methods for Explosives*. 1995, New York: Springer-Verlag.

[49] Von Elbe, G., et al., *Research on combustion in solid rocket propellants: hydrazine nitroform as a propellant ingredient*. 1964, Technical Report DA-36-034-AMC-0091R, Atlantic Research Corporation.

[50] Van der Heijden, A.E.D.M. and A.B. Leeuwenburgh, *HNF/HTPB propellants: Influence of HNF particle size on ballistic properties.* Combustion and Flame, 2009. **156**(7): p. 1359-1364.

[51] Williams, G.K. and T.B. Brill, *Thermal decomposition of energetic materials 67. Hydrazinium nitroformate (HNF) rates and pathways under combustionlike conditions.* Combustion and Flame, 1995. **102**(3): p. 418-426.

[52] Tang, K.C. and M.Q. Brewster, *Modeling combustion of hydrazinium nitroformate.* Proceedings of the Combustion Institute, 2002. **29**(2): p. 2897-2904.

[53] Tummers, M.J., A.E.D.M. van der Heijden, and E.H. van Veen, *Selection of burning rate modifiers for hydrazinium nitroformate.* Combustion and Flame, 2012. **159**(2): p. 882-886.

[54] Lee, H. and T.A. Litzinger, *Thermal decomposition of HAN-based liquid propellants.* Combustion and Flame, 2001. **127**(4): p. 2205-2222.

[55] Oxley, J.C. and K.R. Brower. *Thermal decomposition of hydroxylamine nitrate*. in *Propulsion*. 1988. Los Angeles: Proc. SPIE 0872.

[56] Kappenstein, C., N. Pillet, and A. Melchior. *New nitrogen-based monopropellants (HAN, ADN, HNF,...). Physical chemistry of concentrated ionic aqueous solutions*. in *AAAF 6th Intern. Symp., Propulsion for Space Transportation of the XXIst Century*. 2002. Versailles.

[57] Courthéoux, L., et al. *Thermal and Catalytic Decomposition of HNF and HAN-based Propellants*. in *European Space Agency, (Special Publication) ESA SP*. 2004. Sardinia.

[58] Cawlfield, D.W., *Process for the production of high purity hydroxylammonium nitrate*. 1993, US Patents 5,213,784.

[59] Kartte, K., *Production of hydroxylammonium nitrate*. 1974, US Patents 3,856,924.

[60] Fuchs, H., et al., *Preparation of hydroxylammonium salts*. 1989, US Patent 4,889,704.

[61] Liggett, T., *Process for producing concentrated solutions of hydroxylammonium nitrate and hydroxylammonium perchlorate*. 1978, The United States Of America As Represented By The Secretary Of The Navy.

[62] Dotson, R.L. and R.T. Brooker, *Process for concentrating aqueous solutions of hydroxylammonium nitrate*. 1989, US Patent 4,851,125.

[63] Levinthal, M.L., et al., *Process for making high purity hydroxylammonium nitrate*. 1993, US Patents 5,266,290.

[64] Amrousse, R., et al., *HAN and ADN as liquid ionic monopropellants: Thermal and catalytic decomposition processes.* Applied Catalysis B: Environmental, 2012. **127**: p. 121-128.

[65] Shaw, B.D. and F.A. Williams, *A Model for the Deflagration of Aqueous Solutions of Hydroxylammonium Nitrate.* Symposium (International) on Combustion, 1992. **24**(1): p. 1923-1930.

[66] Pembridge, J.R. and G. Stedman, *Kinetics, Mechanism, and Stoicheiometry of the Oxidation of Hydroxylamine by Nitric Acid.* Journal of the Chemical Society, Dalton Transactions, 1979(11): p. 1657-1663.

[67] Liu, L., et al., *Hydroxylamine Nitrate Self-Catalytic Kinetics Study with Adiabatic Calorimetry.* Journal of Hazardous Materials, 2009. **162**(2-3): p. 1217-1222.

[68] Rafeev, V.A. and Y.I. Rubtsov, *Kinetics and mechanism of thermal decomposition of hydroxylammonium nitrate.* Russian Chemical Bulletin, 1993. **42**(11): p. 1811-1815.

[69] Kondrikov, B.N., et al., *Burning of Hydroxylammonium Nitrate.* Combustion, Explosion and Shock Waves, 2000. **36**(1): p. 135-145.

[70] Lee, H. and T.A. Litzinger, *Chemical Kinetic Study of HAN Decomposition.* Combustion and Flame, 2003. **135**(1-2): p. 151-169.

[71] Cronin, J.T. and T.B. Brill, *Thermal Decomposition of Energetic Materials. 29 - The Fast Thermal Decomposition Characteristics of a Multicomponent Material: Liquid Gun Propellant 1845.* Combustion and Flame, 1988. **74**(1): p. 81-89.

[72] Schoppelrei, J.W., M.L. Kieke, and T.B. Brill, *Spectroscopy of Hydrothermal Reactions. 2. Reactions and Kinetic Parameters of [NH3OH]NO3 and Equilibria of (NH4)2CO3 Determined with a Flow Cell and FT Raman Spectroscopy.* The Journal of Physical Chemistry, 1996. **100**(18): p. 7463-7470.

[73] Schoppelrei, J.W. and T.B. Brill, *Spectroscopy of Hydrothermal Reactions. 7. Kinetics of Aqueous [NH3OH]NO3 at 463-523 K and 27.5 MPa by Infrared Spectroscopy.* The Journal of Physical Chemistry A, 1997. **101**(46): p. 8593-8596.

[74] Amrousse, R., et al., *Thermal and Catalytic Decomposition of H2O2-Ionic Liquid Monopropellant Mixtures on Monolith-Based Catalysts*, in *46th AIAA/ASME/SAE/ASEE Joint Propulsion Conference & Exhibit*. 2010: Nashville, TN.

[75] Tompa, A.S., *Thermal analysis of ammonium dinitramide (ADN).* Thermochimica Acta, 2000. **357-358**: p. 177-193.

[76] Dendage, P.S., et al., *Characterization and thermal analysis of hydrazinium nitroformate (HNF).* Journal of Energetic Materials, 2003. **21**(3): p. 167-183.

[77] Anflo, K., T. Gronland, and N. Wingborg, *Development and testing of ADN-based monopropellants in small rocket engines*, in *35th Intersociety Energy Conversion Engineering Conference and Exhibit*. 2000, American Institute of Aeronautics and Astronautics: Cagliari.

[78] Gadiot, G.M.H.J.L., et al., *Hydrazinium nitroformate and its use as oxidizer in high performance solid propellants.* Environmental Aspects of Rocket and Gun Propulsion, 1995.

[79] Amrousse, R., et al., *Corrigendum to: "HAN and ADN as liquid ionic monopropellants: Thermal and catalytic decomposition processes" [Appl. Catal. B: Environ. 127 (2012) 121–128].* Applied Catalysis B: Environmental, 2014. **158–159**: p. 426-428.

[80] Courthéoux, L., et al., *Catalytic Decomposition of HAN-Water Binary Mixtures*, in *38th AIAA/ASME/SAE/ASEE Joint Propulsion Conference & Exhibit*. 2002, American Institute of Aeronautics and Astronautics: Indianapolis. p. 4027/1-4027/10.

[81] Hwang, C.H., S.W. Baek, and S.J. Cho, *Experimental investigation of decomposition and evaporation characteristics of HAN-based monopropellants.* Combustion and Flame, 2014. **161**(4): p. 1109-1116.

[82] Amrousse, R., et al., *Hydroxylammonium nitrate as greeen propellant: Decomposition and stability.* International Journal of Energetic Materials and Chemical Propulsion, 2012. **11**(3): p. 241-257.

[83] Chang, Y.P., et al., *Combustion Characteristics of Energetic HAN/Methanol-based Monopropellants*, in *38th AIAA/ASME/SAE/ASEE Joint Propulsion Conference & Exhibit*. 2002, American Institute of Aeronautics and Astronautics: Indianapolis, IN, USA. p. 4032/1-4032/14.

[84] Katsumi, T., et al., *Combustion Characteristics of Hydroxylammonium Nitrate Aqueous Solutions.* International Journal of Energetic Materials and Chemical Propulsion, 2010. **9**(3): p. 219-231.

[85] Amrousse, R., et al., *New HAN-based mixtures for reaction control system and low toxic spacecraft propulsion subsystem: Thermal decomposition and possible thruster applications.* Combustion and Flame, 2015. **162**(6): p. 2686-2692.

[86] Lee, Y.J. and T.A. Litzinger, *Combustion chemistry of HAN, TEAN, and XM46.* Combustion Science and Technology, 1999. **141**(1-6): p. 19-36.

[87] Cronin, J.T. and T.B. Brill, *Thermal Decomposition of Energetic Materials. 8. Evidence of an Oscillating Process during the High-Rate Thermolysis of Hydroxylammonium Nitrate, and Comments on the Interionic Interactions.* Journal of Physical Chemistry, 1986. **90**(1): p. 178-181.

[88] Adams, M. and E.J. Barth, *Dynamic modeling and design of a bulk-loaded liquid monopropellant powered rifle.* Journal of Dynamic Systems, Measurement, and Control, 2008. **130**(6): p. 61001.

[89] DeSpirito, J., *Interior ballistic simulations of the bulk-loaded liquid propellant gun*. 2001, DTIC Document.

[90] Rosenberger, T., I. Stobie, and J. Knapton, *Test Results from a 37-mm Segmented-Chamber Bulk-Loaded Liquid Propellant Gun*. 1995, DTIC Document.

[91] Klein, N. *Ignition and Combustion of the HAN-Based Liquid Propellants*. in *Proceedings of 27th JANNAF Combustion Subcommittee Meeting*. 1990. Laurel: CPIA Pub.

[92] Bonner, F.T. and N.Y. Wang, *Reduction of nitric oxide by hydroxylamine. 1. Kinetics and mechanism.* Inorganic Chemistry, 1986. **25**(11): p. 1858-1862.

[93] Bonner, F.T., L.S. Dzelzkalns, and J.A. Bonucci, *Properties of nitroxyl as intermediate in the nitric oxide-hydroxylamine reaction and in trioxodinitrate decomposition.* Inorganic Chemistry, 1978. **17**(9): p. 2487-2494.

[94] Hisatsune, K., et al., *Development of HAN-based liquid propellant thruster*, in *2nd International Conference on Green Propellants for Space Propulsion*. 2004: Cagliari, Italy. p. 25/1-25/5.

[95] Amrousse, R., et al., *Performance and deactivation of Ir-based catalyst during hydroxylammonium nitrate catalytic decomposition.* Applied Catalysis A: General, 2013. **452**(0): p. 64-68.

[96] Courthéoux, L., et al., *Transformation of platinum supported on silicon-doped alumina during the catalytic decomposition of energetic ionic liquid.* Journal of Catalysis, 2005. **232**(1): p. 10-18.

[97] Courthéoux, L., et al., *Facile Catalytic Decomposition at Low Temperature of Energetic Ionic Liquid as Hydrazine Substitute.* European Journal of Inorganic Chemistry, 2005. **2005**(12): p. 2293-2295.

[98] Courthéoux, L., et al., *Platinum supported on doped alumina catalysts for propulsion applications. Xerogels versus aerogels.* Journal of Non-Crystalline Solids, 2004. **350**: p. 113-119.

[99] Xiaoguang, R., et al., *Catalytic decomposition of hydroxyl ammonium nitrate at room temperature.* Chinese Journal of Catalysis, 2007. **28**(1): p. 1-2.

[100] Yetter, R.A., et al., *Combustion Issues and Approaches for Chemical Microthrusters.* International Journal of Energetic Materials and Chemical Propulsion, 2007. **6**(4): p. 393-424.

[101] Katsumi, T., et al., *A Study On The Combustion Mechanism Of Hydroxylammonium Nitrate.* International Journal of Energetic Materials and Chemical Propulsion, 2015. **14**(4): p. 307-319.

[102] Amariei, D., et al., *Catalytic and thermal decomposition of ionic liquid monopropellants using a dynamic reactor. Comparison of powder and sphere-shaped catalysts.* Chemical Engineering and Processing: Process Intensification, 2007. **46**(2): p. 165-174.

[103] Amariei, D., et al. *Shape forming of Pt/Al2O3Si sol-gel catalysts for space applications*. in *Scientific Bases for the Preparation of Heterogeneous Catalysts, Proceedings of the 9th International Symposium*. 2006. Elsevier.

[104] Amrousse, R., et al., *Chemical engineering study for hydroxylammonium nitrate monopropellant decomposition over monolith and grain metal-based catalysts.* Reaction Kinetics, Mechanisms and Catalysis, 2014. **111**(1): p. 71-88.

[105] Klingenberg, G., H. Frieske, and H. Rockstroh, *Electrical Ignition of HAN-based liquid propellants*. 1990.

[106] Klingenberg, G., et al., *Investigation of liquid gun propellants: Electrical ignition of LGP 1846.* Propellants, Explosives, Pyrotechnics, 1990. **15**(3): p. 103-114.

[107] Yetter, R., et al., *Development of Meso and Micro Scale Liquid Propellant Thrusters*, in *41st Aerospace Sciences Meeting and Exhibit*. 2003, American Institute of Aeronautics and Astronautics: Reno.

[108] Meng, H., et al. *Decomposition and ignition of HAN-based monopropellants by electrolysis*. in *47th AIAA Aerospace Sciences Meeting including the New Horizons Forum and Aerospace Exposition*. 2009. Orlando.

[109] Risha, G.A., R.A. Yetter, and V. Yang, *Electrolytic-Induced Decomposition and Ignition of HAN-Based Liquid Monopropellants.* International Journal of Energetic Materials and Chemical Propulsion, 2007. **6**(5): p. 575-588.

[110] Hua, M., et al., *Decomposition and Ignition of HAN-Based Monopropellants by Electrolysis*, in *47th AIAA Aerospace Sciences Meeting including The New Horizons Forum and Aerospace Exposition*. 2009, American Institute of Aeronautics and Astronautics: Orlando, FL. p. 5064-5079.

[111] Khare, P., et al., *Thermal and Electrolytic Decomposition and Ignition of HAN–Water Solutions.* Combustion Science and Technology, 2015. **187**(7): p. 1065-1078.

[112] Yu, Y., et al., *Study on Electrical Ignition and Micro-Explosion Properties of HAN-Based Monopropellant Droplet.* Frontiers of Energy and Power Engineering in China, 2010. **4**(3): p. 430-435.

[113] Yu, Y., et al., *Study on electrical ignition characteristics of HAN-based liquid propellant spray.* Advanced Materials Research, 2012. **588-589**: p. 268-272.

[114] Liu, K., Y.-G. Yu, and B. Ni, *Numerical simulation for arcless electrical ignition process of single droplet of HAN-based liquid propellant.* Hanneng Cailia/Chinese Journal of Energetic Materials, 2014. **22**(2): p. 155-160.

[115] Koh, K.S., J. Chin, and T.F.W.K. Chik, *Role of Electrodes in Ambient Electrolytic Decomposition of Hydroxylammonium Nitrate (HAN) Solutions.* Propulsion and Power Research, 2013. **2**(3): p. 194-200.

[116] Reed, B. and S. Harasim, *Material compatibility testing with HAN-based monopropellants.* AIAA paper, 2001. **3696**.

[117] Wu, M.-H. and R.A. Yetter, *A Novel Electrolytic Ignition Monopropellant Microthruster Based on Low Temperature Co-fired Ceramic Tape Technology.* Lab on a Chip, 2009. **9**(7): p. 910-916.

[118] London, A.P., *A systems study of propulsion technologies for orbit and attitude control of microspacecraft*, in *Department of Aeronautics and Astronautics*. 1997, Massachusetts Institute of Technology.

[119] Bayt, R.L., *Analysis, fabrication and testing of a MEMS-based micropropulsion system*. 1999, Aerospace Computational Design Laboratory, Dept. of Aeronautics & Astronautics, Massachusetts Institute of Technology.

[120] Mueller, J., *Thruster options for microspacecraft: a review and evaluation of existing hardware and emerging technologies.* AIAA paper, 1997. **3058**: p. 1997.

[121] Zhang, J., et al., *Polymerization optimization of SU-8 photoresist and its applications in microfluidic systems and MEMS.* Journal of Micromechanics and Microengineering, 2001. **11**(1): p. 20.

[122] Reznikova, E.F., J. Mohr, and H. Hein, *Deep photo-lithography characterization of SU-8 resist layers.* Microsystem Technologies, 2005. **11**(4-5): p. 282-291.

[123] Becker, H. and C. Gärtner, *Polymer microfabrication technologies for microfluidic systems.* Analytical and Bioanalytical Chemistry, 2008. **390**(1): p. 89-111.

[124] Kuo-Shen, C., et al., *Effect of process parameters on the surface morphology and mechanical performance of silicon structures after deep reactive ion etching (DRIE).* Microelectromechanical Systems, Journal of, 2002. **11**(3): p. 264-275.

[125] Santana, P.P.d., I.M.F.d. Oliviera, and E. Piccin, *Evaluation of using xurography as a new technique for the fabrication of disposable gold electrodes with highly reproducible areas.* Electrochemistry Communications, 2012. **16**(1): p. 96-99.

[126] Bartholomeusz, D.A., R.W. Boutte, and J.D. Andrade, *Xurography: Rapid Prototyping of Microstructures Using A Cutting Plotter.* Journal of Microelectromechanical Systems, 2005. **14**(6): p. 1364-1374.

[127] Fouchal, F. and P. Dickens, *Adaptive screen printing for rapid manufacturing.* Rapid Prototyping Journal, 2007. **13**(5): p. 284-290.

[128] Wolfe, D.B. and G.M. Whitesides, *Rapid prototyping of functional microfabricated devices by soft lithography*, in *Nanolithography and patterning techniques in microelectronics*, D.G. Bucknall, Editor. 2005, Woodhead Pub Limited. p. 76-118.

[129] Kolekar, R.D., *Fluid flow characteristics in xurographic microchannels*, in *Department of Mechanical Engineering*. 2009, University of Utah.

[130] Kanakamedala, S.K., et al. *A simple enzyme based biosensor on flexible plastic substrate*. in *SPIE NanoScience+ Engineering*. 2010. San Diego: International Society for Optics and Photonics.

[131] Kim, D.S., et al., *Disposable integrated microfluidic biochip for blood typing by plastic microinjection moulding.* Lab on a Chip, 2006. **6**(6): p. 794-802.

[132] Steigert, J., et al., *Rapid prototyping of microfluidic chips in COC.* Journal of Micromechanics and Microengineering, 2007. **17**(2): p. 333-341.

[133] Jenny, G., et al., *Comparison of glass etching to xurography prototyping of microfluidic channels for DNA melting analysis.* Journal of Micromechanics and Microengineering, 2007. **17**(12): p. 2407.

[134] Hyewon, K., et al., *An improved method of preparing composite poly(dimethylsiloxane) moulds.* Nanotechnology, 2006. **17**(1): p. 197.

[135] Koo, N., et al., *Improved mold fabrication for the definition of high quality nanopatterns by Soft UV-Nanoimprint lithography using diluted PDMS material.* Microelectronic Engineering, 2007. **84**(5-8): p. 904-908.

[136] Gale, B.K., et al., *Low-Cost MEMS Technologies*, in *Comprehensive Microsystems*, Y. Gianchandani, O. Tabata, and H. Zappe, Editors. 2008, Elsevier. p. 341-378.

[137] Armani, M., R. Probst, and B. Shapiro, *Fabricating PDMS microfluidic channels using a vinyl sign plotter*, in *Lab on a Chip Technology, Volume 1: Fabrication and Microfluidics*, K.E. Herold and A. Rasooly, Editors. 2009, Caister Academic Press: Norfolk, UK.

[138] Chaudhury, M.K. and G.M. Whitesides, *Direct measurement of interfacial interactions between semispherical lenses and flat sheets of poly(dimethylsiloxane) and their chemical derivatives.* Langmuir, 1991. **7**(5): p. 1013-1025.

[139] Lee, J.N., C. Park, and G.M. Whitesides, *Solvent compatibility of poly(dimethylsiloxane)-based microfluidic devices.* Analytical Chemistry, 2003. **75**(23): p. 6544-6554.

[140] Dangla, R., F. Gallaire, and C.N. Baroud, *Microchannel deformations due to solvent-induced PDMS swelling.* Lab on a Chip, 2010. **10**(21): p. 2972-2978.

[141] André, E.-T., A. Yamada, and L. Wang. *An inexpensive and durable epoxy mould for PDMS*. Chips and Tips 2009 17 July 2013]; Available from: http://blogs.rsc.org/chipsandtips/2009/04/22/an-inexpensive-and-durable-epoxy-mould-for-pdms/.

[142] Björn, S., M.K. Chowdhury, and S. Göran, *The fabrication of microfluidic structures by means of full-wafer adhesive bonding using a poly(dimethylsiloxane) catalyst.* Journal of Micromechanics and Microengineering, 2007. **17**(8): p. 1710-1714.

[143] Koerner, T., et al., *Epoxy resins as stamps for hot embossing of microstructures and microfluidic channels.* Sensors and Actuators B: Chemical, 2005. **107**(2): p. 632-639.

[144] Yu, H., et al., *Soft lithography replication based on PDMS partial curing.* Microsystem Technologies, 2011. **17**(3): p. 443-449.

[145] Eddings, M.A., M.A. Johnson, and B.K. Gale, *Determining the optimal PDMS–PDMS bonding technique for microfluidic devices.* Journal of Micromechanics and Microengineering, 2008. **18**(6): p. 067001.

[146] Bahadorimehr, A., et al. *Low cost fabrication of passive microfluidic devices*. in *Nanotechnology (IEEE-NANO), 2010 10th IEEE Conference on*. 2010.

[147] Land, K.J., et al., *Low cost fabrication and assembly process for re-usable 3D polydimethylsiloxane (PDMS) microfluidic networks.* Biomicrofluidics, 2011. **5**(3): p. -.

[148] Maji, D., S.K. Lahiri, and S. Das, *Study of hydrophilicity and stability of chemically modified PDMS surface using piranha and KOH solution.* Surface and Interface Analysis, 2012. **44**(1): p. 62-69.

[149] Jeffrey, R., S. Raymond, and M.-S. Manuel, *Micropropulsion system selection for precision formation flying satellites*, in *37th Joint Propulsion Conference and Exhibit*. 2001, American Institute of Aeronautics and Astronautics: Salt Lake City.

[150] Steven, B. and R. Joshua, *Ignition evaluation of monopropellant blends of HAN and Imidazole-based ionic liquid fuels*, in *50th AIAA Aerospace Sciences Meeting including the New Horizons Forum and Aerospace Exposition*. 2012, American Institute of Aeronautics and Astronautics: Nashville.

[151] Cheah, K.H., P.S. Khiew, and J.K. Chin, *Fabrication of a zirconia MEMS-based microthruster by gel casting on PDMS soft molds.* Journal of Micromechanics and Microengineering, 2012. **22**(9): p. 095013.

[152] Wu, M.H., R.A. Yetter, and V. Yang. *Development and characterization of ceramic micro chemical propulsion and combustion systems*. in *46th AIAA Aerospace Sciences Meeting and Exhibit*. 2008. Reno.

[153] Zube, D.M., E.J. Wucherer, and B. Reed, *Evaluation of HAN-Based Propellant Blends*, in *39th AIAA/ASME/SAE/ASEE Joint Propulsion Conference and Exhibit*. 2003, American Institute of Aeronautics and Astronautics: Huntsville, AL, USA. p. 12.

[154] Dennis, M., et al., *Development and testing of new, HAN-based monopropellants in small rocket thrusters*, in *34th AIAA/ASME/SAE/ASEE Joint Propulsion Conference and Exhibit*. 1998, American Institute of Aeronautics and Astronautics.

[155] Vanderhoff, J.A. and S.W. Bunte, *Electrical conductivity measurements of hydroxylammonium nitrate: Design considerations*. 1986, DTIC Document.

[156] Decker, M., et al., *HAN-Based Liquid Gun Propellants: Physical Properties.* US Army Ballistic Research Laboratory, Aberdeen Proving Ground, Maryland, 1987: p. 11.

[157] Vanderhoff, J.A., S.W. Bunte, and P.M. Donmoyer, *Electrical Conductance of Liquid Propellants: Theory and Results*. 1986, DTIC Document.

[158] Iizuka, T., et al., *Investigation of Discharge Plasma as Reaction Initiation System for 1N-class Thrusters with Green Propellants.* TRANSACTIONS OF THE JAPAN SOCIETY FOR AERONAUTICAL AND SPACE SCIENCES, AEROSPACE TECHNOLOGY JAPAN, 2014. **12**(ists29): p. Ta_5-Ta_9.

[159] Toshiaki, I., et al., *Feasible Study on Low Frequency Plasma Jet as Ignition System for HAN Based Propellant*, in *48th AIAA/ASME/SAE/ASEE Joint*

Propulsion Conference & Exhibit. 2012, American Institute of Aeronautics and Astronautics.

[160] Singh, D.A., *Sugar Based Rocket Propulsion System- Making, Analysis & Limitations.* International Journal of Engineering Trends and Applications, 2015. **2**(5): p. 30-37.

[161] Schmidt, E.W., *Hydroxylammonium Nitrate Compatibility Tests with Various Materials-A Liquid Propellant Study*. 1990, DTIC Document.

[162] Agrawal, J.P., *High Energy Materials: Propellants, Explosives and Pyrotechnics*. 2010, Weinheim: Wiley-VCH. 464.

[163] Hurley, C., et al., *Properties of alternatively fueled ammonium nitrate explosives.* 1996.

[164] Journal, I.s.P.a.M. *Current Metal Prices*. 2017 [cited 2017 2/7/2017]; Available from: http://www.icmj.com/current-metal-prices.php.

[165] Kuo, B.-H., *A Study on the Electrolytic Decomposition of HAN-Based Propellants for Microthruster Applications*, in *Department of Mechanical Engineering*. 2010, The Pennsylvania State University.

[166] Bamford, C.H., R.G. Compton, and C.F.H. Tipper, *Decomposition of Inorganic and Organometallic Compounds*. Comprehensive Chemical Kinetics, ed. C.H. Bamford, R.G. Compton, and C.F.H. Tipper. Vol. 4. 1972, Amsterdam, Netherlands: Elsevier. 271.

[167] MacDonald, D.K.C. and D. Tuomi, *Thermoelectricity: An Introduction to the Principles*. Dover Books on Physics. 2006, Mineloa, New York: Dover Publications.

[168] Pennington, N.L. and C.W. Baker, *Sugar: User's Guide To Sucrose*. AVI Books. 1990: Van Nostrand Reinhold.

[169] Lee, J.W., et al., *Investigation of Thermal Decomposition as the Kinetic Process That Causes the Loss of Crystalline Structure in Sucrose Using a Chemical Analysis Approach (Part II).* Journal of Agricultural and Food Chemistry, 2011. **59**(2): p. 702-712.

[170] Predoi, D., *Physico-chemical studies of sucrose thin films.* Digest Journal of Nanomaterials and Biostructures 2010. **5**(2): p. 373-377.

[171] Hurtta, M., I. Pitkänen, and J. Knuutinen, *Melting behaviour of d-sucrose, d-glucose and d-fructose.* Carbohydrate Research, 2004. **339**(13): p. 2267-2273.

[172] Boggs, B.K., R.L. King, and G.G. Botte, *Urea electrolysis: direct hydrogen production from urine.* Chemical Communications, 2009(32): p. 4859-4861.

[173] Fisher Scientific. *Safety data sheet - Ammonia solution 35%*. 2012; Available from: http://wercs.acros.com/wercsdata/document.aspx?prd=FSUA3280~~PDF~~MTR~~CLP1~~EN~~2010-11-25%2015:45:14~~Ammonia%20solution%2035%.

[174] McDonald, J.C. and G.M. Whitesides, *Poly(dimethylsiloxane) as a Material for Fabricating Microfluidic Devices.* Accounts of Chemical Research, 2002. **35**(7): p. 491-499.